A MICROFLUIDIC CHIP – BASED SYNTHESIS OF CARBON-11 RADIOTRACERS FOR THE PURPOSE OF PET IMAGING

by

Samar Haroun
BSc., The University of Western Ontario, 2008

THESIS SUBMITTED IN PARTIAL FULFILLMENT OF
THE REQUIREMENTS FOR THE DEGREE OF
MASTER OF SCIENCE

In the Department of Chemistry

© Samar Haroun 2011

SIMON FRASER UNIVERSITY

Spring 2011

APPROVAL

Name:	**Samar Haroun**
Degree:	**Master of Science**
Title of Thesis:	**A Microfluidic chip–based Synthesis of Carbon-11 Radiotracers for the purpose of PET Imaging**

Examining Committee:

Chair: **Dr. Neil Branda**
Professor, Department of Chemistry

_____

Dr. Paul C. H. Li
Senior Supervisor
Professor, Department of Chemistry

_____

Dr. Thomas J. Ruth
Co-Senior Supervisor
Adjunct Professor, Department of Chemistry

_____

Dr. Corina Andreoiu
Supervisor
Assistant Professor, Department of Chemistry

_____

Dr. Erika Plettner
Supervisor
Associate Professor, Department of Chemistry

_____

Dr. Tim Storr
Internal Examiner
Assistant Professor, Department of Chemistry

Date Defended/Approved: **January 17, 2011**

Declaration of Partial Copyright Licence

ABSTRACT

A microchip-based technique was developed for the radiolabeling process of positron emission tomography (PET) radiotracers using C–11. Due to C–11's short half-life (20.4 min) it is beneficial to develop a rapid and efficient synthesis that can be done while the patient is waiting. The investigation began with the non-radioactive synthesis of raclopride ((2S)-(-)-3,5-dichloro-N-((1-ethyl-2-pyrrolidinyl)methyl)-6-hydroxy-2-methoxybenzamide), a compound used to study dopamine receptors. The reaction was optimized on the microchip achieving 2-times the yields using ~$1/20^{th}$ the precursor amounts and ~$1/5^{th}$ the reaction time compared to the conventional method. Consequently, optimal parameters were applied to the radiolabeling synthesis of L-[methyl-^{11}C]-methionine achieving 100% relative activities while the [^{11}C]raclopride synthesis resulted in lower relative activities. Therefore reaction conditions were investigated and a computational mass transfer study showed that the reaction kinetics of the radiolabeling process must be considered for the microchip design.

Keywords: microfluidic reactor; positron emission tomography (PET) imaging; radiotracer; raclopride; L-methionine; computational fluid dynamics (CFD)

DEDICATION

To my mum, the most driven and selfless person I know.

For all the motivation and encouragement and for being my biggest fan:

Thank you!

ACKNOWLEDGEMENTS

TABLE OF CONTENTS

LIST OF FIGURES

LIST OF TABLES

LIST OF EQUATIONS

LIST OF SCHEMES

LIST OF ABBREVIATIONS AND SYMBOLS

[^{11}C]MET   L-[methyl-^{11}C]-methionine

[^{11}C]MeI   [^{11}C]methyl iodide

[^{11}C]MT   [^{11}C]methyl triflate

[^{11}C]Rac   [^{11}C]Raclopride

C – 11   Carbon – 11

CFD   Computational fluid dynamics

DI   De-Ionized

DMR   Desmethyl raclopride

DMSO   Dimethyl sulfoxide

EOB   End of bombardment

HPLC   High Performance Liquid Chromatography

ID   Inner diameter

IPA   Isopropyl alcohol

IS   Internal standard

L-homo   L-homocysteine thiolactone hydrochloride

MeCN	Acetonitrile
MET	L-methioine
MeI	Methyl iodide
OD	Outer diameter
PDMS	Polydimethylsiloxane
PEEK	Polyetheretherketone
PET	Positron-emission tomography
R	Rate of reaction
RAD-HPLC	Radiochemical HPLC
UV-HPLC	UV Visible HPLC
Rac	Raclopride
REL	Reaction Engineering Lab (a COMSOL module)
RT	Retention time
SA	Specific Activity

η	Viscosity
ρ	Density
c	Concentration
D	Diffusion coefficient
F	Body forces on microchannels
F_o	Initial molar flow rate
F_f	Final molar flow rate
h	microchannel height
p	Pressure
u	Microchannel velocity
v	Volumetric flow rate
V	Volume
w	microchannel width

1: INTRODUCTION

1.1 Positron Emission Tomography (PET)

1.1.1 Overview

Positron-emission tomography (PET) is a highly sensitive imaging technique that is capable of monitoring molecular or metabolic processes in living patients [1-5]. This technique uses radioactive probes, known as "radiotracers" that generate a signal. This signal is detected externally giving us the ability to image biochemical and physiological processes *in vivo* in a non-invasive manner [2-3, 6-9]. Imaging techniques such as magnetic resonance imaging, X-rays, and/or ultrasounds are all common ways to explore the structural abnormalities of an organ or tissue by providing us with its physical structure [2, 7]. What these techniques lack is the ability to provide information about on-going biochemical processes on the molecular level, which is definitely of great value for early disease diagnosis and new drug design.

The radiotracer compounds are designed with great selectivity for the tissue or receptor of interest in order to provide an accurate image of the biological process occurring at the target. Commonly used radionuclides for PET imaging are low atomic mass isotopes of key elements of a living organism (e.g. C, N, O and F see Table 1-1) [2-3, 10-11]. Therefore, this has made it convenient to label the molecules of interest directly and provide an image without disturbing

the biological process [3, 6]. Their known decay paths and short half-lives have made them very desirable for physiological study [1].

Table 1-1 PET radionuclides and their half-life, their decay mode and decay product after positron emission. *Source:* **Welch and Redvanly, 2003.**

Radionuclide	Half-life, $t_{1/2}$ (min)	Decay mode	Decay product
^{11}C	20.4	100% β^+	^{11}B
^{13}N	9.97	100% β^+	^{13}C
^{15}O	2.04	100% β^+	^{15}N
^{18}F	110	97% β^+, 3% EC*	^{18}O

EC = electron capture

In PET imaging a radiotracer is administered to the subject, most commonly, by ingestion, intravenous injection or inhalation [5]. The highly selective molecule then travels to the area of interest where it behaves in a similar manner to a naturally occurring biological compound within the body. Throughout this process, the radioisotope decays mainly by positron emission (see Scheme 1-1).

$$^{11}_{6}C \rightarrow {}^{11}_{5}B + {}_{1}\beta^+ + v$$
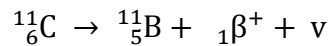
Scheme 1-1 Shows the decay of carbon-11 (^{11}C, C – 11) to boron-11 by releasing a positron (β^+) and neutrino (v).

Once released, the positron travels a short distance before it collides with an electron in the tissue. This process is known as annihilation and results in the release of two gamma ray photons (at 511 KeV) that travel out of the body in

opposite directions along a straight line, known as the "line of coincidence" (see Figure 1-1) [2-3, 5]. For this reason the PET scintillation detectors are arranged in a circular ring in order to capture the signal from both gamma rays in every annihilation [1]. This signal is then used to approximate the location of the PET radiotracer probe in the body. The arrangement and design generates a three-dimensional image of the radiotracer's location, giving not only the structural information about the tissue but also the biological distribution of the compound.
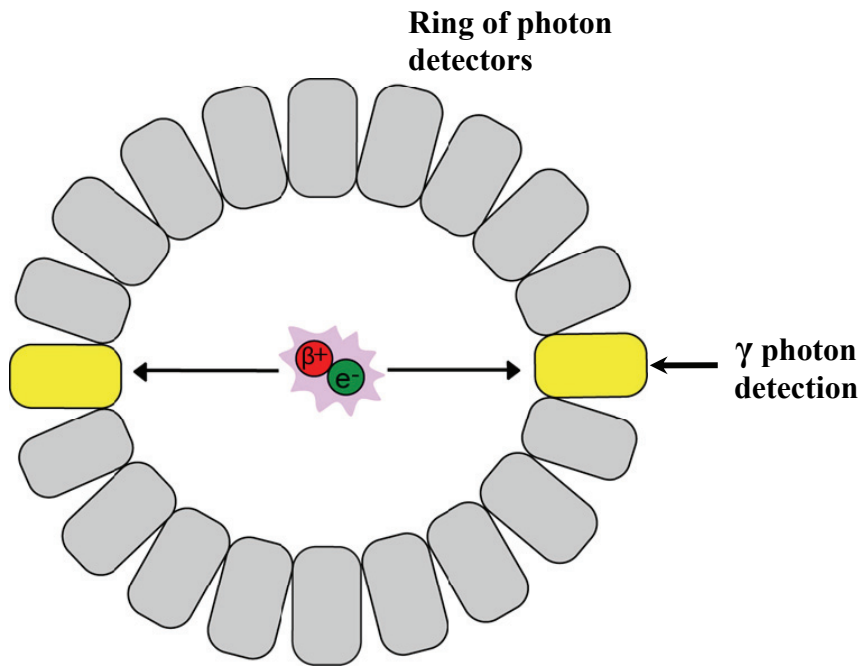
Figure 1-1 Principle of a PET detector showing the release of two gamma (γ) ray photons due to the annihilation of an electron (β⁻) and a positron (β⁺). (Similar to [2])

The concentration and distribution of the radiotracers can be observed over time to give quantitative information on the physiological and biochemical

events. This capability has given PET imaging valuable use in many medical applications such as oncology for the diagnosis of tumours, cardiology for diagnosing heart disease and neurology for the characterization of early stage neurological disorders [2].

1.1.2 PET radionuclides

1.1.2.1 Overview and synthesis of short-lived PET isotopes

PET imaging radionuclides are usually generated using a cyclotron with a 7 – 15 MeV energy. The cyclotron operates by generating a negative ion source (H$^-$) by passing H$_2$ gas through an electrical field (see Figure 1-2(a)). A magnetic field within the cyclotron moves the charged particles (H$^-$) in a circular path outwards while they gain energy (see Figure 1-2(a)) [3]. Then an ultra thin foil (usually made of graphite) is placed strategically where the electrons are extracted from the H$^-$ beam resulting in the change of the beam charge and in turn generating a beam of protons (H$^+$) (see Figure 1-2 (a) and (b)) [12]. With this, the beam made of protons reverses direction in the magnetic field and by placing exit ports on the cyclotron tank wall the H$^+$ beam can be directed out to the target of choice (see Figure 1-2(c) for a schematic diagram of a gas target). This extracted beam is used to bombard the target material at certain energies to produce the PET radionuclide of interest [3, 7].
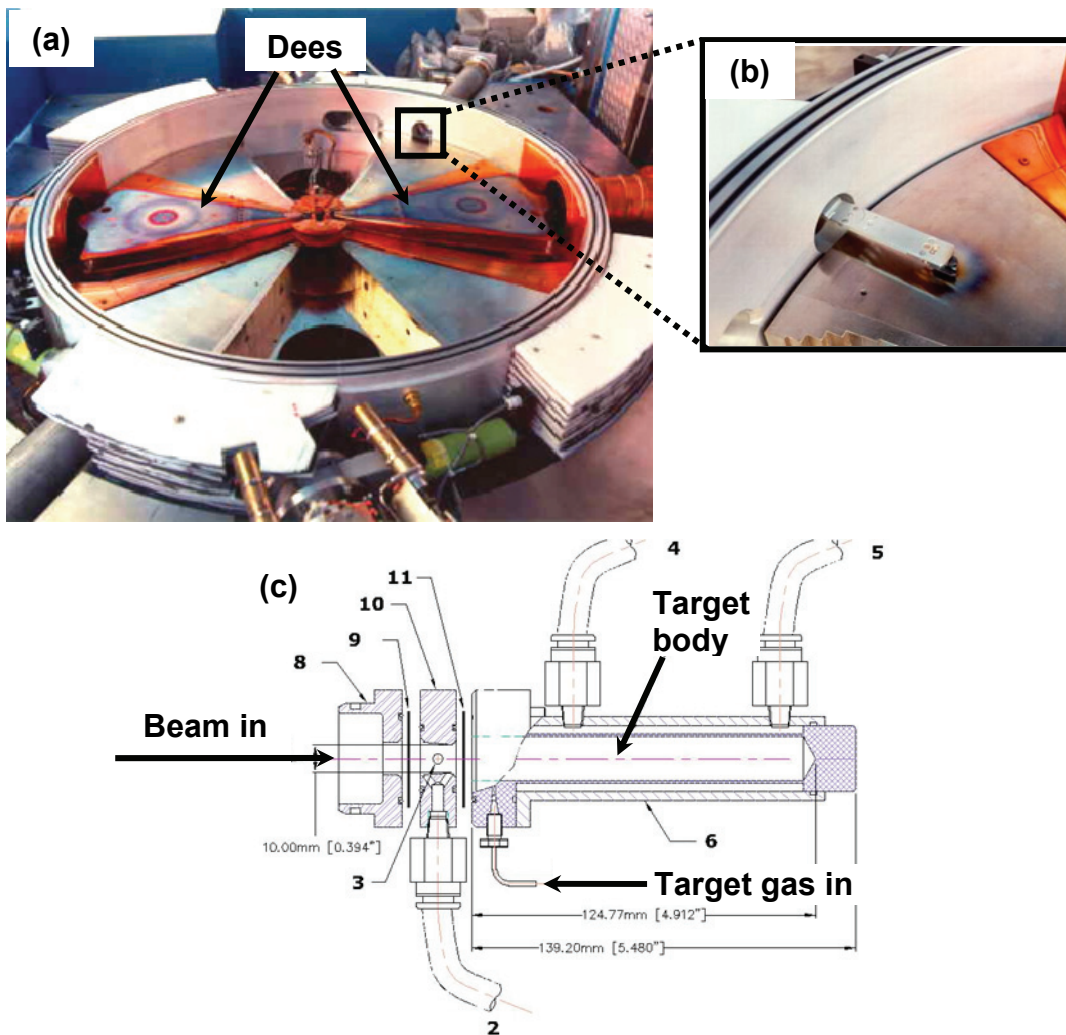
Figure 1-2 (a) Picture of the inside of the TR13 cyclotron showing the vacuum tank dees, (b) a close-up of the foil extractor location where the beam is redirected outside of the cyclotron into the target of choice and (c) a schematic of a typical gas target for the TR-13. (As shown in [10, 12])

For example, C – 11 is produced by irradiating N_2, a gas target with a proton beam generated in a cyclotron ($^{14}N(p,\alpha)^{11}C$). C – 11 is then converted into $[^{11}C]CH_4$ in the presence of H_2 or $[^{11}C]CO_2$ in the presence of O_2. The radionuclide is then transferred to a chemistry module, where it is used to synthesize an imaging probe (see Scheme 1-2).

1.1.2.2 General aspects C – 11 radiolabeling

C – 11 is a commonly used radionuclide for PET biomedical research purposes. It can be easily found in naturally occurring biological compounds and can be substituted in for carbon-12 without significantly altering the reaction mechanisms or the biological behaviour of the molecule [3]. Its half-life is enough to perform an experiment in order to investigate a biological event but also short enough for easy disposal and repeated investigations in patients with minimal radiation dose exposure [3, 5, 8]. Unfortunately, for radiotracer production purposes the 20.4 min C – 11 half-life creates difficulties for the radiochemists [3]. Due to time limitations C – 11 imaging usually requires an on-site radiochemistry facility and access to a nearby cyclotron. In addition, patients are scheduled according to the radiotracer probe availability instead of the imaging requirements [3, 5, 13].

Therefore, due to these properties it becomes important to choose a shorter synthetic pathway for C – 11 radiotracers [2]. The radiolabeling process starts with two major cyclotron produced precursors, $[^{11}C]CH_4$ and $[^{11}C]CO_2$. These can be used directly as primary precursors or can be converted into other more suitable secondary precursors to be used in the radiolabeling processes (see Scheme 1-2) [2-3]. For example $[^{11}C]$methyl iodide ($[^{11}C]MeI$, $[^{11}C]CH_3I$), a commonly used radiolabeling precursor, is synthesized through the iodination of $[^{11}C]CH_4$ at high temperatures (~725 ^0C) [14].

$[^{11}C]CHCl_3 \longrightarrow [^{11}C]CH_2N_2$

$[^{11}C]CH_3I \longleftarrow \boxed{[^{11}C]CH_4} \longrightarrow [^{11}C]HCN$

$[^{11}C]CH_3OSO_2CF_3 \qquad [^{11}C]COCl_2$
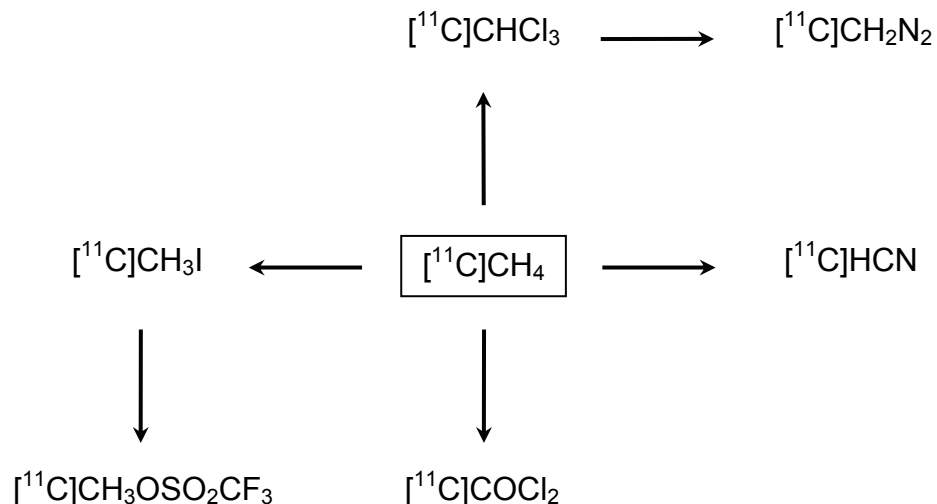
Scheme 1-2 PET radiolabeling secondary precursors prepared from $[^{11}C]CH_4$. *Source: Welch, 2003.*

Methylation reactions have become the most widespread method for C – 11 radiotracer syntheses [2, 15-16]. Their radiolabeling processes usually involve a nucleophilic substitution with a biological probe precursor at a nitrogen, oxygen or sulphur site. The commonly used secondary precursor for this process has been $[^{11}C]MeI$ due to its rapid and highly efficient methylation properties. $[^{11}C]MeI$ is synthesized with specific activities (SA, ratio of a radiolabeled probe`s activity to its non-radiolabeled counterpart) between 1 – 15 Ci/µmol and radiochemical yields (RCY) that are greater than 50% [2, 14]. Some examples of radiotracers synthesized through methylation reactions include; L-[methyl-^{11}C]-methionine ($[^{11}C]MET$) which is used in oncology for protein synthesis monitoring, $[^{11}C]$raclopride ($[^{11}C]Rac$) which is used in psychiatry for dopamine receptor imaging, $[^{11}C]$Meta-hydroxyephedrine which is used in cardiology for adrenergic

receptor imaging and [¹¹C]PiB (Pittsburgh compound B) which is used in neurology for amyloid plaque imaging for the purpose of Alzheimer's disease diagnosis [2, 17].

[¹¹C]MET is an amino acid that is routinely used for PET imaging purposes, and has been used to image brain, pancreas, neck, lung and breast tumours for diagnosis and research purposes [18-20]. It is also used to study hyper-ammonemia, a metabolic system disorder that is described by excess ammonia in children's blood [18]. Its synthesis involving the methylation of a sulphide anion in a chiral precursor (e.g. L-homocysteine thiolactone HCl (L-homo)) in the presence of sodium hydroxide (NaOH), has been optimized to produce enantiomeric purities >99% and over 90% RCY (see Scheme 1-3). Its L-homo precursor is also cheap and easy to generate [18, 20].
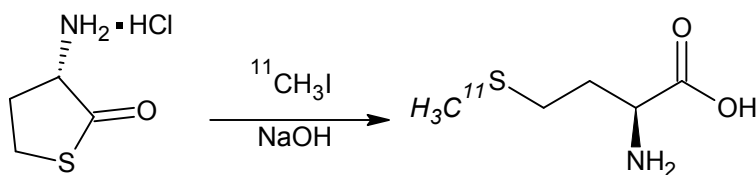
Scheme 1-3 [¹¹C]MET synthesis process from L-homo [21].

Meanwhile, [¹¹C]Rac is a PET radiotracer used to examine dopamine D_2 receptors. Due to its high binding affinity and selectivity as a receptor antagonist it has become a very important imaging tool [22]. It is currently used in the diagnosis and study of neuropsychiatric diseases such as Schizophrenia,

Parkinson's disease and drug abuse [22]. [11C]Rac has been synthesized using [11C]MeI and [11C]methyl triflate ([11C]MT, $^{11}CH_3OSO_2CF_3$) achieving final product yields between 50 – 65% (see Scheme 1-4 and Scheme 1-5) [22].
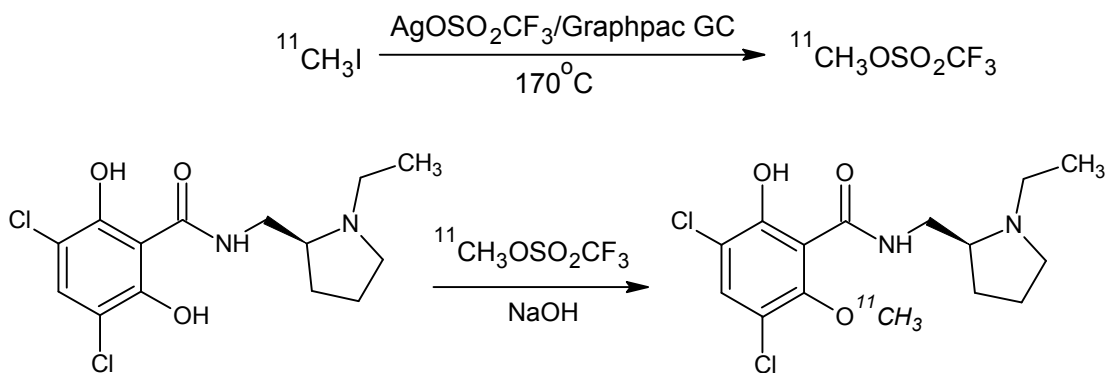
Scheme 1-4 [11C]methyl triflate preparation from [11C]methyl iodide through a glass column (Graphpac GC) containing silver triflate and the synthesis of [11C]Rac using [11C]MT [22-23].

[11C]MT can produce high yields with lower precursor amounts and shorter reactions times. However, it has become a less attractive choice than [11C]MeI for the purpose of automated systems' development since it adds an extra step to the synthetic process. [11C]Rac is currently synthesized routinely for clinical investigation using [11C]MeI with acceptable final yields of 17 – 45% with a specific activity of 7 – 10 Ci/μmol [24]. This reaction consumes up to 1.7 mg of the precursor with a total production time of up to 35 – 45 min [24].
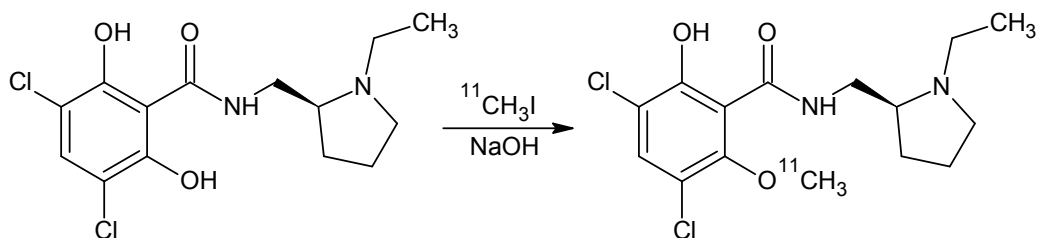
Scheme 1-5 [¹¹C]Rac synthesis using [¹¹C]MeI [3, 24-25].

[¹¹C]Rac is an important compound for brain research; however its high operational cost, expensive precursor and its demand for access to a nearby cyclotron and radiopharmaceutical facility limits its commercial availability, and presents an obstacle for its use [25].

Finally, the use of C – 11 in PET imaging research is increasingly growing and is expected to have many applications. This of course makes the development of new radiolabeled probes and synthesis tools very important to the progress its research and production [2-3].

1.2 Microfluidics in chemical synthesis

1.2.1 Background

Microfluidic devices consist of a network of micrometer-sized channels, which facilitate the manipulation of nanoliter amounts of volume where reagents are combined to react under specific physical conditions [8, 26-28]. These miniaturized devices have been used in many biological and chemical applications ranging from micromixing, chemical synthesis, separation, chemical transformations to integrated devices for research and commercial purposes

showing an advantage over conventional processes [8, 16, 29]. Examples have shown improved yields and purer products with greater selectivity syntheses due to the increased surface area-to-volume ratio in the microchannels (up to 50000 m^2/m^3 compared to conventional laboratory reactors at 1000 m^2/m^3) [30]. Also, in many applications microreactors have allowed users to achieve these promising results using reduced reagent amounts and shorter reaction times than conventional processes with milder and more controllable reaction conditions [8, 16, 30]. Moreover, their fabrication process (even for complicated and integrated devices) is relatively inexpensive which is encouraging for mass production and automation [8]. Use of these devices has grown tremendously over the past decade because as controllable enclosed systems they can provide insight on the reaction pathways and kinetics of processes, which has the potential to reduce product development timelines [29, 31].

The type of microfluidic reactor (microchip) used depends on the purpose of the investigation. Two types of microfluidic reactor designs commonly used include the continuous-flow (also single and multiphase) and batch-mode microfluidic reactors [29, 32]. Batch-mode microfluidic reactors are made of a combination of reaction modules composed of microchannel networks that are usually separated by a valving system. Fluid can be dispensed in different directions and into different compartments for various isolated reactions [8]. Due to their compartmentalizing property, the batch-mode microfluidic reactors have been used for parallel syntheses involving the combination of multiple reagents in multi-step processes. In contrast, continuous-flow microfluidic reactors involve

pressure-driven or electrokinetic/electroosmotic flow of fluids into the microchannels. This is carried out either with the use of peristaltic pumps or an applied electric field respectively. Therefore, reagents are dispensed into the microfluidic reactor where they meet and mix while flowing through the microchannels and being exposed to heat [8]. Therefore, the continuous-flow microfluidic reactors have been mostly developed for high throughput large-scale continuous production applications.

1.2.2 Microfluidic chip continuous-flow chemical syntheses

A continuous-flow microfluidic reactor system involves the continuous pumping of fluids into the microchannels and collection of product from the outlets (plug-flow) [26]. During this process, the reaction completion time (residence time) in a flask corresponds to the time reagents take to flow through the micro-size channels [26, 29]. The microfluidic reactor device can include micromixer designs that usually enhance reagent contact, mixing and heat transfer, which can be advantageous to the overall rate of reaction [26, 29]. With the use of single-phase or multi-phase flow, microfluidic reactors have found applications in oxidation and reduction reactions, alkylations, hydrolysis, peptide synthesis, polymer synthesis, hydrogenation reaction, photochemical reactions and much more (see Table 1-2) [26, 31].

The microfluidic reactor geometry facilitates the optimization of reaction conditions such as temperature, flow rate and residence time, which is an advantage when optimizing reaction processes. For example, Ratner *et. al.* used a simple serpentine microfluidic reactor to explore a glycosylation reaction where

the product stereochemistry is dependent on temperature, solvent choice, stoichiometry and concentration (see Figure 1-3) [29, 33]. This process involved dissolving the reagents in solution and adding them separately into the microchannels. First the fluids entered a "mixing zone" and then proceeded into a long serpentine microchannel for reaction completion (see Figure 1-3) [33]. Using the microfluidic reactor they were able to reduce reagent quantities compared to conventional methods and efficiently handle microliters of volume. They were also able to carry out up to 44 experiments to explore the temperature and residence time effects on the synthesis process from a single batch of reagents. Furthermore, maximum conversions were achieved within a short residence time (26 – 213 s) [33]. Finally, with an enclosed system and controlled reaction conditions they were able to retrieve data that improved their understanding of the reaction kinetics [29, 33].
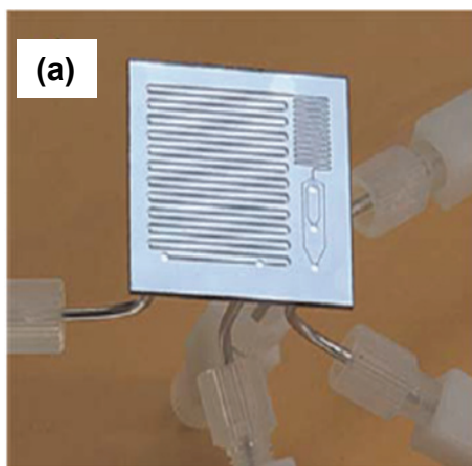
Figure 1-3 (a) Shows a picture of the silicon reactor used in the investigation. *Source: Ratner et. al.*, **2004.**

Whether a reaction is single phase or multiphase the reduced diffusion distances in the microchannels can increase the "interfacial area" (area of contact between two fluids in the microchannel, see Figure 1-7) contact for a faster overall rate of reaction in comparison to the conventional methods. For example, Hisamoto's phase transfer (organic and aqueous phase) reaction performed on the setup shown in Figure 1-4 with a microfluidic reactor (200 µm in width, 100 µm in depth, and 45 cm in length), produced yields as high as 57% in 1 min and 90% in 5 min (longer residence time) [34-35]. This was an improvement compared to the experiments that were carried out in a round-bottom flask using the same conditions, at high stirring rates giving only 37% yields in 1 min [34].

(a)

1a   2a   TBAB   NaOH/CH₂Cl₂   3a

$$\text{1a} + \text{PhCH}_2\text{Br} \xrightarrow[\text{NaOH/CH}_2\text{Cl}_2]{\text{TBAB}} \text{3a}$$

(b)

0.3 M **1a**
0.45 M **2a**

Microreactor

teflon tube (10 cm)

5 mol% TBAB
0.5 N NaOH aq.

NH₄Cl aq.

(c)

Yield/%

100
90
80
70
60
50
40
30
20
10
0

(a)
(b)
(c)
(d)

0   100   200   300   400   500   600

Mean Residence Time/sec.

(a) Microreactor

(b) Round-bottomed flask (1350 rpm)

(c) Round-bottomed flask (400 rpm)

(d) Round-bottomed flask (0 rpm)
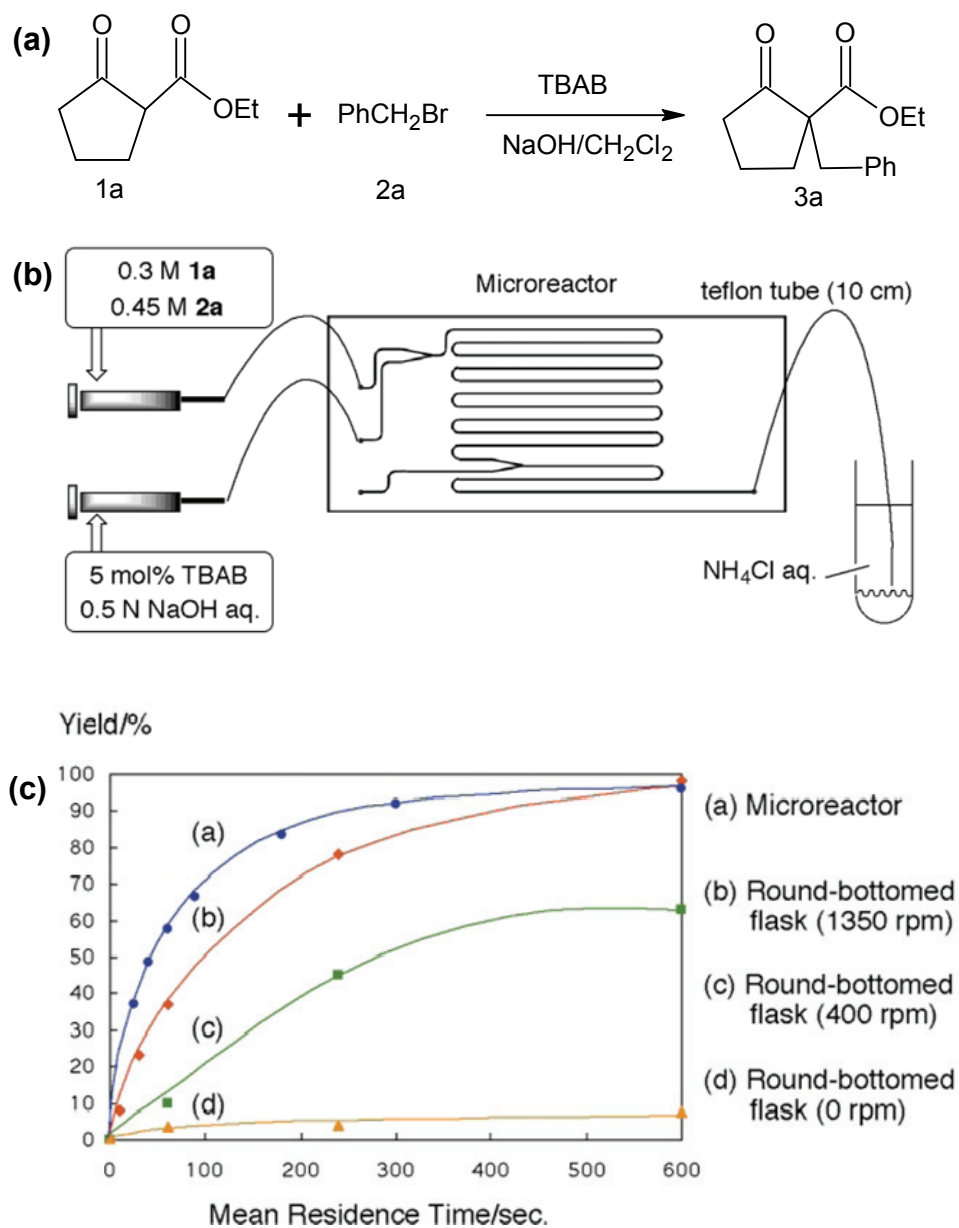
Figure 1-4 (a) Scheme of the phase-transfer benzylation reaction of ethyl 2-oxocyclopentanecarboxylate (1a) with benzyl bromide (2a) in the presence of tetrabutylammonium bromide (TBAB). (b) A schematic of the experimental setup for the phase transfer alkylation reaction with reagents 1a and 2a dissolved in dichloromethane (CH₂Cl₂) and an aqueous solution of NaOH and TBAB are introduced through separate inlets. (c) Chemical yields (%) for the experiments using the microfluidic reactor and the round-bottom flasks at various stirring rates. *Source:* Ueno *et. al.,* 2003.

Other continuous-flow microfluidic reactor applications include (Haswall *et. al.*) Kumada coupling, (Wilson *et. al.*) dehydration reaction, (Lu *et. al.*) photochemical reaction and (Hisamoto *et. al.*) phase-transfer synthesis across two liquid phases (see Table 1-2) [31].

Table 1-2 Examples of continuous-flow reactions carried out in a microfluidic reactor. *Source:* **Fletcher e*t. al.* 2002.**

Reaction	Chip material	Flow (delivery)	Solvent	Conversion (%)	Ref.
Kumada coupling	PP	Pressure driven	THF	60	[36]
Dehydration	Glass/ PDMS	Pressure driven/EOF	EtOH	85 – 95	[37]
Photochemical	Silicon/ quartz	Pressure driven	IPA	60	[38]
Phase transfer alkylation	Glass	Pressure driven	EtOAc	100	[34]
Phase transfer	Glass	Pressure driven	DCM	100	[39]

*PP = polypropylene, PDMS = polydimethylsiloxane, THF = tetrahydrofuran, EtOH = ethanol, IPA = isopropyl alcohol, EtOAc =ethyl acetate, DCM = dichloromethane, EOF = electroosmotic flow

1.2.2.1 C – 11 radiolabeling on a microchip

The challenge with C – 11 radiotracer production is in developing a rapid, reliable and versatile radiolabeling platform [2]. Considering that the radiolabeled precursors are short-lived, most production processes completed within 2 – 3 half-lives can result in over 75% – 88% radioactivity loss [30]. Therefore, large amounts of initial activity are needed to compensate for the preparation time and in some cases the low RCYs. As a result, the synthesis process is usually carried out using remote operations within a shielded hot cell (similar to a fumehood but

made of lead). Additionally, excess amounts of the expensive precursor (10^2 to 10^6) are used to accelerate the radiolabeling process [24]. This and other limitations add to the high costs of the radiotracer production.

As a result of these limitations, much work has been done to develop semi-automated on-line synthesis apparatus with reduced personnel activity exposure that incorporate the purification processes with the aim of reducing production time and costs [8]. Such systems have facilitated the use of the radioactive precursors in limited amounts (e.g. [^{11}C]MeI, usually in nmol) for radiotracer syntheses. In addition, their reduced manual operation and increased reproducibility have improved product standards [8, 30]. However, most of the current semi-automated systems are designed to handle macroscale amounts of liquid while the reaction volumes are usually between 0.3 – 3.0 mL. Separation and purification are also a challenge with these systems considering that the excess precursor amounts make the small amount of product harder to extract. Furthermore, available modules are usually radiotracer specific and hard to adapt to new syntheses without making major modifications to the system. Lastly, these automated systems are usually very expensive and still require specially trained staff as well as a hot cell or mini-cell for shielding purposes making them an impractical option for some PET centres [8, 40].

Consequently, the development of microfluidic reactors for PET radiotracer synthesis has attracted a great deal of attention over the past decade [8, 16]. PET radiolabeling miniaturization has the potential of reducing probe precursor amounts, reducing the reaction scale even further and with automation

it can provide better fluid handling and control over reaction conditions [30]. Also, the enhanced mass and heat transfer and reduced diffusion distances in the microchannels can result in an increase of RCY and product purity [30]. In addition, their small dimensions can reduce workspace and facilitate more localized shielding requirements [8, 30].

Many investigations have demonstrated the potential applicability and benefits of implementing microfluidic modules for radiolabeling purposes (see Table 1-3) [8, 16]. For example, Lu *et. al.* were able to radiolabel a carboxylic ester using [^{11}C]MeI on a continuous flow T-shaped microchip that is 200 µm wide and 60 µm deep with a total volume capacity of 0.2 µL (see Figure 1-5).
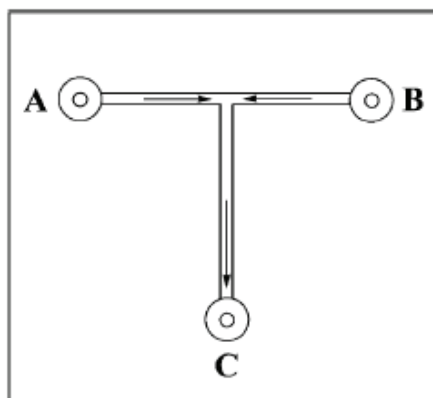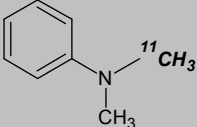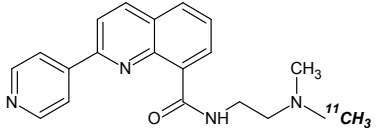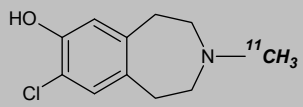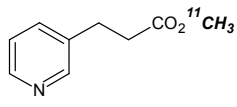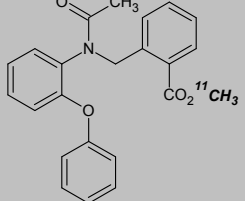
Figure 1-5 Schematic diagram of the microchip used in ^{11}C carboxylic esters radiolabeling. Reagents are added into inlet A and B and product sample is collected at outlet C. *Source:* Lu *et. al.,* 2004.

The precursors, 3-(3-pyridinyl)propionic acid and [^{11}C]MeI were both introduced through separate inlets and at a 1 µL/min flow rate they were able to achieve RCYs as high as 88% (see Table 1-3, entry 4) [15]. This was completed

using smaller reagent amounts in a residence time of 12 s and total processing time of 10 min, at room temperature. Using the same microchip design Lu *et. al.* also investigated the synthesis of compound 5 generating RCYs as high as 65% (see Table 1-3) [15]. In these examples the purification process was easily carried out on an analytical high performance liquid chromatography (HPLC) system and the RCYs were calculated in a similar manner to the conventional radiolabeling methods using the initial C–11 activity and final product C–11 activity [8]. Brady *et. al.* also filed a patent for a similar microchip with a serpentine design that was used for C – 11 methylation reactions where they achieved 5 – 19% RCYs synthesizing compound 5 at higher flow rates between 10 – 100 μL/min [41].

Table 1-3 List of ^{11}C-labelled PET tracers synthesized on various glass microchips [8].

	Compound	^{11}C-labeling reagent	Reaction condition	RCY (%)
1		$[^{11}C]CH_3I$	NaOH, acetone, RT	Not reported
2		$[^{11}C]CH_3I$	Acetone, RT	10%
3		$[^{11}C]CH_3I$	NEt₃, acetone, RT	5 – 19%
4		$[^{11}C]CH_3I$	nBu_4NOH, DMF, RT	56%*, 88%**
5		$[^{11}C]CH_3I$	nBu_4NOH, DMF, RT	45%*, 65%**

RT = Room temperature, Pd = palladium, DMF = N,N-dimethylformamide,
*10 µL/min, **1 µL/min.

These C – 11 radiolabeling examples have shown reaction times and RCYs that are similar to the conventional methods. They have also highlighted the benefits of the miniaturization of the radiolabeling processes, such as reduced precursor amounts and more controlled reaction conditions [8, 16, 40]. However, in order to approach production standards a microfluidic device must be capable of fast, reliable and reproducible multi-tracer production. Its operation must be fully automated and should incorporate product formulation. Considering that these standards have not been met by any device, further research is still

needed before this technology can be implemented for the routine production of PET radiotracers [8, 16, 30].

1.2.3 Fabrication and system design

Microfluidic reactors usually consist of a network of channels constructed on a substrate that is made of glass, ceramic, quartz, silicon, metal or a polymer (fluoropolymer) (see Figure 1-6) [8, 16, 26, 29-30, 32]. The material chosen for the fabrication of a microfluidic reactor is dependent on its application [26]. For instance, design requirements such as multi-layering and the use of a valving system can restrict the fabrication to certain materials. Also, microfluidic reactors for industrial or medicinal production purposes must consider the material biocompatibility and its pressure and temperature restrictions as well as solvent compatibility [26].
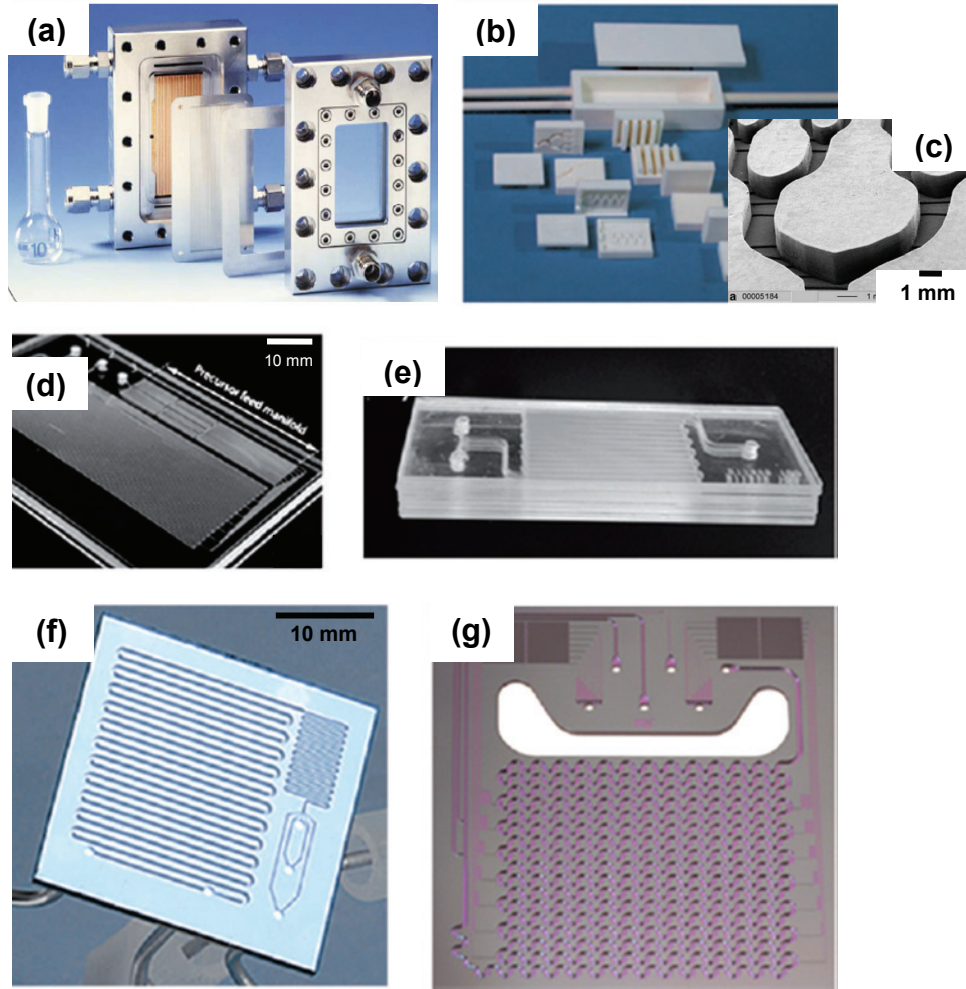
Figure 1-6 Examples of microfluidic reactors fabricated from (a) metal, (b) ceramic and (c) a detailed view of a microstructure example of the ceramic microreactors, (d) PDMS, (e) glass, (f, g) silicon. *Source:* **Hartman and Jensen, 2009.**

Silicon devices are known to be costly and incompatible with strong bases, while metal devices face issues when using strong acids and ceramic devices require complicated fabrication processes. On the other hand, glass and polymer devices have been the most commonly used for microfluidic applications. Polymer material, such as PDMS (made of repeating units of –O–Si(CH$_3$)$_2$–) has become more favourable than glass especially for prototyping

purposes [42]. The advantage to using these PDMS devices is their simple and cost effective soft-lithography fabrication process [32, 43-44]. Once bonded, the PDMS microchips can usually operate at relatively high temperatures and pressures depending on their fabrication and bonding technique [26, 29]. However, their use has been limited to prototyping experiments due to their incompatibility with some organic solvents, which is a major disadvantage [29].

Another part of a microfluidic system design is the fluid delivery method and fluidic connections. Usually the microfluidic reactor design includes cavities and through-holes for the purpose of generating the inlets and outlets [26]. For continuous-flow chemical reaction applications, the most common fluid delivery is carried out using syringe pumps [26, 35]. This continuous-flow design allows for the integration of the system with an analytical instrument such as an HPLC for online-analysis, which is great for the future automation of a system [28]. Fluidic connections between the syringe pumps and the microfluidic reactors involves the use of standard tubing and fixtures with "compressible-type" holders (microchip holders) to create a leak-free connection for fluid delivery into the microchannels [45]. Direct connection of fixtures or tubing on the microfluidic reactors can limit the flexibility of the system by making it hard to replace or remove devices from the process unlike the use of microchip holders where nothing is permanently bound to the reactor [45]. Another advantage of using these microchip holders is the flexibility of designing other features to help control and vary reaction conditions. For example, heat exchangers, pressure sensor

sites and/or even external thermocouples can be incorporated to the microchip holders [26].

1.2.4 Microchannel design

For the purpose of chemical synthesis, fast and thorough mixing of reagents is an important aspect of the reaction progress [16, 30]. Generally, it is believed that the micrometer-scale (microscale) dimensions can increase mixing efficiency by inherently increasing the contact surface between two fluids and decreasing molecular diffusion distances of reagents [29-31, 34, 36, 38-39]. Miniaturization ultimately creates a viscous force dominance over inertial forces in a microfluidic reactor. In a pressure-driven flow microfluidic reactor, low Reynolds numbers (R_e < 2300), which represent the inertial force over the viscous force ratio, generate laminar flow in the microchannels (see Figure 1-7 and Appendix B, Section 5.2.3.2) [30, 46]. Laminar flow generates a "parabolic velocity profile" where the maximum fluid velocity is at the centre of the channel and an almost zero velocity is observed at the channel walls allowing mixing by diffusion only through the liquid interfaces [30, 32, 46]. Mixing of reagents through interfacial interaction of two fluid streams is therefore limited by species diffusion distances and could result in reduced mass and heat transfer [30].
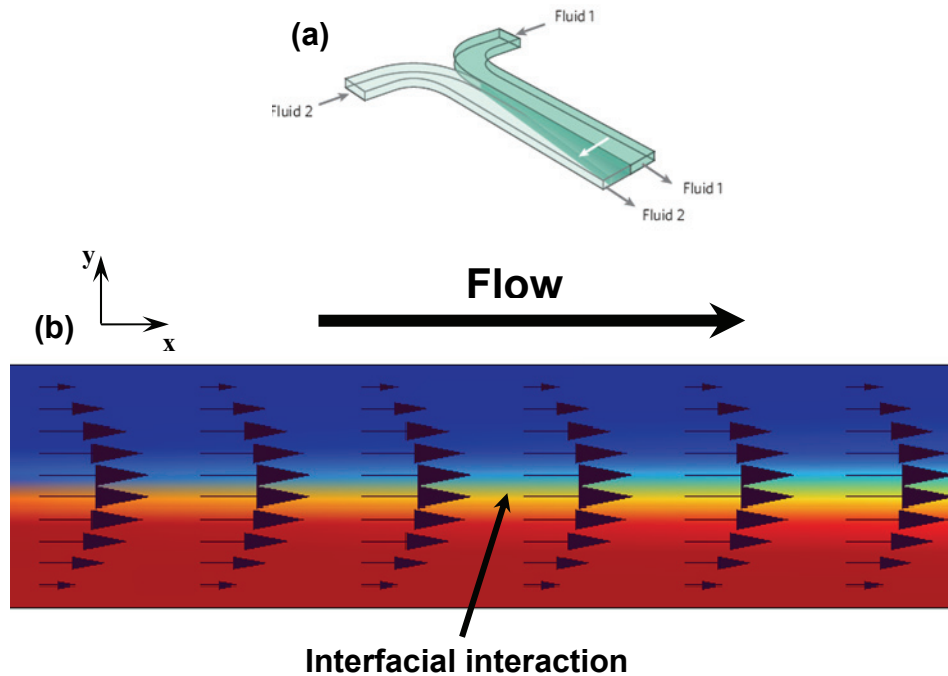
Figure 1-7 (a) Mixing of two miscible fluids at laminar flow in a microchannel through diffusion. *Source:* **deMello, 2006. (b) A schematic of two streams flowing side-by-side. Note: direction of flow is from left to right.**

This mixing issue has been addressed previously by creating various micromixer designs that can further decrease species diffusion distances [30-31]. The two categories of micromixer designs that have been reported in the literature are active and passive micromixers [29, 43, 47-50]. Active mixing involves incorporating moving parts or applying external forces to induce mixing within the microchannels. The agitations can create chaotic advections that enhance the mixing process [51]. Active micromixers can be applied to a continuous, staggered (start/stop) or stopped-flow microfluidic reactor design. Some examples of external forces include ultrasonic vibrations, dielectrophoresis

and magnetic forces [51]. Although these micromixer designs are very efficient at increasing the mixing of species within the microchannels, they are usually hard to fabricate, operate and clean, making them more challenging to implement for a simplistic microfluidic reactor design [32, 52-53].

On the other hand, passive micromixer designs can require a 2D or 3D device fabrication (see Figure 1-8) [46]. Mixing mechanisms include the addition of multiple streams in the flow focusing geometry (see Figure 1-8(f)) and increasing secondary flows through turning and twisting in the tesla structure, zig-zag, square-wave and curve channels (see Figure 1-8(a) – (d)) . Also, the method of creating obstacles through barriers can enhance mixing tremendously; however, it has been known to also create pressure problems especially with highly viscous solvents in continuous-flow. For example, the 3D L-shaped and staggered-herringbone grooves design can induce chaotic mixing but can slow down the flow due to gravity and collision with barriers (see Figure 1-8(e) and (g)) [43]. In addition, for fabrication simplicity 2D micromixing structures have been widely used for many chemical synthesis applications facilitating fast fabrication for prototyping and development. The 2D passive micromixer structure used in this investigation was initially explored by the Whitesides group with the intention to design a portable analytical system that is required to mix and analyze samples using a hand-operated vacuum source (see Figure 1-8(h)) [54]. At the micromixer section, it used gas bubbles to mix two streams of liquid within the microchannels.
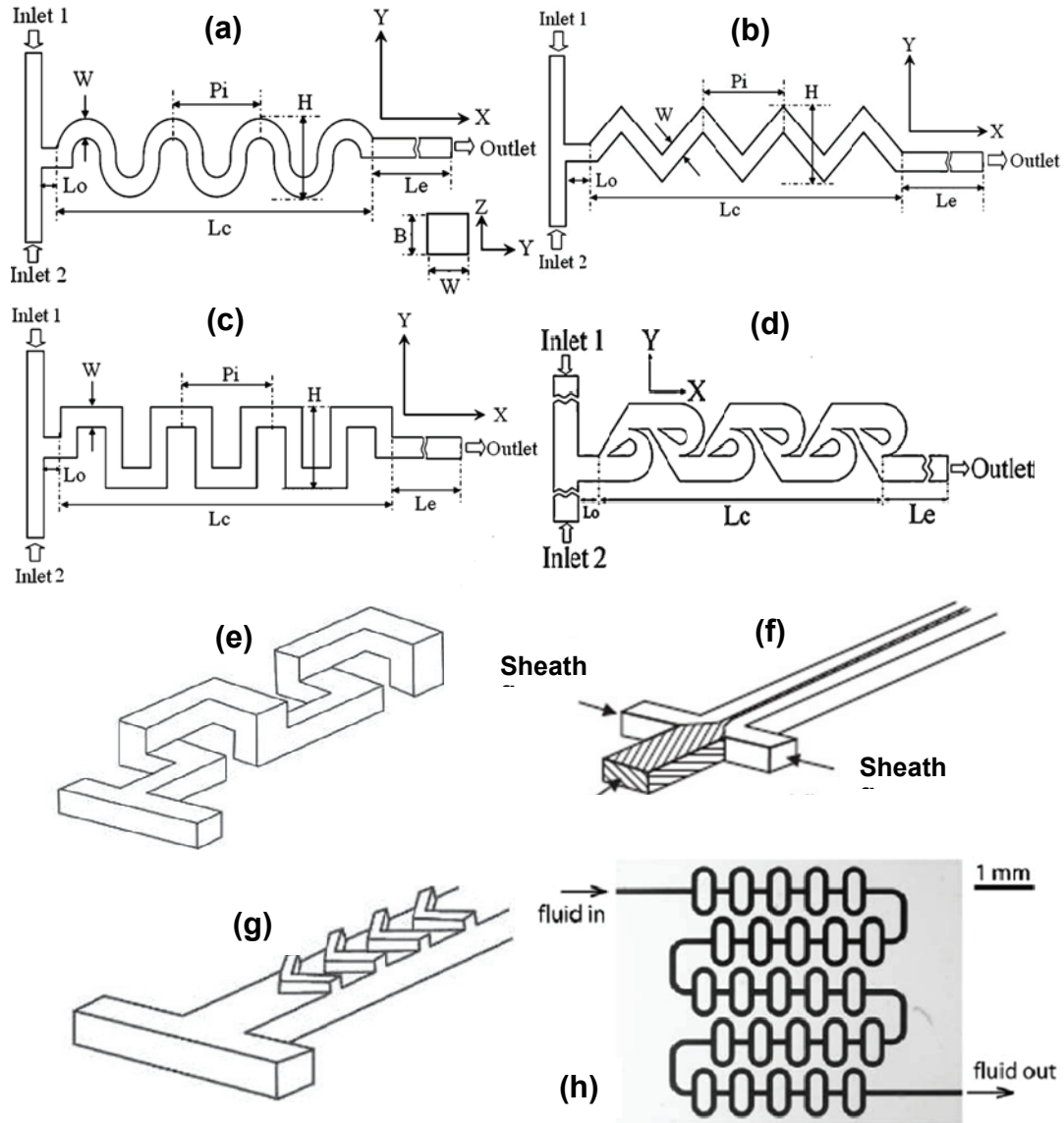
Figure 1-8 Schematic diagrams of Examples of 2D and 3D passive micromixers. (a) curve microchannel, (b) zig-zag microchannel, (c) square-wave microchannel, (d) tesla structure microchannel, (e) 3D L-shaped microchannel, (f) flow-focusing (FF) inlet junction design, (g) Staggered-herringbone grooves microchannel and (h) an optical image of the mixer section showing a branched micromixer design [46-48, 51-52, 54].

1.2.5 Computational fluid dynamics (CFD)

The growing use of microfluidic reactors for a wide range of biological and chemical applications has inspired more ways for the research and development of new devices and lab-on-a-chip (LOC) systems [55-56]. Obtaining an efficient microfluidic reactor design for a particular application can be done more accurately by implementing a computational investigation. In these investigations, the relationship between the hydrodynamics and the reaction kinetics combined with experimental data can produce a more complete picture of the reaction progress in the microchannels [55, 57]. Therefore allowing researchers to evaluate the effect of the flow and mass transfer within the microchannel design on the reaction progress and product formation. Computational analysis displays many advantages especially the ability to generate information about a particular microfluidic reactor design that can be used in comparison with experimental data to enhance a particular microreactor design for optimal conditions [57].

Extensive CFD analysis has been carried out to study micromixer designs such as the T-shaped micromixer chip (see Figure 1-5). This in many cases has helped create new and more efficient designs to overcome slow diffusion in the microchannels [49, 51-52, 55]. The modelling process usually involves generating a simple and realistic model that is able to incorporate various geometries while evaluating parameters such as the diffusion coefficient, reaction temperature, flow rate, residence time and so on. For instance, computational work carried out by Meijir *et. al.* compares passive and active micromixer

designs [49]. To study the effect of various reaction conditions on chemical selectivity and yields, it has become important to incorporate both the momentum and mass transfer for a more accurate estimation of the microfluidic reactor conditions [55]. CFD allows for the investigation of micromixing efficiency at different R_e numbers (see Appendix B, Section 5.2.3.2) while implementing the reaction kinetics and exploring the mass flux at different parameters as well [58-61]. Variations in reactor lengths, residence times, micromixer structure and reaction conditions (temperature, pressure, rate constants) and many more parameters are all possible through CFD analysis. For example, Buddoo *et. al.* investigated the first-order synthesis of linalool (component of fragrances and flavours) on a multi-channel microfluidic reactor (14 channel, 0.5 mm × 0.4 mm) in comparison to a mini-channel tubular reactor (ID = 4.6 mm) [57]. Using the CFD software and reaction kinetics, Buddoo *et. al.* were also able to explore the effects of temperature and residence time on the decomposition of the compound during the synthesis process. The simulation results estimated the optimal reaction parameters for the synthetic process which were then validated by the collected experimental data [57].

1.3 Thesis motivation and objectives

1.3.1 Thesis motivation

PET radiosynthesis still faces problems with production and development due to long radiolabeling processes. Specifically, the production process for a C – 11 radiotracer can take up to 45 min resulting in up 80% activity loss only through decay [11]. Furthermore, this process currently requires large amounts of

initial radioactivity, large hot cells for radiation safety purposes and specially trained personnel, which limits the use of this powerful imaging tool [40]. Microfluidic reactors have previously shown an advantage of increasing surface-area to volume ratios (up to a 50-fold increase compared to the conventional methods), inducing rapid heat and mass transfer and increasing selectivity properties for chemical syntheses. The use of a simple microchannel (serpentine or tubular, similar to Figure 1-4) and T-shaped (see Figure 1-5) microfluidic reactors for the purpose of C – 11 PET radiotracer syntheses has been widely explored. These C – 11 radiolabeling processes have displayed moderate to high RCYs as reaction conditions were optimized (see Table 1-3). In some cases higher yields were obtained with the increase in reaction times hence providing a trade-off effect. Therefore, in our investigation we hope to explore the advantages of a microfluidic chip-based technique for the synthesis of [^{11}C]MET and [^{11}C]Rac, two C – 11 PET radiotracers.

1.3.2 Thesis objectives and outline

In this investigation, we selected a passive micromixer design initially explored by Whitesides et. al. who intended to design a portable analytical system but has never been applied to a radiolabeling procedure [54]. We anticipated that the micromixer loop design can induce more mixing compared to a straight serpentine or a T-shaped microfluidic reactor by providing many twists and turns, multiple splitting and rejoining of fluid streams with collision at the rejoining-junction and also providing a longer residence time in a more compact area. One of the advantages of choosing this design is the fact that it only

requires a single layer mold to fabricate the chip, which is a simpler process, compared to a 3D- or active-micromixer design.

Furthermore, the use of a polymer (PDMS) material adds to the low cost of fabrication and is compatible with the solvents used in the [^{11}C]Rac and [^{11}C]MET synthetic process. Therefore, all these features of the design made it an attractive prototype to study the C – 11 radiotracer synthesis process. Also, the simplicity of the soft-lithography fabrication process allows for an easier design modification process for optimization and potential implementation into an automated PET tracer production instrument.

Therefore, in this investigation, we:

1. Design the continuous-flow microchip for this application.

2. Compare our microchip design to the previously investigated serpentine design microfluidic reactor.

3. Fabricate a prototype of the microchip for the purpose of experimental investigation.

4. Explore the mixing within the microchannels through computer modelling and experimental methods.

5. Carry out and analyze the non-radioactive synthesis of raclopride on the microchip.

6. Apply the optimized microchip technique for the radioactive synthesis of [^{11}C]MET.

7. Explore the applicability of the microchip design to more than one C – 11 radiolabeling process by synthesizing [^{11}C]Rac.

8. Perform a CFD analysis of the microchip technique by creating a continuous-flow microreactor model in order to investigate the yields as affected by the flow and mass transfer of reagent species on the molecular level.

2: EXPERIMENTAL

In this chapter we describe our various experimental procedures including microfluidic chip (microchip) fabrication, fluidic mixing experiments, cold (non-radioactive) synthesis, hot (radioactive) synthesis and the computer simulation.

2.1 General

The non-radioactive (cold) and radioactive (hot) syntheses were adapted from current routine production procedures for research and medical use. The desmethyl raclopride (DMR) freebase was purchased from JML Biopharm Inc. (Vancouver, BC) and ABX GmBH (Radeberg, De) and raclopride (Rac) was purchased from ABX as well. Both reagents were stored at – 20 ^{0}C until being used. The SU-8 50 photoresist and SU-8 developer solution used in the microchip molding master fabrication were purchased from MicroChem (Newton, MA) while the PDMS was made from Dow Corning's Sylgard® 184 crosslinking silicone prepolymer and curing agent (Midland, TX). Also HPLC grade solvents, dimethyl sulfoxide (DMSO), acetonitrile (MeCN) and ethanol (EtOH) were purchased from Caledon (Georgetown, ON) and Fisher Scientific (Ottawa, ON) while extra dry sure sealed bottle solvents, DMSO, MeCN and acetone, were purchased at from Sigma Aldrich, (Oakville, ON). The cleaning solvents acetone, EtOH and IPA were purchased from Commerical Alcohols (Chatham, ON). Also, water-soluble dyes made of food pigment that were used in the mixing experiments were purchased from La Cie McCormick Canada (London, ON) [60].

2.2 Polymer-glass Microfluidic Chips

In our experiments, we chose to work with PDMS, a polymer material for microchip fabrication. The advantages to this have been highlighted in the Introduction, Section 1.2.3.

2.2.1 Microchip fabrication

The microchannel design of the polymer-glass microchips was developed on a drafting software program [44]. Next, the designs were used to create a photomask (Cole litho-prep ltd, Vancouver, BC). The photomask is a printout of the microchip design on a transparency at a high resolution (3385 dpi) using a laser printer. This photomask was then used to create a molding master on a Si wafer (University Wafer, South Boston, MA) using a photolithography method (see Figure 2-3). This method involves imprinting the photomask's microstructures on a Si wafer coated with photoresist to create a polymer mold with the microchannel wells (see Figure 2-1(a) and (b)).

Barrier to hold casting polymer solution
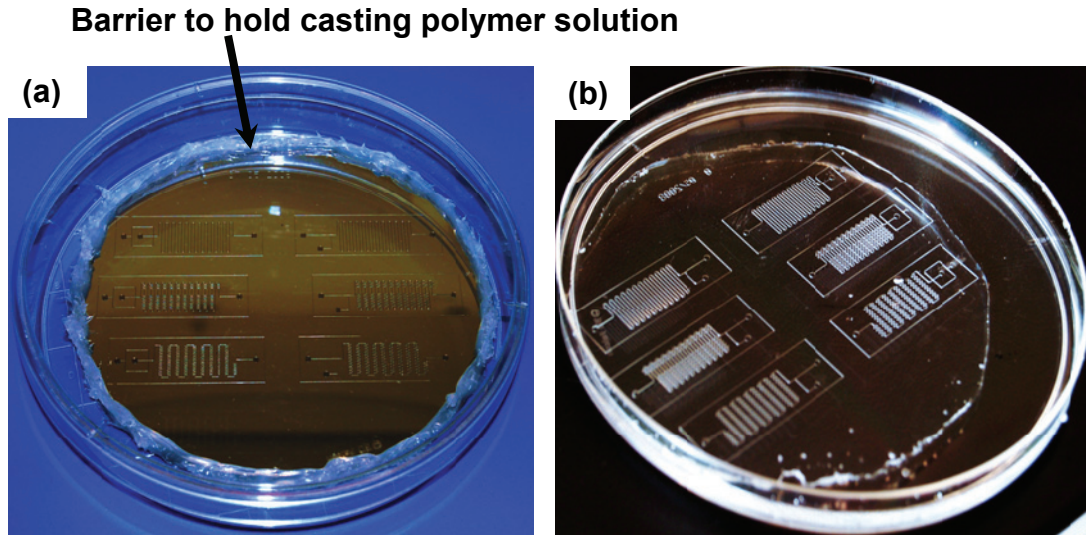
Figure 2-1 (a) Molding master consisting of a silicon wafer patterned with crosslinked SU-8 microstructures and (b) the PDMS mold with the microchannel wells corresponding to the SU-8 microstructures.

Considering that dust contamination could decrease the fabrication quality, the in-house fabrication process of these micrometer size microstructures was carried out in an enclosed clean-room module (577 series, Clean Air Products, Minneapolis, MN) with an air filtration system (see Figure 2-2(a)). The fabrication process was adapted from the SU-8 photoresist data sheets provided by the MicroChem (see Figure 2-3) [43-44, 62].
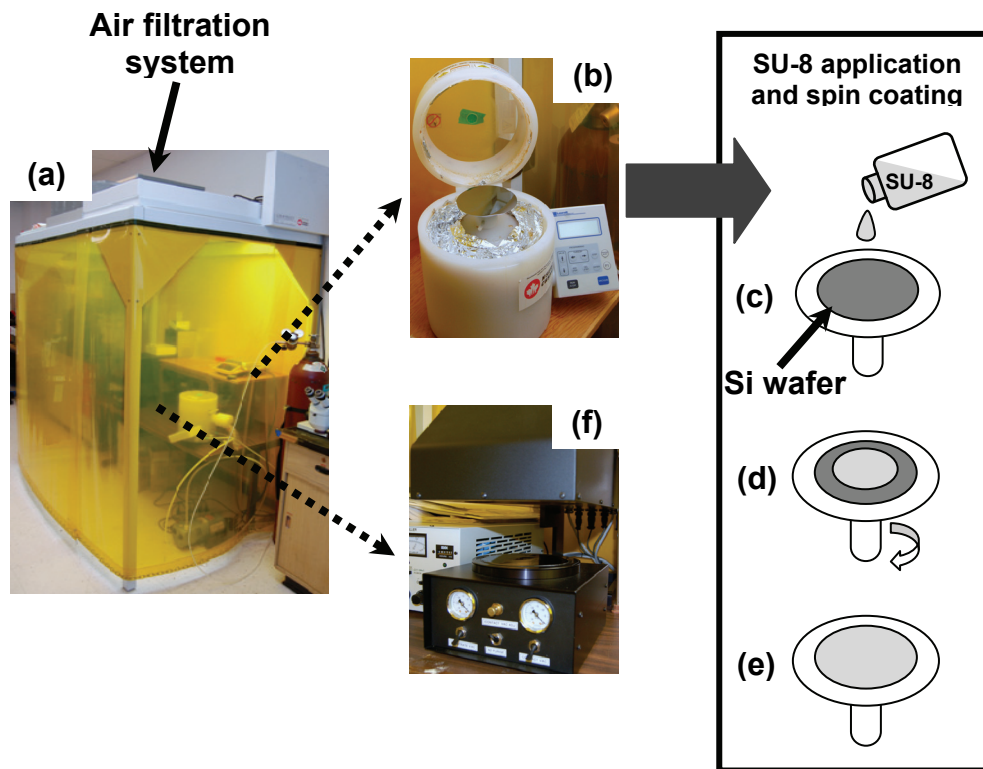
Figure 2-2 Image of, (a) the clean room and the instruments involved in the molding master fabrication. (c) SU-8 photoresist is first poured on the silicon wafer, then the (b) spin coater is used to, (d) – (e) evenly distribute a layer of SU-8 photoresist onto the silicon wafer before being exposed to near UV light using the (f) UV irradiation system [44].

Initially, a 5'' pre-oxidized Si wafer was cleaned using a piranha solution (H_2SO_4: H_2O_2 = 2.5:1). Then it was cleaned with acetone and IPA to remove any dirt, dust or grease from the surface. Next it was rinsed with DI H_2O (18 Ω), blown dry using N_2 gas and baked in a convection oven at 120 ^{0}C for 15 min to ensure complete removal of solvent residue. Next the SU-8 photoresist (Microchem) was poured on the Si wafer mounted on a spin coater (WS-400, Laurell Technologies Corporation, North Wales, PA) (see Figure 2-2(d) – (e)). According to company specifications, a 100 μm thick photoresist layer was

produced on the Si wafer surface when spun at a 1000 rpm for 30 sec. Then the Si wafer was baked on a hot plate at 65 ^{0}C for 10 min and then in the oven at 95 ^{0}C for 30 min to remove SU-8 solvent in preparation for the UV exposure (see Figure 2-3(a)). The photoresist-coated Si wafer was then placed on the UV irradiation system (Model LS-150-3, Bachur & Associates, San Jose, CA) with the photomask on top held in place with a blank glass plate [44]. Once the photomask was positioned carefully on top of the wafer, the photoresist was exposed to UV light (λ = 365 nm) for 30 s on the UV irradiation system (see Figure 2-2(d) and Figure 2-3(b)). Following this the Si wafer was baked (postexposure bake) at 65 ^{0}C for 1 min and then in the oven at 95 ^{0}C for 15 min in order to complete the crosslinking of the exposed photoresist (see Figure 2-3(c)). To dissolve the non-crosslinked photoresist, the Si wafer was then immersed into a solution of SU-8 developer for 10 min while gently being agitated (see Figure 2-3(d)). Once all non-crosslinked photoresist was removed and only the patterned microstructures remained, the molding master was rinsed with IPA and gently blown dry with N_2 gas.
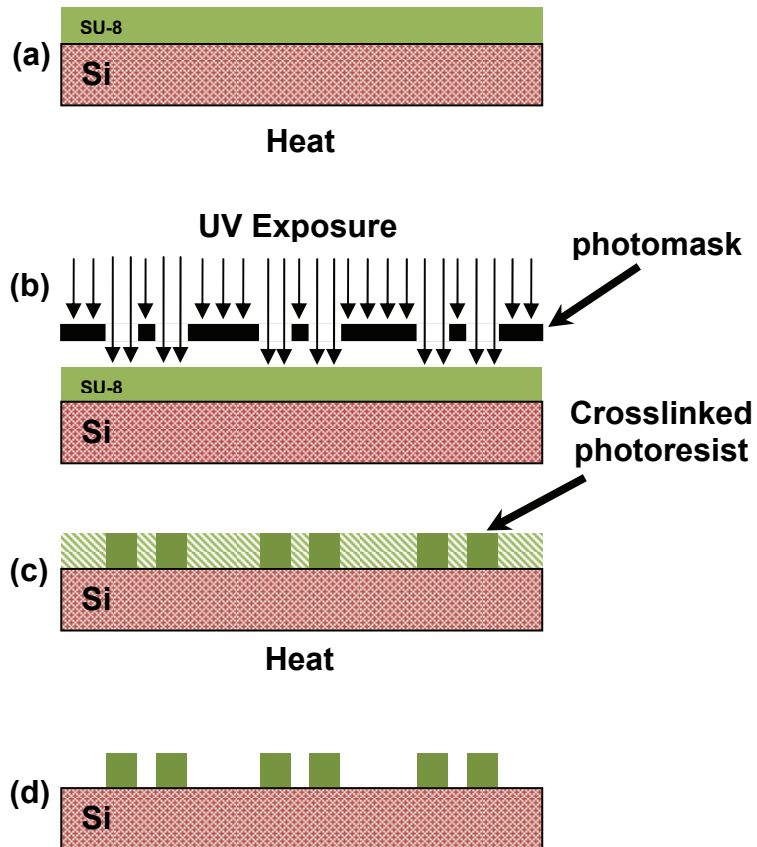
Figure 2-3 Fabrication process for SU-8 molding master, (a) pre-baking Si wafer coated with SU-8 photoresist, (b) expose SU-8 photoresist/Si to UV with the photomask on top, (c) post-exposure bake the Si wafer, (d) SU-8 photoresist/Si with microchannel pattern after being developed.

Once the molding master was created, it was used to generate the PDMS microchip (see Figure 2-4(a) – (c)). First, a barrier (Dow Corning® 732 multi-purpose sealant, Dow Corning®, Midland, MI) was created around the wafer to contain the PDMS casting solution. Then the volume required to generate approximately a 1.2 mm thick mold was calculated and a mixture composed of silicone prepolymer and curing agent in a ratio of 10:1, was mixed. It was then stored overnight at – 20 ^{0}C in order to remove air bubbles. Prior to applying the

PDMS, a thin layer of Repel-Silane (Pharmacia Biotech, Uppsala, Se) was applied on the molding master surface for easy mold release. Subsequently, the PDMS mixture was applied on the molding master and was cured overnight on a flat surface at room temperature (see Figure 2-4(a)) [32]. Once cured, the PDMS was peeled off, the microchip structures were cut-out and their inlets/outlets were punctured using a flat-tip needle.
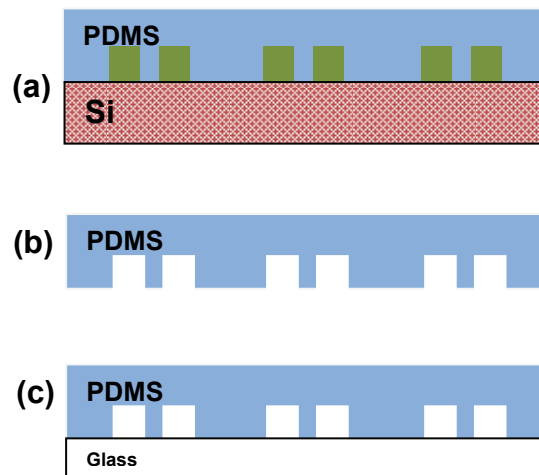
Figure 2-4 Fabrication process of the PDMS-Glass microchip from the molding master. (a) First Pour 10:1 PDMS on the molding master and let it cure to generate microchannel pattern on the polymer, then (b) peel off cured PDMS from molding master and finally (c) bond PDMS to a 0.6 mm glass wafer.

To complete the fabrication process the PDMS must be permanently bonded to a glass wafer (see Figure 2-4(c)) [32, 42, 63]. Using a point cutter, 0.6 mm thick glass wafers were cut to the same size as the PDMS microchip structures (see Figure 2-5) [32]. After thoroughly cleaning the glass wafer using a piranha mixture it was placed on a petri-dish alongside the PDMS cut out mold and subjected to air plasma treatment using a high radio-frequency (R) generator

(115 V, 50/60 Hz, 0.35 A, high radio-frequency generator, model BD-10A, Chicago, IL) (see Figure 2-5(a)) [64]. Then the PDMS and glass layers were sealed together, heated for 15 min at 95 ^{0}C and then overnight at 75 ^{0}C.
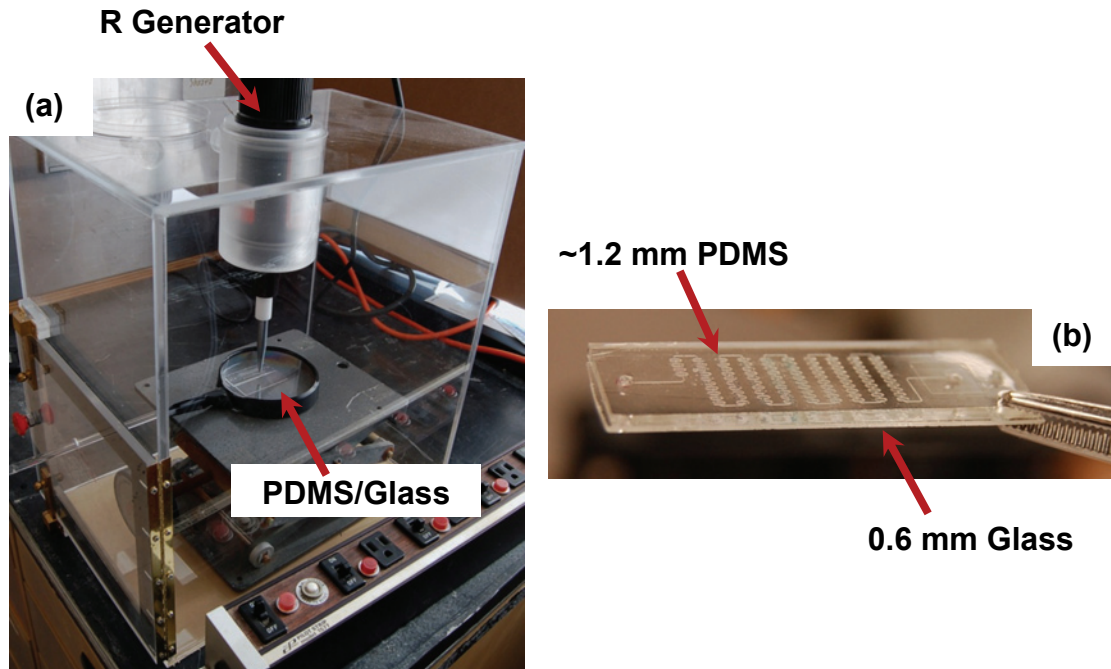
Figure 2-5 (a) Plasma bonding setup with the R generator and PDMS/glass on a flat surface inside a plexiglas chamber and (b) an image of a permanently bonded PDMS-glass microchip.

2.2.2 PDMS-glass microchips

Each molding master was used to create six different microchip designs (see Figure 2-5). The microchips' dimensions were 45 mm (length) × 15 mm (height) × ~1.8 mm (depth) with approximate channel depths of 50 μm (side inlet microchannel) and 100 μm (main inlet and microchip microchannels) (see Appendix A, Section 5.1.1, Table 5-1 for more details). The external dimensions allowed the microchip to be mounted in a microchip holder (Lab-on-a-chip kit

4515, Micronit Microfluidics, Enschede, NL) for the purpose of liquid delivery. The devices also varied in channel lengths and volume capacities. In addition, fluidic connections were made using polyetheretherketone (PEEK, Fisher Scientific) tubing with a larger internal diameter (ID) for the outlet (OD = ~1.6 mm, ID = ~381 µm) than the inlet (OD = ~1.6 mm, ID = ~178 µm) in an attempt to avoid pressure build up. PEEK material is compatible with many chemicals and is able to withstand high temperatures which is why it is commonly used in radiolabeling systems [40].

Microchip 1

(a)

Microchip 2

(d)

Microchip 3

(b)

Microchip 4

(e)

Microchip 5

(c)

Microchip 6

(f)

0.1

(g)
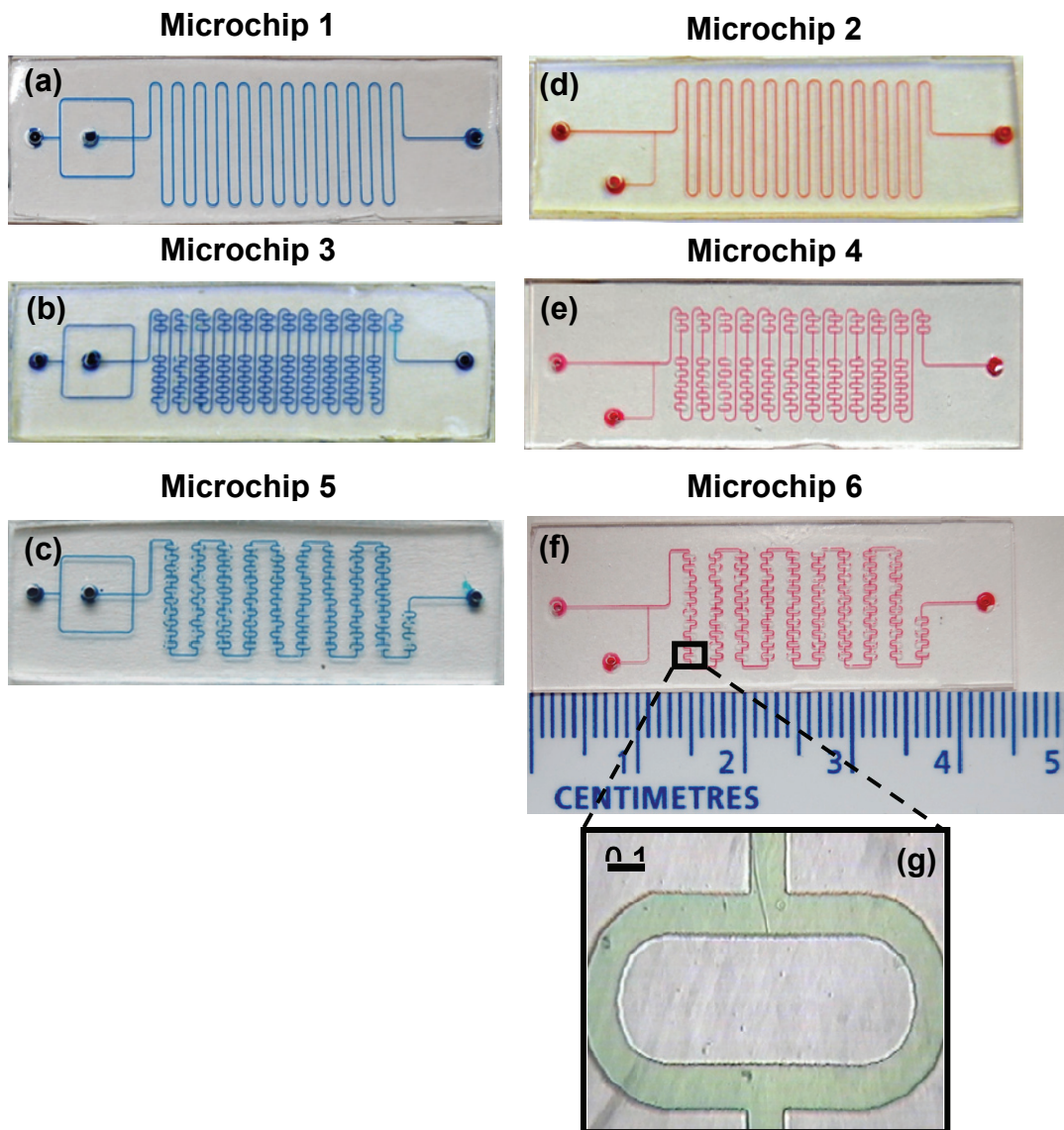
Figure 2-6 Images of the six microchip designs fabricated from one molding master. (a)-(c) Show a Cross-junction at the inlet channels for the no loop, abacus, and full loop microchip designs, (d)-(f) show a T-junction at the inlet channels for the 3 microchip designs and (g) An inset of the micromixer loop with the relative scale.

2.3 Microchip mixing experiments

For a continuous-flow liquid delivery, the microchip was mounted in a microchip holder which was connected to two syringe pumps using PEEK tubing (see Figure 2-7) [40]. The microchip holder was then placed on an inverted optical microscope (WPI, Sarasota, FL) platform and using a CCD camera (IV – CCAM2, Industrial Vision Source, Farmers Branch, TX). Images and video footage were captured at different locations on the microchip.
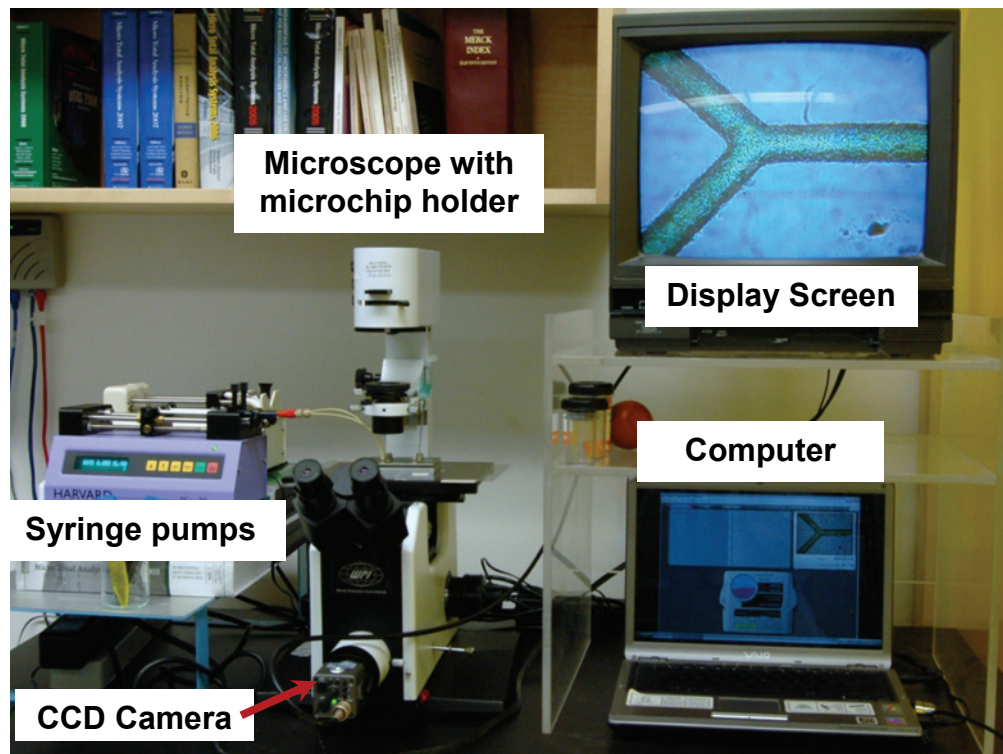
Figure 2-7 Mixing experiment setup with an inverted optical microscope, two syringe pumps, CCD camera, TV and computer to investigate liquid mixing behaviour within the microchannels.

Fluid interaction was examined by flowing two liquid streams simultaneously into the two inlets of the microchip using two syringe pumps

(Harvard Apparatus, Saint-Laurent, QC, see Figure 2-8) [59]. Blue-colored MeCN and yellow-colored DMSO were introduced at various flow rates (2, 6 and 12 µL/min) using syringe pump 1 and syringe pump 2 respectively.
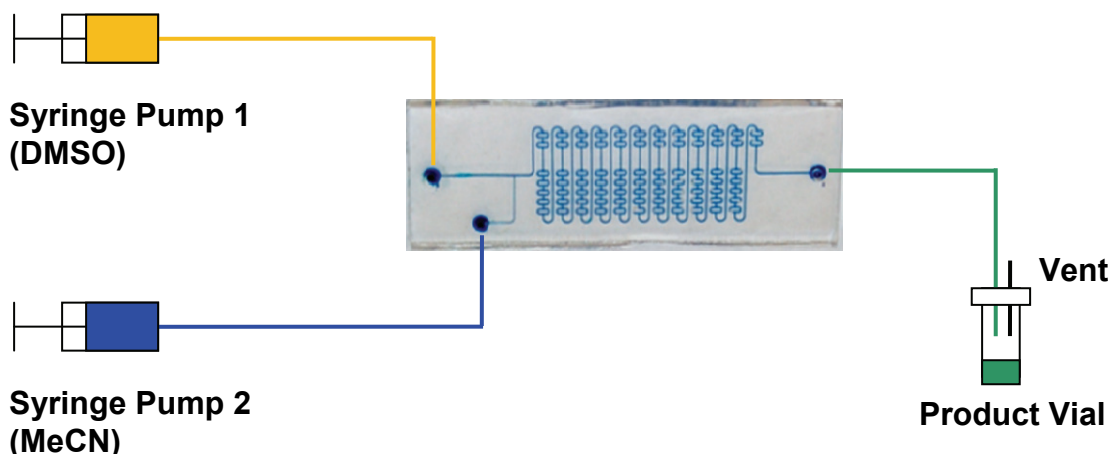
Figure 2-8 Experimental setup for liquid-liquid mixing experiment.

2.4 Temperature calibration

Temperature calibration experiments were carried out in order to investigate difference in temperature between the hot plate dial and the surface. The temperature was calibrated by placing a thermocouple probe (digital dual channel thermometer, VWR) on the hot plate surface. Temperature readings were recorded every 30 s and the values were plotted to determine the temperature difference between the expected value from the hot plate dial reading and the measured value on the surface of the hot plate. This was done for 15 – 20 min, which appeared to be the time for the temperature to stabilize, then the temperature was increased by 10 ^{0}C and the measurement was

repeated for the new temperature setting. This calibration was done with the microchip-holder (with the Aluminum base) placed on top of the hot plate (see Figure 2-9).
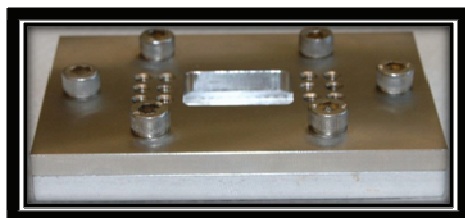
Figure 2-9 Microchip holder with Aluminum bottom machined at the SFU science technical centre.

2.5 Conventional cold raclopride synthesis

The conventional non-radioactive reaction was carried out in our lab by dissolving DMR (~4.2 – 5.1 µmol) in 400 µL of dimethylsulfoxide (DMSO) and adding 7 µL of 5 M NaOH in a 3 ml micro reaction v-shaped vial (v-vial) (Sigma Aldrich) (reaction scheme shown in Scheme 1-5). Methyl iodide (MeI) (dissolved in 0.75 ml HPLC-grade MeCN) was then bubbled into the reaction vial with the aid of a nitrogen gas flow (see Figure 2-10). This was done while continuously stirring the reaction solution using a Barnstead hot plate/stirrer (Thermo Scientific, Asheville, NC) and maintaining the water bath temperature at 76 – 82 ^{0}C. After continuously bubbling MeI for ~8 – 10 min, the reaction vial was removed from the water bath and cooled to room temperature. Then 1 ml of 0.1 M ammonium formate (HCOONH$_4$) was added to the solution to quench the

reaction (at ~15 min). The time of the various steps (preparation, MeI addition and quenching) was around 22 min in all runs.
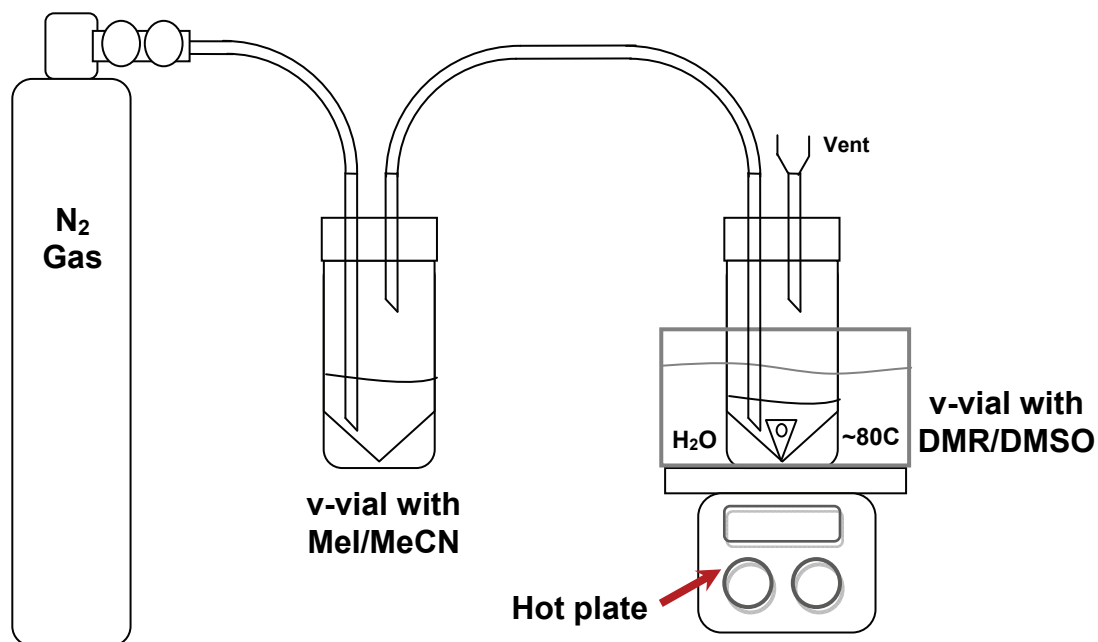
Figure 2-10 Schematic of the conventional methylation process setup.

Then the products were analyzed by reversed phase HPLC (HP1050, Agilent Technologies, Mississauga, ON) using an Agilent, Zorbax column (C18, 4.6 mm x 250 mm) with a mobile phase composition of 70% sodium dihydrogen phosphate (NaH_2PO_4, with 2% phosphoric acid (H_3PO_4) added) : 30% MeCN with UV detection at 240 nm. A calibration curve of 1:1 DMR:Rac with 2.5, 5, 25, 50, 250, 500 µM concentrations was used to quantify the Rac amounts in the product solution.

2.6 Microfluidic synthesis

2.6.1 Microchip cold Rac synthesis

In the cold Rac synthesis, DMR (2.4 – 3.9 µmol) was dissolved in 400 µL of DMSO and mixed with 7 µL of 5 M NaOH solution. In another vial 7.5 µL of MeI was added to HPLC-grade MeCN (0.15 - 0.75 ml). Then both solutions were loaded on two separate syringes and the experiment was carried out using a setup similar to the one shown in Figure 2-11. After loading the syringes, the hot plate temperature was calibrated (see Appendix A, Section 5.1.2). Then at a flow rate of 8 µL/min on each pump (16 µL/min for both), the precursor solution and the MeI solution were dispensed into the microchip where product samples were collected. Each reagent batch that was loaded on to the syringes was used for multiple runs where different product samples were collected at varied temperatures and collection times. For each run the product sample was immediately neutralized using a 0.1 M ammonium formate (HCOONH$_4$) solution. Then the microchip was cleaned after completing each experiment with a continuous flow of MeCN for future reuse.

The product sample was then analyzed using HPLC (HP 1100, Agilent) with a C18 column (Zorbax, 4.6 mm X 150 mm, Agilent) or C8 column (Zorbax-SD C8, 3.5 mm X 150 mm, Agilent) and a UV detector (λ = 240 nm). The mobile phase composition for analysis was 70% of an aqueous solution containing 5 mM NaH$_2$PO$_4$ (with 2% H$_3$PO$_4$ added) and 30% of MeCN. The Rac yield was then quantified using an internal standard (IS), 2,4-dihydroxybenzoic acid (see Appendix A, Section 5.1.3). Then the yields were calculated according to the

estimated initial DMR concentration used for each run according to the flow rate and collection time (see Appendix B, Section 5.2.1).

2.6.2 Radioactive synthesis of [^{11}C]MET

[^{11}C]MET synthesis involved using a setup which was similar to the Rac cold synthesis. However, a rotating collection vial holder was fabricated in Al to facilitate vial switching during consecutive collections (see Figure 2-11). This reduced the user's hand exposure to radiation through reduced contact. Additionally, for radiation safety purposes, less activity was generated using shorter (3 – 7 min) cyclotron beam irradiation times compared to the conventional production process (30 – 60 min). Also, experiments were carried out in a shielded fumehood for further protection (see Figure 2-12(a)).
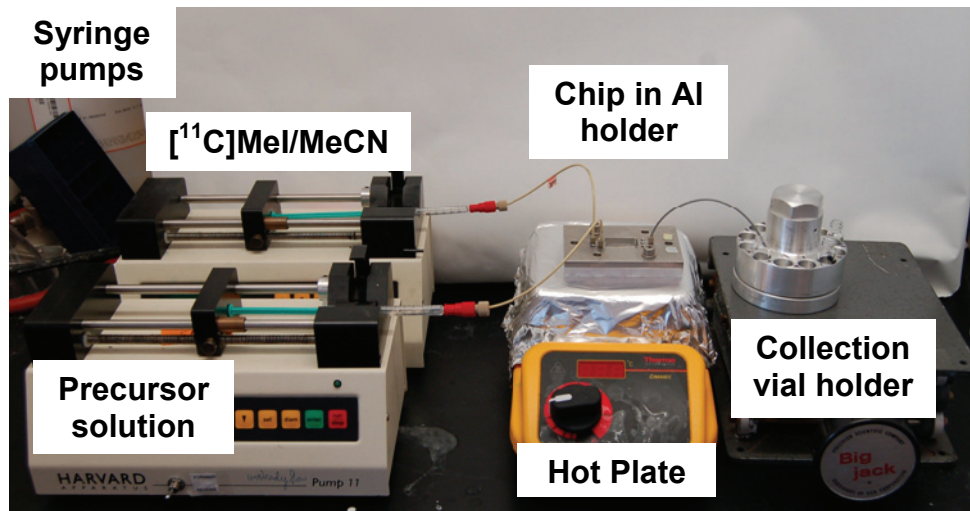
Figure 2-11 Microchip synthesis reaction setup in which syringe pumps are used to deliver the precursor solution (DMR in DMSO) and [^{11}C]MeI solution (in MeCN).

[^{11}C]MET was synthesized from L- homocysteine thiolactone HCl (L-homo) (Fluka Biochemika, Buchs, CH) and cyclotron-generated [^{11}C]MeI (see Scheme 1-3). A TR-13 (13 MeV, EBCO technologies, BC) cyclotron was used to produce [^{11}C]CH$_4$ at 13 MeV, through the irradiation of N$_2$ gas in the presence of H$_2$. [^{11}C]CH$_4$ was then processed and converted into [^{11}C]MeI in an semi-automated system. Initially, 3.3 – 4.6 μmol of L-homo was dissolved in EtOH:H$_2$O (~200:200 μL) and mixed with 2.75 μL of 5 M NaOH solution and [^{11}C]MeI was trapped in EtOH:H$_2$O (~250:150 μL). Both reagent solutions were loaded into separate syringes and the experiment was carried out as shown in the previous setup in Figure 2-11. At a flow rate of 10 μL/min, reaction temperatures and collection times were varied for multiple runs within the same experiment.
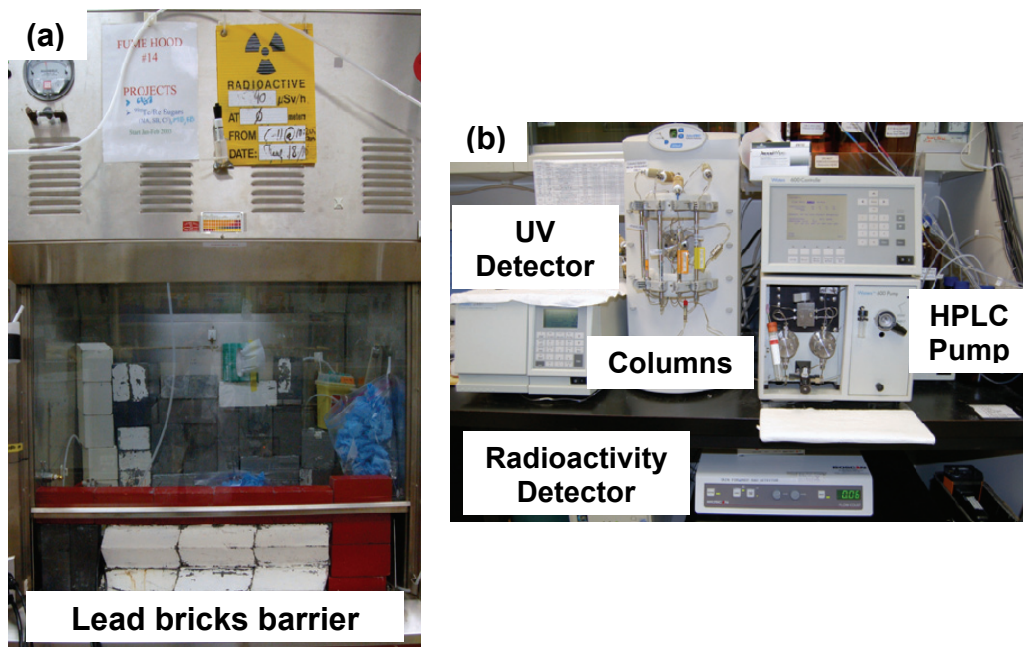
Figure 2-12 (a) Fumehood with lead bricks for protection against high activity exposure. (b) HPLC setup for radiochemistry analysis with the column → UV detector → radioactivity detector connected in series.

After completing the experiment, the microchannels were flushed with solvent in order to dissolve any accumulated residue, which can cause contamination with the reuse of the microchip. Then the neutralized crude (un-purified) product samples were analyzed using a HPLC system (Waters 200E, Waters Limited, Mississauga, ON) with a C8 column (Zorbax-SD C8, 3.5 mm X 150 mm, Agilent technologies, Mississauga, ON). Detection was carried out using a Waters 2487 dual wavelength absorbance detector (λ = 254 nm) and a radioactivity detector (NaI(Tl)/PMT, FC-6106, photodiode, Bioscan, Washington, DC) (see Figure 2-12(b)). In general, the scintillation material used for radioactivity detection is selected according to its light output and energy

resolution. In this case the NaI-Thalium activated scintillation crystals were used for the HPLC radioisotope detection due to their efficient energy output at a low cost and since energy resolution isn't a concern when working with only positron emission. The detector used converts linear pulses from radioactive decay (counts per minute = cpm) into a voltage (6×10^6 cpm = 1 V) which is plotted against time [65]. The HPLC method for this process consisted of a solvent gradient of 100% NaH_2PO_4 with 2% H_3PO_4 (buffer with a pH ~ 3) from 0 – 2 min at 0.5 mL/min, which was gradually increased from 2 – 4 min to 10% buffer and 90% MeCN with an increase in flow rate to 1 mL/min [18, 20]. The column was flushed after each run with a 9:1 of buffer:MeCN (~4 min), followed by 1:1 buffer:MeCN (~ 4 min) and finally back to 100% buffer (~ 2 min). Using the HPLC data, [^{11}C]MET relative activities were calculated in order to evaluate the efficiency of the radiolabeling process.

Subsequently, EtOH was replaced with acetone since it has been used in the literature as an alternative solvent for the efficient synthesis of [^{11}C]MET. Reactions were carried out with L-homo dissolved in acetone:H_2O (~200:100 µL) and mixed with 2.75 µl of 5 M NaOH solution while cyclotron-generated [^{11}C]MeI was trapped in acetone:H_2O (~200:100 µL). For this process the HPLC analysis used a mobile phase composition of 3:7 buffer:MeCN and flushed for 3 – 5 min using with the same ratio.

2.6.3 Radioactive synthesis of [^{11}C]Rac

Next DMR and [^{11}C]MeI were used to synthesize [^{11}C]Rac in the same setup as the [^{11}C]MET synthesis. Similarly, the TR-13 cyclotron was used to

produce $[^{11}C]CH_4$ at 13 MeV, which was processed and converted into $[^{11}C]MeI$ in a semi-automated system. Then the $[^{11}C]MeI$ was trapped in 250 – 300 µL of extra dry MeCN. A few minutes before the $[^{11}C]MeI$ trapping, DMR (1.5 – 2.4 µmol) was dissolved in ~250 – 300 µL of extra dry DMSO in a reaction vial and mixed with 7 µL of 5 M NaOH solution. Each reagent batch that was loaded on to the syringes was used for multiple runs where different product samples were collected at varied temperatures, flow rates, reaction modes (flow mix and premix) and collection times [40].

After experiments were complete, the microchannels were flushed with the reaction solvent, similar to the $[^{11}C]MET$ synthesis. Then the neutralized crude (un-purified) product samples were analyzed using the same UV-HPLC (214 nm) and RAD-HPLC instrument and column as $[^{11}C]MET$. The mobile phase consisted of ~37:63 MeCN and 5mM potassium dihydrogen phosphate (KH_2PO_4, pH ~ 2.8) (see Figure 2-12). Then the relative activities and RCYs were calculated using the estimated initial $[^{11}C]MeI$ decay-corrected activity and the measured crude product sample decay-corrected activity [22, 66] (see Appendix B, Section 5.2.2.2). Also the $[^{11}C]MeI$ conversion was calculated in order to correct for losses due to experimental procedures (see Appendix B, Section, Appendix 5.2.2.2).

2.7 Computational Fluid Dynamics (CFD)

After the experimental investigation we carried out a computational study of our microchip geometry and reaction kinetics using COMSOL Multiphysics® (COMSOL), a CFD software. For our investigation we used COMSOL's reaction

engineering lab (REL) and the microelectromechanical systems (MEMS) modules. Initially the REL module was used to investigate the reaction kinetics and generate the "ideal" microreactor conditions where it was assumed that reagents are perfectly mixed [67]. Then the flow and mass transfer within the microchannels was modeled using the MEMS module's incompressible Navier-Stokes equation and Convection and Diffusion (Convection-Diffusion) equation. Finally, the reaction kinetics setup on the REL module were coupled with the flow and mass transfer model in order to investigate the reaction progress in our microchip geometry by varying the conditions such as the flow rate, reagent concentrations, diffusion coefficient, rate constant (k) and reaction mode.

2.7.1 Reaction engineering lab (REL) – "ideal" flow-reactor model

For our model, the reactor type was set to a plug-flow reactor (PFR) (see Figure 2-13). This means that there is balance of liquid in-flow and liquid out-flow in the given reactor, which reflects the behavior in a continuous-flow microfluidic reactor. This balance of liquid flow also reflects a balance of species molar flow (F) through the microreactor (see Equation 2-2). In this case for a species A, the change in position along the x (ΔV) direction shows a change in the species concentrations (ΔF_A) due to the progress of the reaction.
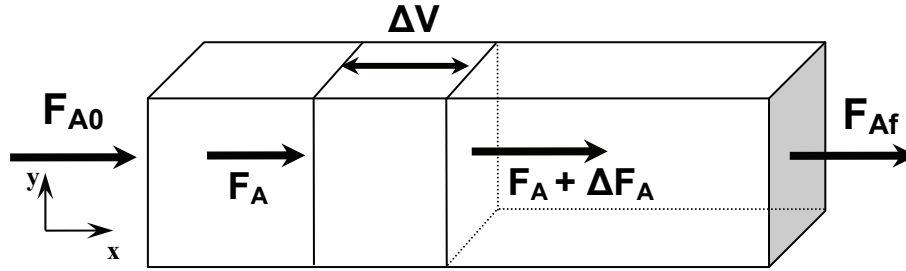
Note: F_{A0} = specified initial molar flow rate of species A at the inlet and F_{Af} = collected final molar flow rate of species A at the outlet.

Figure 2-13 Schematic of a plug-flow reactor showing the change in the molar flow rate of species A (F_A) as the liquid travels down the reactor (adapted from [67-68]).

Furthermore, the species mass balance is represented by [67]:

Equation 2-1 Mass balance (mmol/L·s).

$$\frac{dF_i}{dV} = R_i$$

Where F_i is the molar flow rate (mol/s) which represents the mass flow of the species i, V is the microfluidic reactor volume (m^3) and R_i denotes the rate of the reaction of species i (mmol/L·s). The species molar flow rate, F_i for DMR and MeI was calculated using the following equation:

Equation 2-2 Molar flow rate (mol/s).

$$F_i = c_i \cdot v$$

Where c_i (mmol/L) refers to the concentration of species while v (L/s) is the volumetric flow rate of the species throughout the microchannel (in-flow and out-flow) [67].

54

Therefore for the 2nd order reaction, $DMR + MeI \rightarrow Rac$, the overall reaction rate value was,

Equation 2-3 Rate of reaction for Rac synthesis (mmol/L·s).

$$R_{overall} = k \cdot c_{DMR} \cdot c_{MeI}$$

Where k (L/mmol·s) denotes the rate constant. While, the generated species rate of reaction equations are shown in Table 2-1.

Table 2-1 Shows the R_i equations for the reaction species in the hot and cold synthesis simulations

Species	Cold synthesis	Hot synthesis
R_{DMR}	-k[DMR][MeI]	-k[DMR][MeI]
R_{MI}	-k[DMR][MeI]	-k[DMR][MeI] – λ[MeI]
R_{Rac}	k[DMR][MeI]	k[DMR][MeI] – λ[Rac]

Note: The generated species reaction rate equation were modified for the hot synthesis scenario in order to incorporate the decay factor (see Table 2-1) [69-70].

In this investigation, two plug-flow reactors PFR 1 (3.10× 10^{-10} m³, 31.0 mm) and PFR 2 (4.56×10^{-10} m³, 45.6 mm) were modeled and compared. After acquiring results for different variables (concentrations, flow rates and k see Table 2-2) on both PFR 1 and PFR 2, the progress along the microreactors' length was evaluated using the calculated yields. Then the conditions were exported to COMSOL's MEMS module for the "space-dependent" simulation.

2.7.2 MEMS module – "space-dependent" model

2.7.2.1 Geometry settings

The microchip design was modified where only the 1st or 2nd meanders of the microchannels were kept as the design's reaction "repeating" unit (see Figure 2-14). These shorter repeating unit (RU) geometries were modeled in 2D for simplicity and memory limitation.
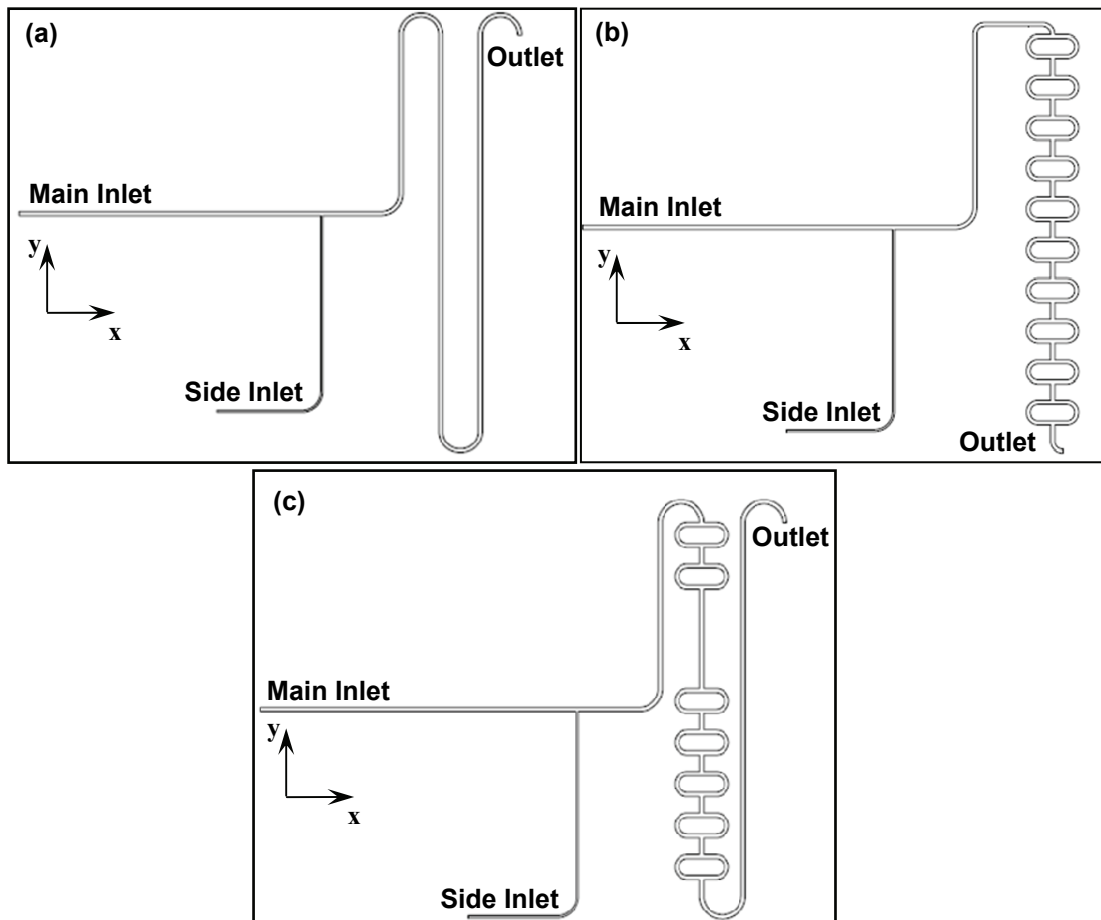
Figure 2-14 Schematic of (a) no loop, (b) full loop and (c) abacus microchips' RUs used for the microreactor "space" model.

2.7.2.2   Momentum balance

In the microchannels, flow is represented by a continuity equation where fluids are treated as incompressible species with constant densities in space and time (see Equation 2-4) [56].

Equation 2-4 Continuity equation for incompressible fluids [56].

$$\nabla \cdot \mathbf{u} = 0$$

Where, u denotes the velocity in the microchannels (m/s). The Navier-Stokes equation is a continuous non-linear differential equation used to calculate the pressure-driven flow within the microchannels (see Figure 1-7 and Equation 2-5) [56]. This equation defines the species momentum which is controlled by its carrier solvent flow field property and is dependent on the microchannel geometry.

Equation 2-5 Incompressible Navier-Stokes equation [71].

$$\rho(\mathbf{u} \cdot \nabla) \cdot \mathbf{u} = \eta \nabla^2 \mathbf{u} - \nabla p + \mathbf{F}$$

Where, p equals the pressure (Pa), η denotes the dynamic viscosity (Pa·s), F is a body force term (N/m^3) which incorporates the force exerted by the fluid volume on the microchannel walls [56, 71]. For this investigation the default (water) dynamic viscosity (η = 10^{-3} kg/m.s) and density (ρ = 10^3 kg/m^3) values were used for the carrier solvent. Also, the inlets were exposed to various initial velocities (u_0) for a pressure-driven flow. These u values were calculated from the experimental volumetric flow rate (m^3/s) and inlet cross-sectional area (m^2) (see Equation 2-6) [56, 72].

Equation 2-6 Flow rate determination.

$$u = \frac{v}{(w \cdot h)}$$

Where, w and h are the inlet width and height. In addition, the microchannel walls due to laminar flow property are set to zero-velocity (no slip condition). On the other hand, the outlet boundary condition is set to no viscous stress with $p_0 = 0$ since the flow property within the microchannel is unaffected as the fluid exits through the outlet.

2.7.2.3 Mass balance

The mass transport in the microfluidic reactors is assumed to be diffusion-controlled and can be described using Fick's first law of diffusion (see Equation 2-7). This is a valid assumption unless micromixer structures (passive or active) are introduced to the channel design [29].

Equation 2-7 Fick's first law of diffusion.

$$J = -D\Delta n$$

Where, J is the diffusive flux (mol/m^2·s), describing the flow of a substance through small area over time and Δn is the change in particle density or concentration over diffusion distance [26, 29, 56, 71]. In this case, the diffusion time (t) is defined by Equation 2-8:

Equation 2-8 Diffusion time as a property of diffusion distance and the diffusion coefficient of the species [26].

$$t = \frac{x^2}{D}$$

Where, x (m) is the diffusion distance travelled by the diffusive process and D (m^2/s) is the diffusion coefficient of the diffusing species. This corresponds to the distance travelled by the species in order to mix.

These properties representing the mass transfer were then studied with the use of the general Convection-Diffusion equation (see Equation 2-9).

Equation 2-9 Convection-Diffusion equation [72].

$$\frac{\partial c_i}{\partial t} + \nabla \cdot (-D_i \cdot \nabla c_i) = R_i - (\mathbf{u} \cdot \nabla c_i)$$

Where, D_i (m^2/s) is the diffusion coefficient of species i (e.g. fluorescein, D = 5 ×10^{-10} m^2/s), c_i (mmol/L) is the concentration of species i and u is the velocity (m/s) [73]. Where R_i denotes the rate of reaction term (mol/(L·s)) identifying the rate of consumption or production of reaction species. Initially, the Convection-Diffusion equation was solved at a steady state for the micromixing investigation where there are no on-going reactions ($\partial c_i/\partial t = R_i = 0$) in the microchannels (see Equation 2-10).

Equation 2-10 Convection-Diffusion equation at steady-state [72].

$$\nabla \cdot [(-D_i \cdot \nabla c_i) + (c_i \cdot \mathbf{u})] = 0$$

On the other hand, the Convection-Diffusion equation generated from exporting the REL data already took into account the reaction species and rate equations (see Equation 2-3). Consequently, the flow properties defined by the Navier-Stokes equation were coupled to the Convection-Diffusion property in order to generate the microreactor synthesis model.

2.7.2.4 Mesh generation

A free (unstructured) triangular mesh was generated with a maximum side-length of 15 μm (see Figure 2-15) [72]. This created a very fine mesh for all the 2D geometries as shown by the example in Figure 2-15. The number of mesh elements for the 3 microchip designs (no loop, abacus and full loop) was ~50505, ~69789 and ~67716 for microchannel lengths of 31.0 mm, 42.8 mm and 45.6 mm, respectively.

(a)

(b)
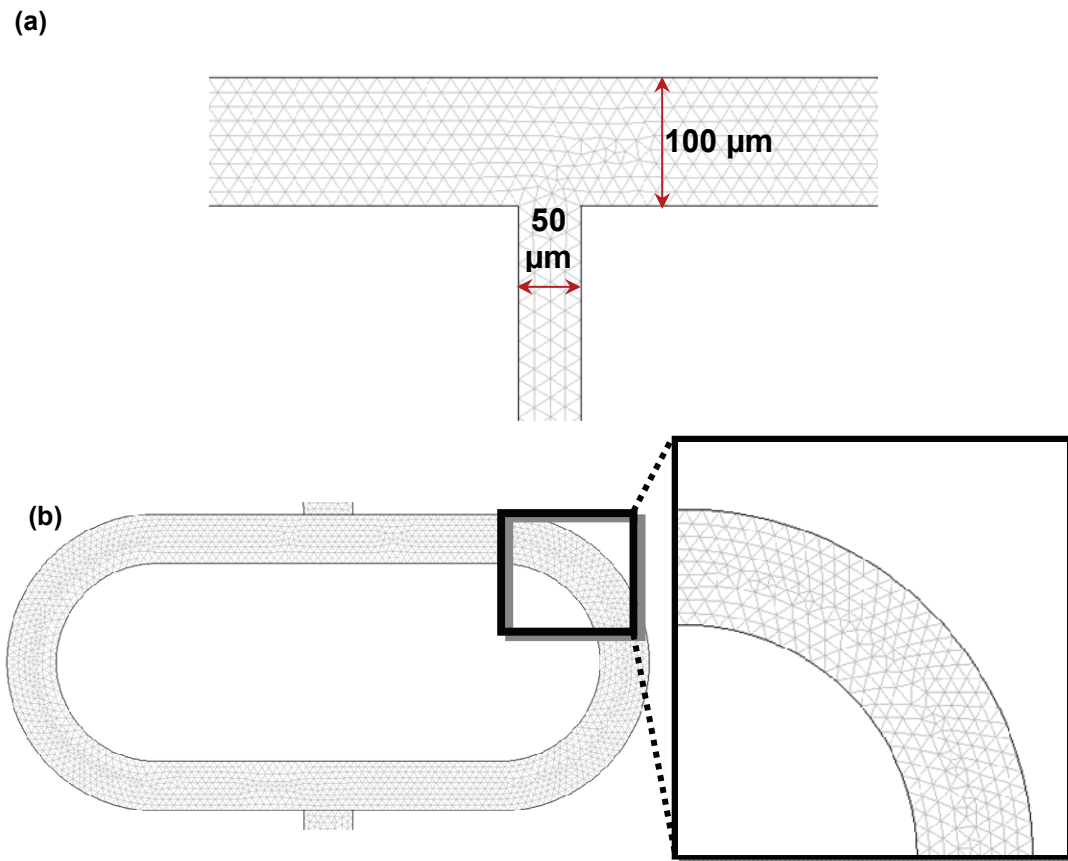
Figure 2-15 Shows the mesh generated mesh in (a) the Inlet T-junction, (b) a micromixer loop and (c) an inset zoomed into the micromixer loop.

2.7.3 Input parameters

The combined default values that were used for the simulations include using a flow rate of 15 µL/min and a k = λ L/mmol·s (where, λ = 5.663×10^{-4} s^{-1} is the decay constant for the C – 11 activity) (see Scheme 1-1) [70, 74]. Also the default D value was set to 10^{-9} m^2/s. In addition, DMR and MeI concentrations used were based on the experimental investigation, with the high concentrations reflecting the cold synthesis and the low concentrations reflecting the hot synthesis. Moreover, the parameters were varied accordingly (see Table 2-2).

Table 2-2 Shows the range of inputted parameters for all simulations.

Parameter	Cold synthesis	Hot synthesis
Flow rate* (µL/min)	2 – 15	2 – 15
Reagent concentration (mmol/L)	DMR: 21.6 MeI: 53.4	DMR: 21.6 MeI: 0.024
k value range (L/mmol·min) **[69-70, 74]**	$10^{-4}\lambda$, $10^{-2}\lambda$, λ	$10^{-4}\lambda$, $10^{-2}\lambda$, λ
D (m^2/s)	10^{-8}, 10^{-9}	10^{-8}, 10^{-9}

Conversion to volumetric flow is shown in Appendix A, Section 5.1.5.1 in Table 5-7.

Furthermore, given that the reaction solutions were dilute, the solvent species were considered the dominant species. Hence, it was assumed that the momentum of the solute (reagents) species is dependent on the diffusion coefficient of the reaction solvents (DMSO and MeCN) [72, 75-76]. The values were estimated using the table of diffusion coefficients of dilute binary liquid mixtures (~1 – 5 × 10^{-9} m^2/s) [76]. Also, as stated in the Handbook of Chemistry

and Physics increasing the temperature by 10 ^{0}C, generally increases the diffusion coefficient values by 10 – 20% [76]. Hence, increasing the temperature by 100 ^{0}C would increase the values by 100 – 200%. The values ranged from ~1 – 5 × 10^{-9} m^2/s and an increase in temperature by 100 ^{0}C would increase these values to 2 – 10 × 10^{-9} m^2/s. Therefore, the D values used, 10^{-8} and 10^{-9} cover this range.

2.7.4 Data Analysis

Initially, the mixing experiments performance was evaluated through the concentration distribution plots and final outlet concentration. Furthermore, in the chemical reaction investigations the final outlet concentration was used to calculate the Rac yields, which were then compared for the different processes to evaluate the reaction efficiency. The standard deviations for the CFD values were as low as 10^{-5} % and 10^{-3} % for Rac yields in the hot and cold synthesis investigations respectively and hence were disregarded.

Furthermore, for the purpose of comparison between the various investigations (e.g. microchip design and reaction mode), the calculated yields were normalized with respect to the default settings. In the REL module synthesis investigation the calculated Rac/[^{11}C]Rac yields were normalized with respect to the PFR 1 (31.0 mm) simulation final yield (outlet) at default parameters (flow rate = 15 μL/min, k = 5.663×10^{-4} (L/(mmol·s)), with [DMR] = 21.6 mmol/L and [[^{11}C]MeI] = 0.024 mmol/L). Meanwhile for the MEMS module the hot synthesis investigation values were normalized with respect to the no loop microchip simulation outlet yield at default parameters (flow rate = 15

µL/min, k = 5.663×10^{-4} (L/(mmol·s)) with [DMR] = 21.6 mmol/L and [^{11}C]MeI = 0.024 mmol/L in flow mix mode). The yield patterns were used to evaluate the effect of the parameters and were compared in the "space-dependant" model to the REL calculations and the experimental values.

3: RESULTS AND DISCUSSION

3.1 Microfluidic connections

Modifications were made to the commercial, microchip holder (Micronit Microfluidic's lab-on-a-chip kit, stainless steel top and PEEK base) and PEEK tubing (with ferrules and nuts) to better fit our experimentation process. Despite being fabricated of PEEK (glass transition temperature = 143 – 150 ^{0}C and melting point = 343 ^{0}C), the chip holder base experienced a change in shape at temperatures above 100 ^{0}C [77]. After heating during an experiment the PEEK chip holder base's texture increased in stiffness and decreased in size making it hard to fit a microchip in the well. It was suspected that the PEEK material warped as it approached its glass transition temperatures. Therefore, an aluminum (Al) microchip holder base replica was fabricated with similar dimensions (see Figure 3-1(b)). This was beneficial for working with higher temperatures in our experiments and hence was adapted for the synthetic processes.
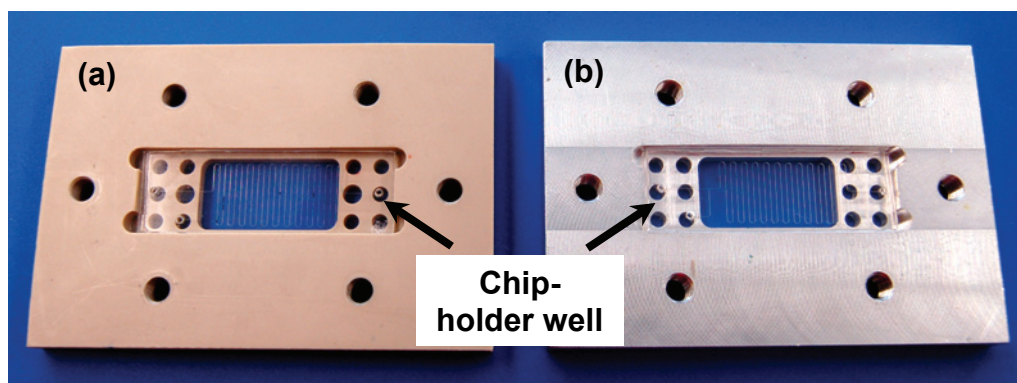
Figure 3-1 Microchip holder (a) PEEK base and (b) Al base that was fabricated in-house.

Furthermore, the flat PEEK tubing and punctured inlet reservoirs on the PDMS-glass microchips did not provide a good connection as some liquid leaks were observed. To resolve this problem the PEEK tubing was tapered by shaving off the edges at a $30^0 - 45^0$ angle (see Figure 3-2(d)). This modification allowed the tubing to be inserted further into the inlet reservoir, providing a better seal. This modification was inspired by the Micronit Microfluidic's microchip connection where the flat-surfaced PEEK tubing was sealed against a conical shaped reservoir for an efficient fluid delivery (see Figure 3-2(e) and (f)).
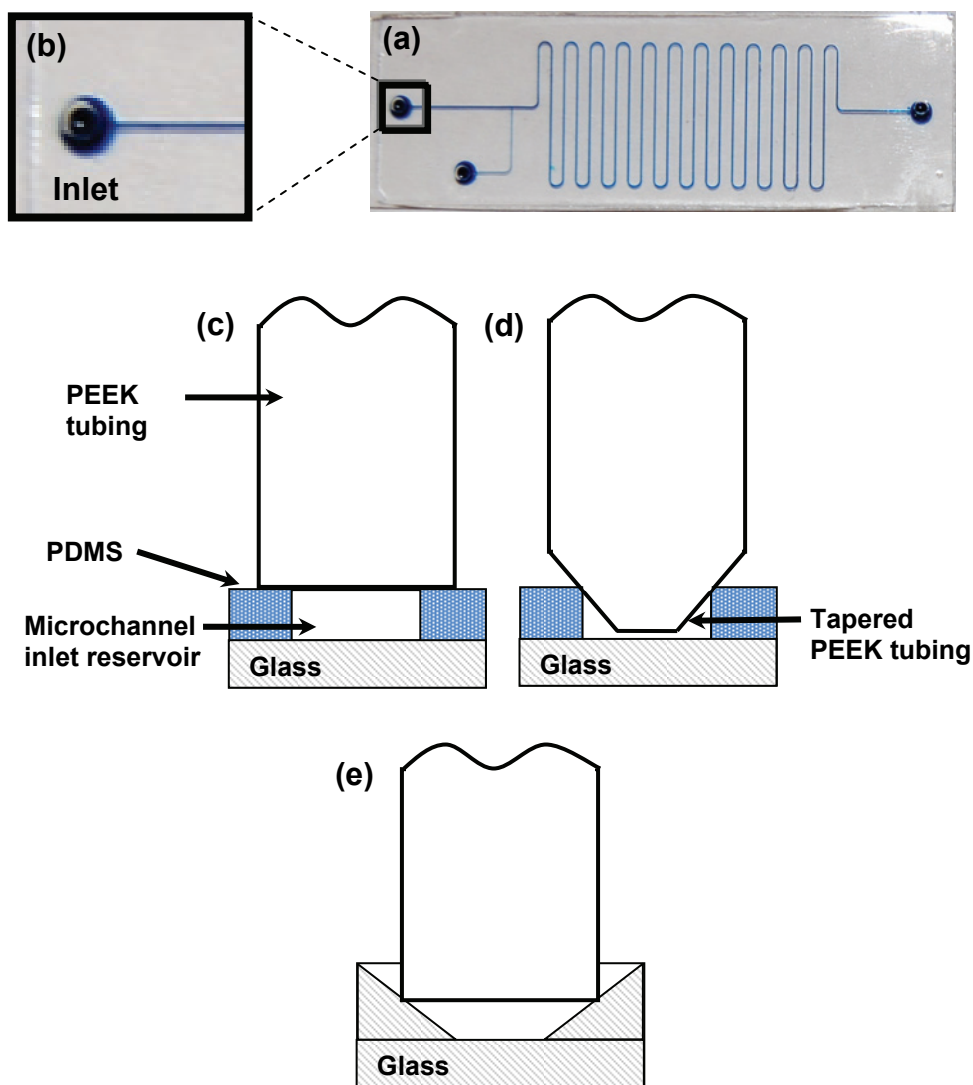
Figure 3-2 (a) Microchip 2 with an inset showing the (b) microchannel inlet reservoir filled with blue dye. Schematic of (c) Flat bottom PEEK tubing and (d) tapered PEEK tubing fitting on the microchip surface. (e) A schematic of PEEK tubing fitted into the Micronit Microfluidics tapered reservoir [78].

Due to the relatively high levels (30 – 60 mCi) of radioactivity that were used for C – 11 synthesis, manual sample collection and handling was not desired. Therefore, this necessitated the manufacturing of a rotating vial holder for multi-sample collection, as inspired by an auto-sampler vial holder on an

Agilent HPLC system (see Figure 3-3). The Agilent HPLC vial holder is electronically controlled to rotate freely while positioning vials for fluid dispensing and injection. In practice, the prototype seen in Figure 3-3(b) makes use of a ball and spring to suspend the top section and allow for its free rotation. As well, the use of the spring helps in removing and inserting the PEEK tubing into the vials by pressing down or releasing the rotating top section. This device and the use of tongs reduced the user's hand exposure to radiation.
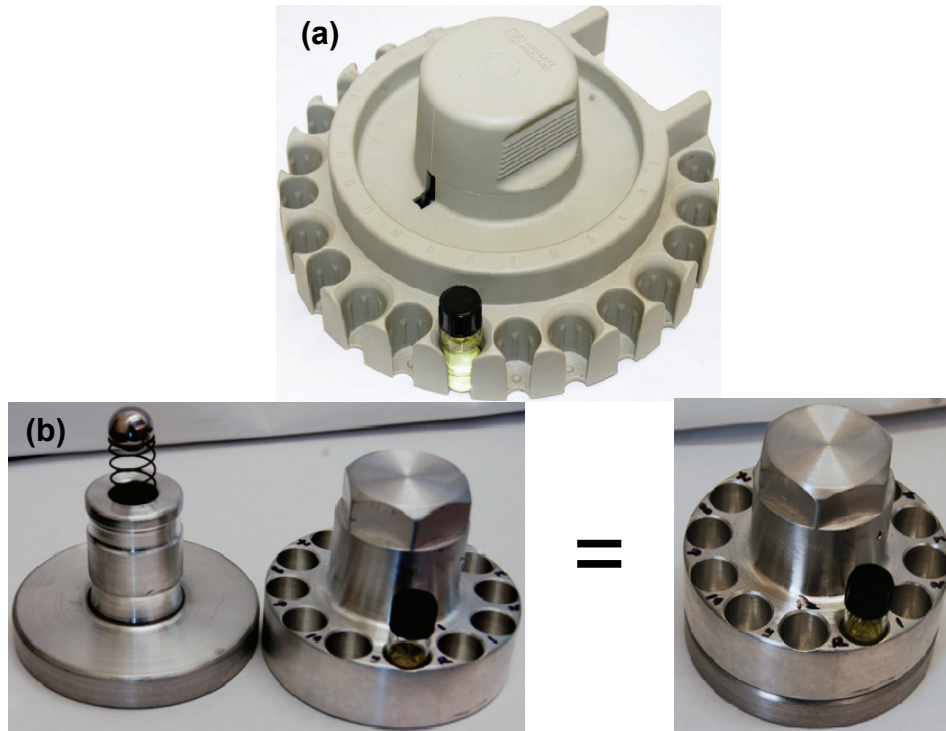
Figure 3-3 (a) HPLC auto-sampler vial holder of an Agilent 1050 HPLC system and (b) In-house built Al vial holder base with ball and spring and rotating top.

3.2 Microchannel mixing

The mixing efficiency of the microchips was investigated by flowing two miscible reaction solvents DMSO and MeCN within the microchannels at various flow rates. Colored-dye was added to DMSO (yellow) and MeCN (blue) in order to observe their liquid flow and mixing behaviour inside the microchannels. Using the optical microscope, a partial green-colour was seen as early as the first meander indicating the mixing of the two dyed liquids (see Figure 3-4(c) and (g)). This optical observation was seen in both serpentine (no loop) microchips (i.e. microchip 1 with a Cross-junction injector and microchip 2 with a T-junction injector) indicating that a larger surface-area in the microchannels induces efficient mixing of the two liquids [60-61].

Furthermore, the T-junction design was compared to the Cross-junction design (the flow focusing geometry) at the inlet channels (similar to Figure 1-8(f)). The flow focusing geometry induces a 3-stream liquid flow, of 2 MeCN streams (blue) from the two side channels and a DMSO stream (yellow) from the main channel (see Figure 3-4(a)). Despite their differences, both geometries showed a fully mixed, green coloured liquid at the channel leading to the outlet (see Figure 3-4(d) and (h)).

(a) Inlets Cross-junction **(b) Inlets' meander** **(c) 1st meander** **(d) Outlet channel**

(e) Inlets T-junction **(f) Inlets' meander** **(g) 1st meander** **(h) Outlet channel**
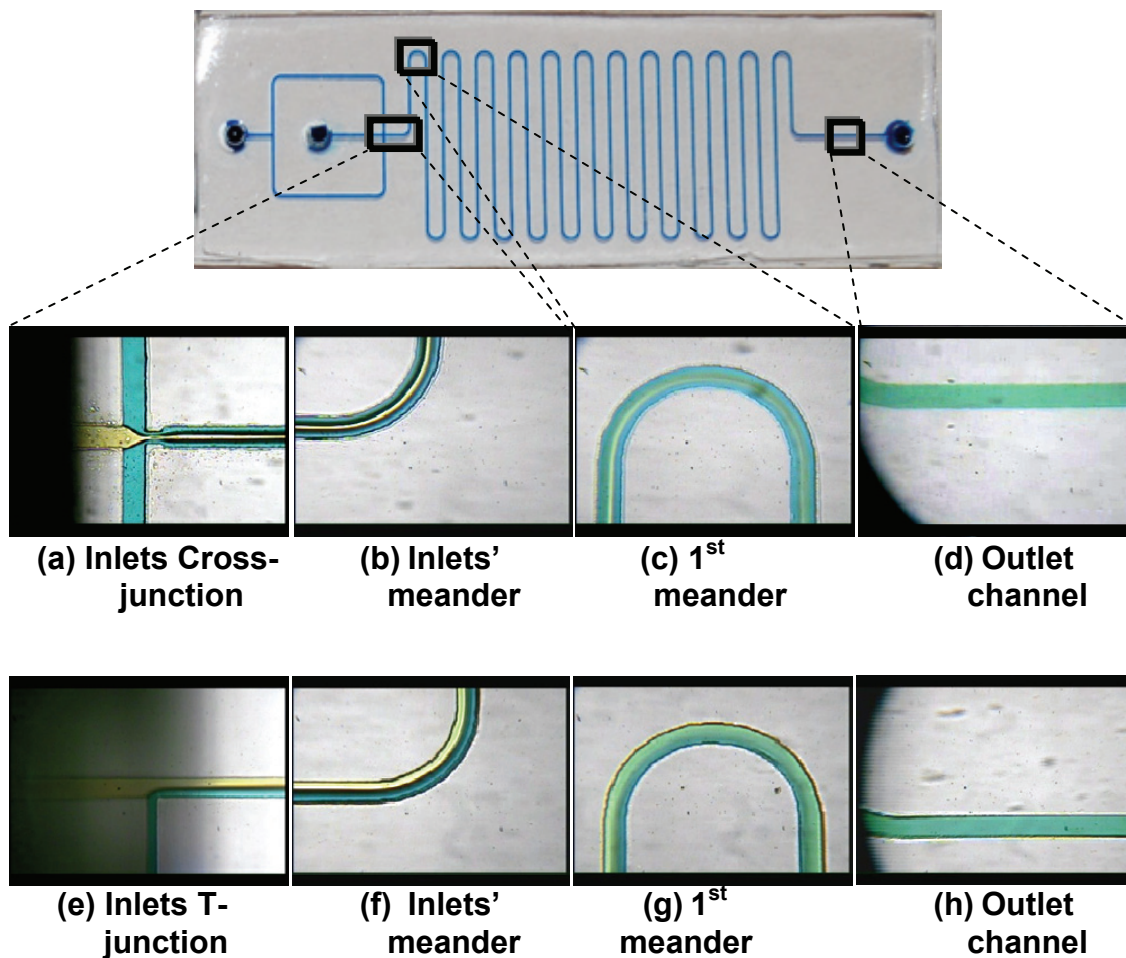
For a picture of all the microchip designs, see Figure 2-6.

Figure 3-4 Dye mixing results on the no loop microchip 1 (a – d) and microchip 2 (e – h) at 12 µL/min using DMSO (yellow) and MeCN (blue).

Moreover, liquid flow and mixing experiments were also conducted on microchip 4 (the abacus design with the T-junction injector) with the micromixer loops incorporated into the microchannels (see Figure 3-5).
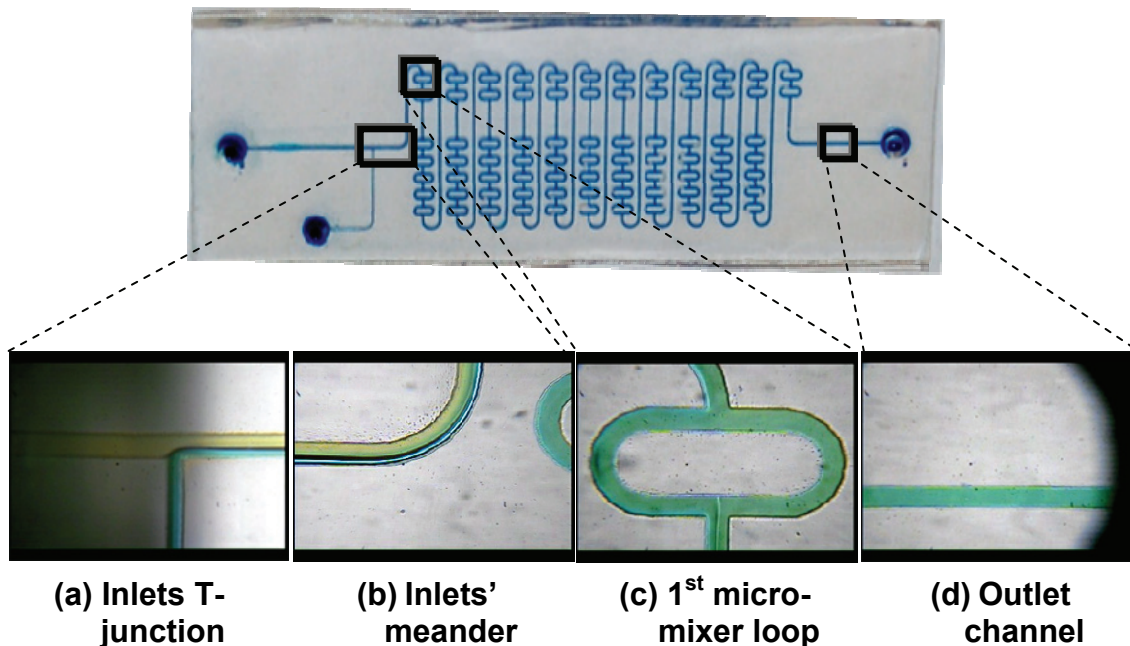
Figure 3-5 Dye mixing results on the abacus design microchip 4 at 12 µL/min using DMSO (yellow) and MeCN (blue).

Here a mixed green colour was seen as early as the first loop in the first meander (see Figure 3-6(c)). When examining the microchannel leading up to the first micromixer loop in the abacus design, it was apparent that decreasing the flow rate shows faster mixing in the microchannel past the T-junction (see Figure 3-6(a)). Therefore, the time for diffusion was greater at a lower flow rate (with the same diffusion distance see Equation 2-8) encouraging species interaction even before the fluid enters the mixing channels.

2 µL/min 6 µL/min 10 µL/min 12 µL/min
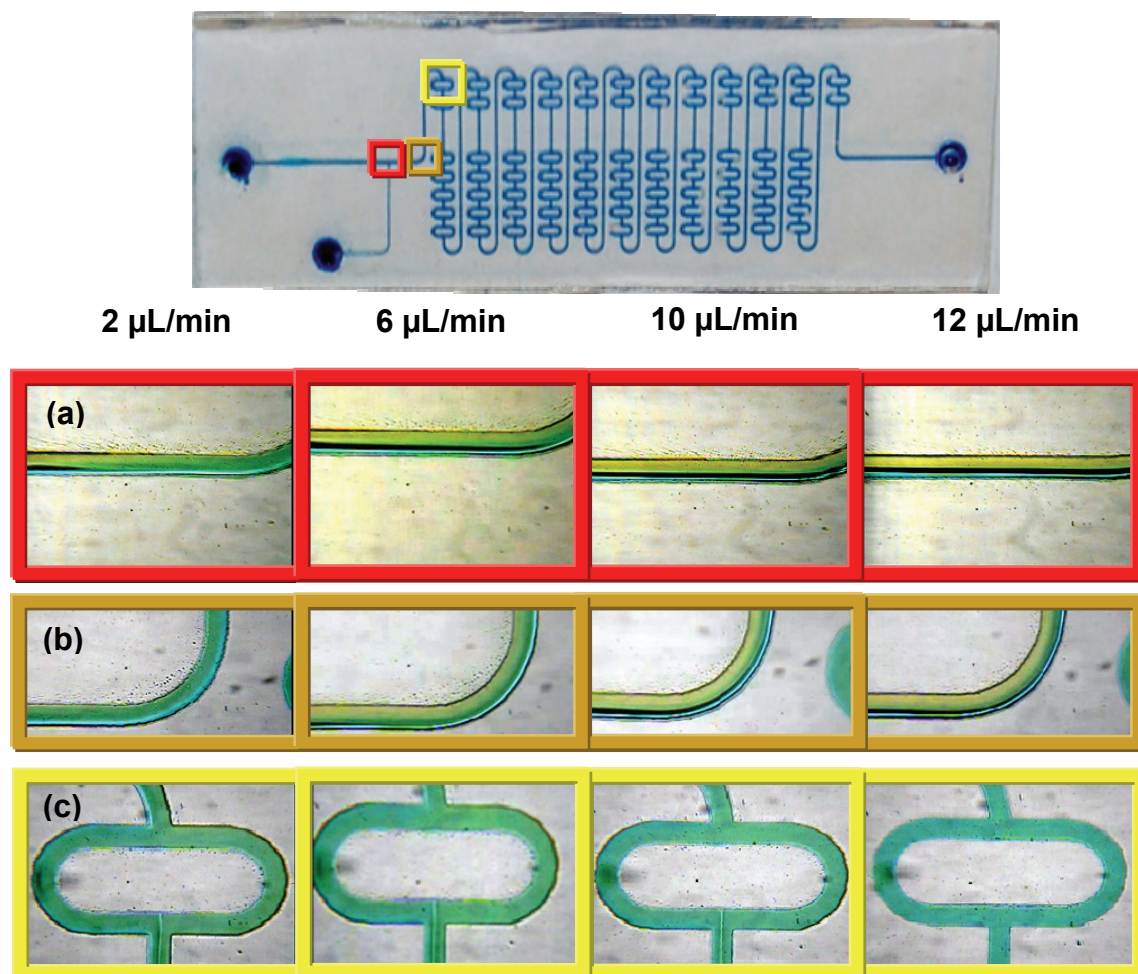
Figure 3-6 Dye mixing results on the abacus design microchip 4 at different flow rates using DMSO (yellow) and MeCN (blue).

Although it was apparent that at different flow rates the amount of mixing past the T-junction was affected, there was no clear difference in the green colour intensity at the outlet channel for microchip 1, 2 and 4 (see Figure 3-5(d)). From the given results the Cross-junction and T-junction showed efficient mixing and were both used for the synthesis process.

3.3 Rac Cold synthesis: Conventional and Microchip

Initially, the non-radioactive or cold synthesis was explored on the PDMS-glass microchip. The results obtained from the different microchip designs were compared to each other and to the cold conventional synthesis. For each collection vial the Rac yield produced by the microchip cold synthesis was determined through an internal standard (IS) method (see Appendix A, Section 5.1.3, Figure 5-3 for a chromatogram that displays peaks for the IS, DMR and Rac). Various standard solutions with known IS, DMR and Rac concentrations were used to generate an HPLC calibration curve. Then the product aliquots were mixed with a known IS concentration during HPLC analysis in order to calculate the Rac concentration. Using this method, the effects of the reagent concentrations and reaction temperatures on the Rac yield using the microchip designs were examined.

Since DMR (2.4 – 3.9 µmol) was the limiting reagent and was in low amounts, the variation of the MeI (120.2 µmol) concentration was explored. The MeI concentration introduced into the microchannels was varied in 3 different runs with 3 min collections during the same continuous-flow experiment. It was found that as the MeI concentration was decreased the yield also decreased (see Figure 3-7). Reducing the MeI concentration from 801.4 mM to 267.1 mM showed a decrease in yield by a factor of 3 (17.1% to 5.1%). This was a result of reduced species interaction for this 2nd order reaction due to a decrease in reagent concentrations which probably reduced the rate of Rac production.
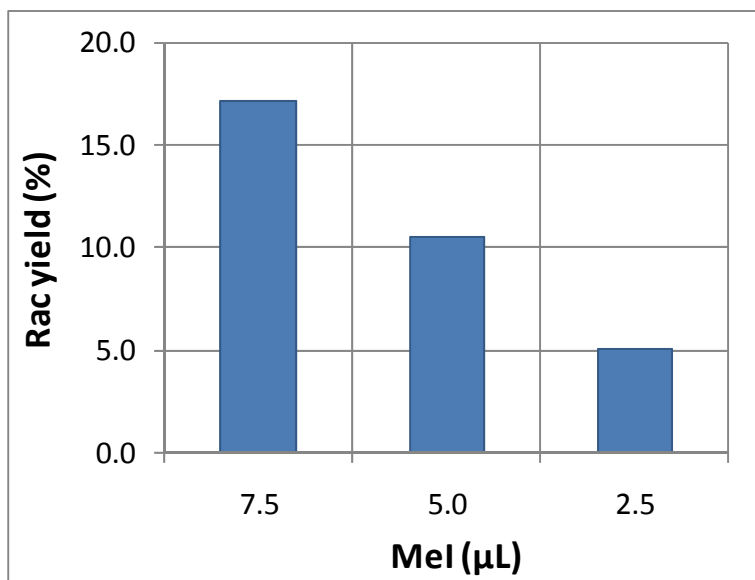
Note: In each reaction, 0.1 μmol (in 400 μL) of DMR was used. Experiments were carried out on the abacus microchip (see Figure 2-6), at 82 ^{0}C and 8 μL/min with a collection time of 3 min. Standard deviation according to the calibration curve was <0.7%. All reaction temperatures were calibrated; see Appendix 5.1.2 for more details.

Figure 3-7 Cold synthesis of Rac using different MeI concentrations (7.5, 5.0 and 2.5 μL which corresponds to 801.4, 534.3 and 267.1 mM respectively) in a 150 μL of MeCN.

Furthermore, temperature optimization experiments were also performed on the no loop, abacus and full loop microchips. The reaction temperature was varied for different runs during the same experiment. From the UV chromatograms it was observed that the unreacted MeI peak (detected at ~13.1 min) would decrease with the increase in temperature (see Figure 3-17). In turn, the Rac peak (detected at ~11.3 min) would increase along with the generation of side products (e.g. peak at ~6 min).
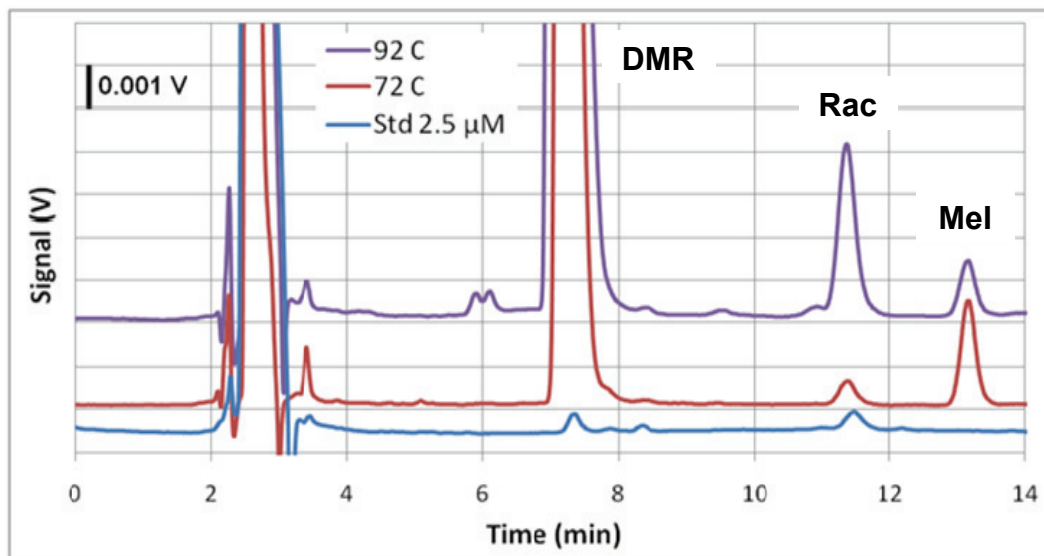
Note: The FR used was 8 μl/min at ~5.1 min and ~5.2 min collection times on the abacus microchip with 0.3 μmol of DMR and 120.2 μmol of MeI (RT: ~7.2 minutes) used in each reaction run. DMSO (solvent) was detected at 2.6 min, excess DMR was detected at ~7.8 min, the Rac produced was detected at ~11.3 minutes and excess MeI was detected at 13.1 minutes.

Figure 3-8 UV-HPLC chromatogram for a temperature variation experiment of the microchip Rac cold synthesis process overlaid with a standard Rac and DMR 2.5 μM mixture.

Additionally, further optimization experiments carried out on the other microchip designs displayed a similar effect where the yield was affected by an increase in temperature (see Table 3-1). It was also observed that the full loop microchip design demonstrated the highest yield even at a lower temperature than the other 2 microchip designs. This might be attributed to a higher ratio of the number of micromixer loops to channel length (loop: length), in the full loop microchip (0.26 mm^{-1}) compared to the abacus microchip design (0.18 mm^{-1}).

Table 3-1 Rac cold synthesis results on the no loop, abacus and full loop microchip designs at 62 – 92 ^{0}C.

Temperature (^{0}C)	Rac yield (%)		
	No Loop (microchip 1)	Abacus (microchip 3)	Full loop (microchip 5)
62	-	2.8 ± 0.7	12.1 ± 2.8
72	0.7	3.3 ± 0.1	-
82	1.3	5.8*	-
92	2.2	-	-

Note: Reaction conditions include using 0.2 – 0.4 µmol (in 400 µL) of DMR and 120.2 µmol of MeI in 750 µL in each reaction at the a flow rate of 8 µL/min in each inlet (16 µL/min for both inlets). All reaction temperatures were calibrated (see Appendix A, Section 5.1.2, Figure 5-1 and Figure 5-2 for more details). Standard deviation according to the calibration curve is <0.7% for the data shown except for data where errors represent standard deviation of 2 – 3 experimental results. For the raw data of Rac concentrations see Appendix A, Section 5.1.2, Table 5-3.
*For a sample calculation see Appendix B, Section 5.2.1.

Moreover, it was confirmed that both microchips that incorporate the micromixer loop design produce higher yields compared to the no loop microchip. It was believed that the micromixer loop design induces mixing through the split-recombine path of the reagent streams. Also, the split-recombine path increases the microchannel length, increasing the reagents' exposure to high temperatures and reaction time, possibly contributing to the higher yields.

In addition, the conventional cold Rac synthesis process was carried out for comparison to the microchip-based technique (see Table 3-2). An experiment on the full loop microchip at optimal conditions showed a ~2-fold increase in Rac yield compared to the conventional cold synthesis (see Table 3-2). This was also achieved with reduced amounts of DMR (~1/20) and MeI (~1/40) and at an

estimated temperature that was lower than the conventional process. This pattern of increased yields with reduced reagents and lower temperatures was also observed with the abacus design.

Table 3-2 Rac synthesis parameters and yield comparison in the conventional and microchip cold synthesis.

	Conventional (Macro)	Full Loop (*Microchip)
DMR (µmol)	4.2	0.2
MeI (µmol)	~120.2	3.2
Reaction time (min)	15	2.5
Ave Temperature (˚C)	78	62
Rac yield (%)	4.6	9.3

Note: The microchip experiments were carried at a flow rate of 8 µL/min. The results obtained for this conventional process showed a 4.4 ± 0.2% (n = 2) yield at ~80 ˚C for an average reaction time of 16 min.

Also, the microchip experiments resulted in less side products as shown by cleaner baselines than those of the conventional experiments (see Figure 3-8 and Figure 3-9). To explain this, the product in the microchip process was separated from the on-going heated reaction in the microchannel during each experimental run (or each product collection). The reaction was also quenched immediately using ammonium formate preventing further reactions from occurring in the collection vial. Meanwhile, the conventional process uses a reaction vessel that contains reagents and products under high temperature conditions until the end of the reaction when ammonium formate is added.
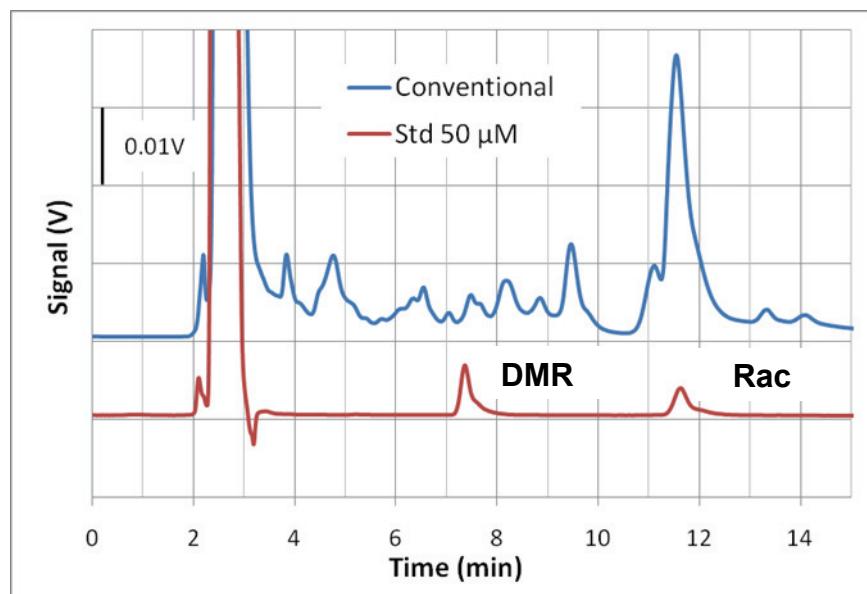
Note: The conventional experiment was carried out at 78 ^{0}C using 4.2 μmol of DMR and ~120.2 μmol of MeI resulting in a 4.6% Rac yield.

Figure 3-9 UV-HPLC chromatogram of the product vial of the conventional cold synthesis of Rac and standard solution containing DMR and Rac (1:1) 5 μM.

Consequently, we have demonstrated that the use of the microchip has improved the synthesis results in comparison with the conventional process. This improvement can be attributed to the larger surface area to volume ratio provided by the small microchannels (100 μm × 100 μm) which could result in better mass (mixing) and heat transfer and thus higher yields. Moreover, reducing the reagent amounts for the microchip process still showed yields that were higher than the conventional method. Therefore, optimal conditions for the microchip cold synthesis (~0.2 – 0.4 μmol of DMR, a flow rate of ~8 μL/min and a temperature of 82 ^{0}C) were used as a guideline for the microchip radiolabeling process which is explored in the next section.

3.4 Microchip hot synthesis

3.4.1 [^{11}C]MET synthesis

[^{11}C]MET production is known to be an efficient radiolabeling process with up 90% final radiochemical yields (RCY). Therefore, this synthesis was explored on our microchip to provide some insight on the design's potential applicability to a C – 11 radiotracer production [8, 19-20].

[^{11}C]MET was synthesized on the microchip using a similar procedure to the microchip cold synthesis of Rac with the exception of using different reagents. Cold MeI was replaced with [^{11}C]MeI and L-homo was used as the precursor (see Scheme 1-3). Since the [^{11}C]MeI concentrations are much lower than the precursor (L-homo) concentrations in the hot synthesis (by a factor of ~10^4), this was considered a pseudo-first order reaction. The [^{11}C]MET synthesis initial reaction conditions were based on the optimized microchip cold synthesis parameters. To start, the temperature variation effect was studied using the regular reaction mode (flow mix – where reagents are introduced into the microchannels through separate inlets) at a flow rate of 10 µL/min.

At the end of each experiment, the reaction product mixture for each run was analyzed by HPLC, using a UV detector and a radiation detector, as shown in Figure 3-10. In Figure 3-10, the lower trace represents the UV-HPLC while the upper trace represents the inverted RAD-HPLC. On the lower trace a clear MeI mass (C – 12) peak was observed and on the upper trace the radiolabeled [^{11}C]MeI and [^{11}C]MET peaks were detected. Since the detectors are in series, the peaks were expected to appear consecutively. For example, the C – 12 mass

peak (~2.4 min) for MeI was detected ~0.1 min before the radiolabeled compound (~2.5 min).
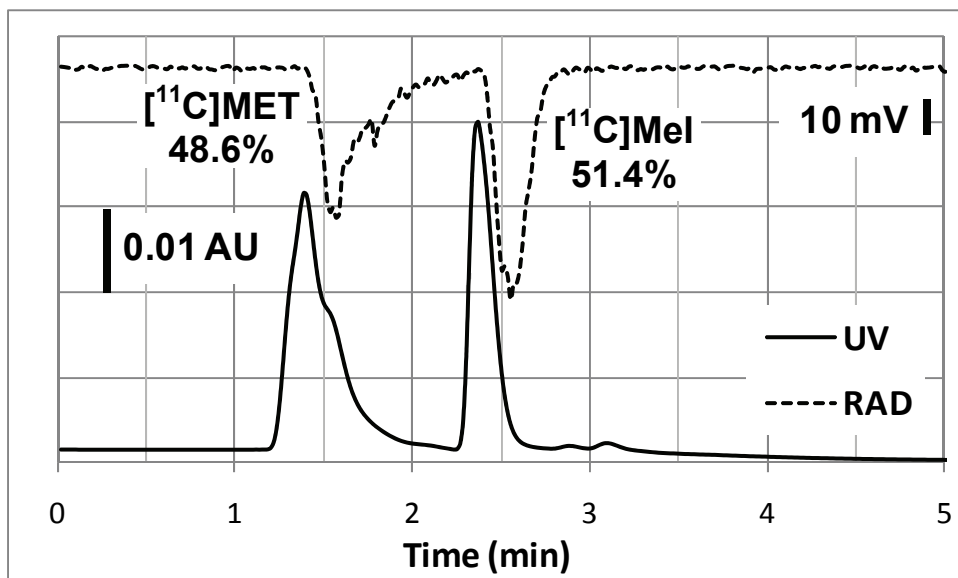
Note: MET and L-homo were detected at ~1.4 – 1.8 min on the UV-HPLC and [11C]MET was detected at ~1.6 min on the RAD-HPLC. MeI and [11C]MeI were detected at 2.4 min (UV-HPLC) and 2.6 min (RAD-HPLC), respectively.

Figure 3-10 UV-HPLC and RAD-HPLC for a product sample using the full loop microchip at 42 ^{0}C and a flow rate 10 µL/min in EtOH/H$_2$O.

[11C]MET production was evaluated by calculating the final relative activity in each collected sample using the radiochemical data (RAD-HPLC) (see Equation 3-1). Equation 3-1's numerator value is obtained from [11C]MET's peak area and the denominator accounts for the peak areas of all the C – 11 compounds ([11C]MET, unreacted [11C]MeI and side products = the total radioactivity in each sample) in solution. Hence, an increase in [11C]MET's relative activity in a collected sample is an indication of increased precursor

radiolabeling on the microchip. Therefore, the relative activity value was related to the L-homo radiolabeling efficiency for each run.

Equation 3-1 [^{11}C]MET relative activity equation:

$$[^{11}\text{C}]\text{MET Relative Activity (\%)} = \frac{[^{11}\text{C}]\text{MET RAD HPLC pk area} * 100\%}{\text{Total RAD HPLC pk areas}}$$

Initially, the temperature study was first carried out using EtOH and H_2O as reagent solvents (see Table 3-3) [13, 19]. HPLC product analysis for this procedure involved using a gradient mobile phase that starts with a 100% buffer composition. Then 10% buffer (90% MeCN) was used at 2 – 4 min in order to elute the [^{11}C]MeI for RCY calculations (see Figure 3-10) [18]. The data showed that a temperature increase from 42 ^{0}C to 82 ^{0}C, resulted in the increase of the relative activity by a factor of ~1.5 (48.6% to 74.8%). This was an indication that the radiolabeling process is affected by the change in temperature. Encouragingly, high product purity was observed (up to 86.6%) using the flow mix mode at a flow rate of 10 µL/min without generating any other C – 11 side products since the only detected activities were those of [^{11}C]MET and unreacted [^{11}C]MeI (see Table 3-3).

Table 3-3 [^{11}C]MET and unreacted [^{11}C]MeI relative activities detected for the synthesis of [^{11}C]MET using EtOH/H$_2$O on the abacus microchip in flow mix mode. A flow rate of 10 µL/min was used at various temperatures.

Temperature (^{0}C)	[^{11}C]MET relative activity (%)	[^{11}C]MeI relative activity (%)
42	48.6 *	51.4
62	58.3	41.7
82	74.8	25.2

A portion of these data are also represented on Figure 3-12.
*Calculation shown in Appendix B, Section 5.2.2.1.

Furthermore, hoping to improve the conversion of [^{11}C]MeI into [^{11}C]MET and to improve the purity of each sample the reaction solvent (EtOH) was replaced with extra dry acetone (see Figure 3-11). For confirmation, the product samples were also spiked using a solution of MET in acetone/H$_2$O (see Appendix A, Section 5.1.4.1, Figure 5-6, for [^{11}C]MeI spike chromatogram).
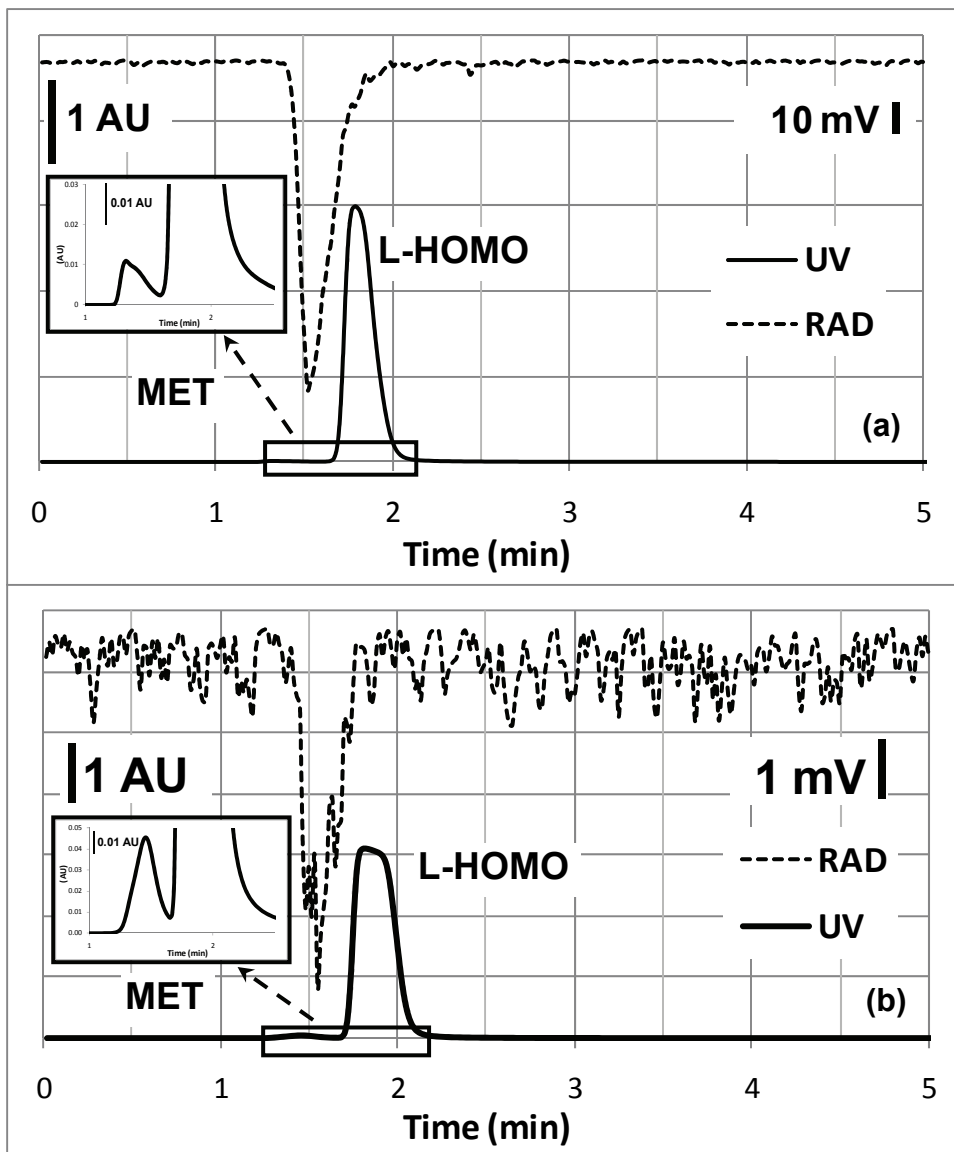
Note: MET was detected at ~1.4 min and L-homo was detected at ~1.8 min in the UV-HPLC. [^{11}C]MET was detected at ~1.6 min in the RAD-HPLC.

Figure 3-11 (a) UV-HPLC and RAD-HPLC for a product sample using the full loop microchip at 42 ^{0}C and a flow rate of 10 μL/min in acetone/H$_2$O and the (b) MET (76.9 mM) spiking experiment (16:1, MET:V2). The insets show a colloquial expansion of the MET cold mass peak.

The calculated relative activity in this case was between 93 – 100% demonstrating almost complete conversion of [^{11}C]MeI into [^{11}C]MET in each

collected sample (see Table 3-4). Since these values were already high at 42 ^{0}C

it was apparent that the temperature had no effect on the radiolabeling efficiency.

Also, these high relative activities were achieved in both microchip designs

without observing an obvious advantage of using the full loop design over the

abacus design. Furthermore, these findings implied that the use of acetone/H_2O

provides optimal conditions for the microchip radiolabeling process of L-homo

even at low temperatures.

Table 3-4 [^{11}C]MET relative activities detected for the synthesis of [^{11}C]MET using acetone/H_2O on the abacus and full loop microchip in flow mix mode. A flow rate of 10 µL/min was used at various temperatures.

Temperature (^{0}C)	[^{11}C]MET relative activity (%)	
	Abacus	**Full loop**
42	97.3 ± 0.5	100
62	96.8 ± 3.2	100

Note: Data represents the mean and range of two replicates.
 [^{11}C]MET is the only product observed through HPLC analysis in the repeated experiments.

3.4.2 [^{11}C]Rac Synthesis

After acquiring high relative activities with the microchip synthesis of

[^{11}C]MET, the [^{11}C]Rac radiolabeling process was also explored. [^{11}C]Rac was

synthesized with DMR and [^{11}C]MeI (see Scheme 1-5) using a similar microchip

procedure as [^{11}C]MET. Therefore, due to the lower [^{11}C]MeI concentrations

compared to the precursor (DMR) concentrations, this was also considered a

pseudo-first order reaction. Furthermore, the HPLC analysis was carried out

starting with the flow mix experiments (see Figure 3-12 for a sample chromatogram). On the lower trace of Figure 3-12, a Rac cold (C – 12) mass peak was not observed considering that the concentrations were below detectable levels in each product sample (see Appendix A, Section 5.1.4.2, Figure 5-7 for an inset of a UV-HPLC). Meanwhile, on the inverted RAD-HPLC the corresponding radiolabeled products, [^{11}C]Rac (2.0%) and unreacted [^{11}C]MeI (83.9%) were observed.
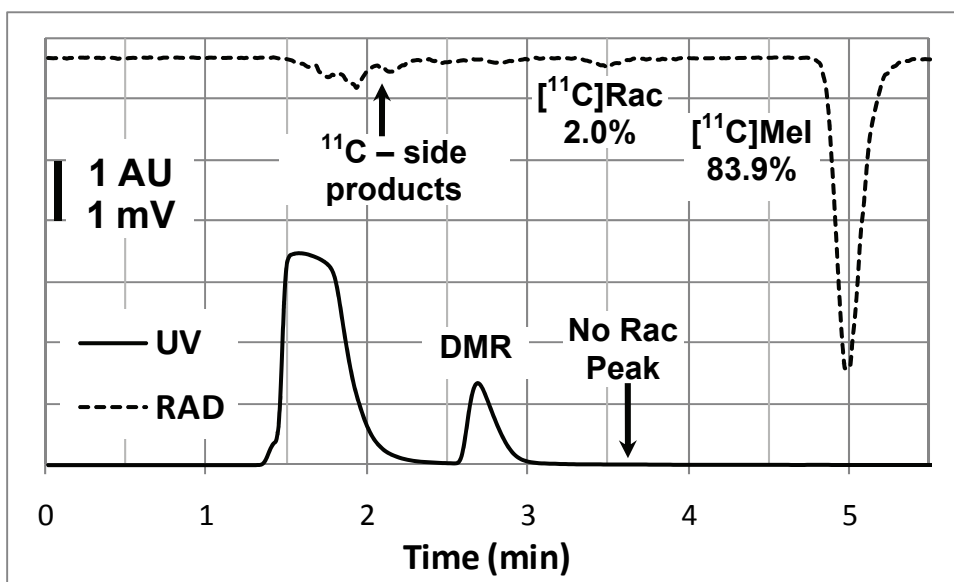
Note: The solvent, DMSO was detected at ~1.8 min and DMR was detected at ~2.7 min on the UV-HPLC while, [^{11}C]Rac and [^{11}C]MeI were detected at ~3.5 and ~5.0 min on the RAD-HPLC respectively.

Figure 3-12 (a) UV-HPLC and (b) RAD-HPLC for [^{11}C]Rac synthesis on the abacus microchip at 82 ^{0}C and a flow rate of 10 µL/min in flow mix mode.

Initially, [^{11}C]Rac relative activities were calculated using the RAD-HPLC peak areas using Equation 3-2. Where the numerator value was obtained from

[^{11}C]Rac's peak area and the denominator accounts for the peak areas of all the C – 11 compounds ([^{11}C]Rac, [^{11}C]MeI and side products) in solution.

Equation 3-2 [^{11}C]Rac relative activity equation:

$$[^{11}C]Rac\ Relative\ Activity\ (\%) = \frac{[^{11}C]Rac\ RAD\ HPLC\ pk\ area * 100\%}{Total\ RAD\ HPLC\ pk\ areas}$$

The results showed that temperature variation had no significant effect on [^{11}C]Rac's relative activity (see Figure 3-13). When the estimated temperature was increased from 62 ^{0}C to 122 ^{0}C, only a slight increase in the relative activity was observed displaying no change to the radiolabeling efficiency. This was believed to be a result of a trade-off between an increase in reaction rate and a loss of [^{11}C]MeI through evaporation with the increase in temperature.
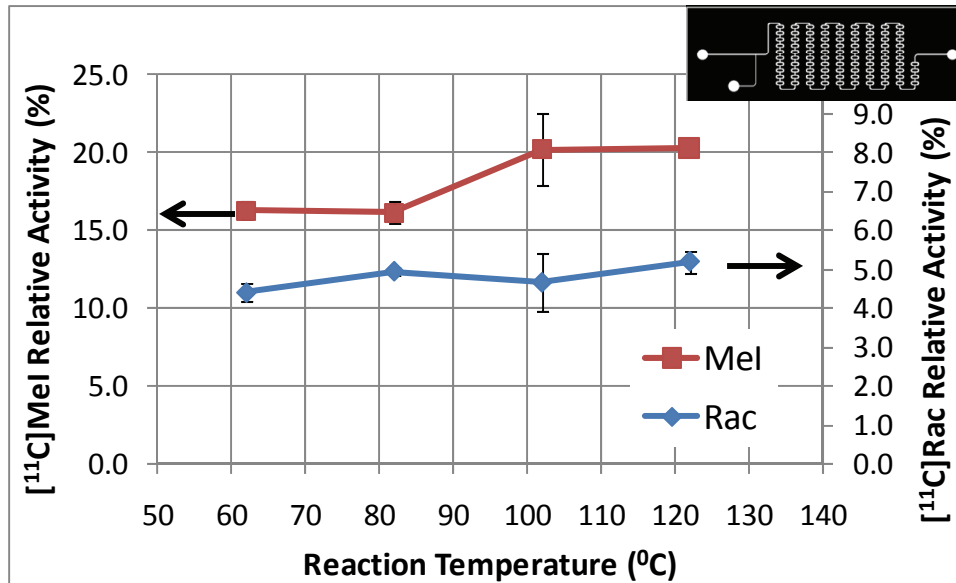
Note: Data represents the mean and range of two replicates.

Figure 3-13 Temperature variation effect on [^{11}C]Rac's relative activity in the full loop microchip at a flow rate of 10 µL/min with 4.0 – 5.5 min sample collections.

Furthermore, the effects of the reaction flow rate variation were studied [16]. In this study, the sample collection times were varied with the flow rates in order to keep the collection volumes (40 – 80 µL) consistent for each run (see Table 3-6). It became apparent that decreasing the rate of fluid delivery into the microchannels increased the [^{11}C]Rac production efficiency (see Table 3-5). For instance, a decrease in flow rate from 10 µL/min to 1 µL/min increased the relative activity by a factor of ~3 (2.0% to 6.7%). It was believed that the decrease in flow rate, increased residence time, which in turn increased the heat transfer and reagent diffusion and interaction time in the microchannels.

Table 3-5 [^{11}C]Rac synthesis results using the abacus microchip at 82 ^{0}C with sample collections at varied flow rates in flow mix mode.

Flow rate (µL/min)	[^{11}C]Rac relative activity (%)
10	2.0
5	4.0
2	5.1
1	6.7

A portion of these data are also represented on Figure 3-12.

However, considering that these relative activity values were generally low and lower than the [^{11}C]MET results, experiments were carried out to further optimize this process. First, the reaction mode was varied by premixing the reagents before introducing them into the microchannels. Premix mode involved mixing DMR and [^{11}C]MeI solutions and drawing the solutions into the syringes ~1 min before connecting the syringes were connected to the microchip. The

results for the premix mode procedure showed an increase in the [^{11}C]Rac relative activity in comparison to the flow mix procedure (see Table 3-6). For example, at a flow rate of 10 µL/min the relative activity increased by a factor of ~5 with the premixed mode compared to the flow mix mode.

Table 3-6 [^{11}C]Rac synthesis results using the abacus microchip where DMR and [^{11}C]MeI are reacted in a flow mix and premix mode, at 82 ^{0}C with sample collections at varied flow rates.

	Flow rate (µL/min)	Collection time (min)	[^{11}C]Rac relative activity (%)
Flow mix	**10**	2.0	2.0
	5	4.0	4.0
	2	10.3	5.1
Premix	**10**	3.0	10.0
	5	6.1	11.2
	2	14.2	16.0*

Note: Collection times were adjusted in each experiment with a different flow rate so that the total collection liquid volumes are roughly the same (i.e. ~20 µL in flow mix mode and ~30 µL in the premix mode).
*See Figure 5-7 for data UV-HPLC and RAD-HPLC.
A portion of these data are also represented on Figure 3-14.

However, the increase in [^{11}C]Rac relative activity between the 2 reaction modes was not sufficient, achieving only 16.0% relative activity at a flow rate of 2 µL/min. This effect was attributed to an increase in the C – 11 side products (see Figure 3-14). For instance, decreasing the flow rate from 10 µL/min to 2 µL/min increased the C – 11 side products' relative activity by ~29.0% (43.1% - 14.1%) in the flow mix mode. This suggested that the increase in residence time also favours side product formation. Even worse, premixing the reagents at 2 µL/min

increased the side products by an extra ~35.3% (78.4% - 43.1%). This pattern coincided with the decrease in the amount of unreacted [^{11}C]MeI found in the product samples, implying that the [^{11}C]MeI was used for the undesirable formation of side products through other methylation processes or possibly the decomposition of the radiolabeled products [79].
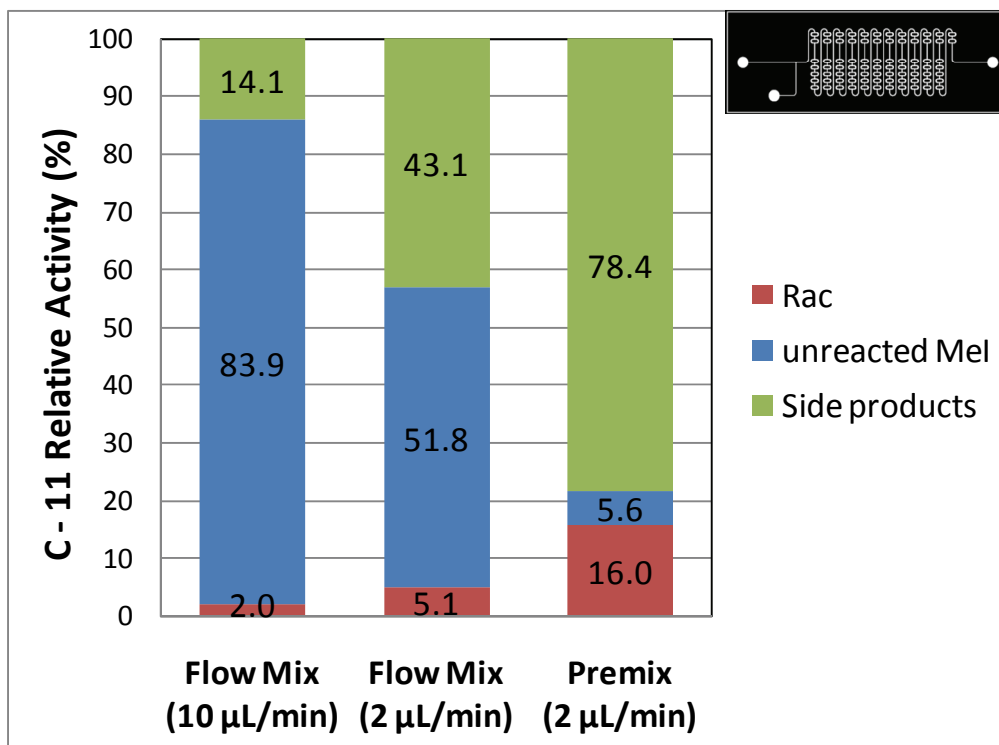
Note: Figure 3-12 shows the RAD-HPLC for the results (flow mix experiment at 10 µL/min) that were used to determine the C – 11 relative activities for [^{11}C]Rac, excess [^{11}C]MeI and side products. See Appendix A, Section 5.1.4.2, Table 5-5 for further details.

Figure 3-14 The [^{11}C]Rac, unreacted [^{11}C]MeI and C – 11 side products relative activities for experiments carried out on the abacus microchip in flow mix mode and premix mode at different flow rates and at 82 ^{0}C.

Additionally, the effect of the microchip design on the [^{11}C]Rac production was investigated (see Figure 3-15). Since full loop design (356 mm) has a

microchannel that is shorter than the abacus design (437 mm) it was expected to produce lower [^{11}C]Rac relative activity values due to a lower residence time (t is proportional to x^2 in the microchannels, see Equation 2-8). Surprisingly, this was not the case, the results displayed higher [^{11}C]Rac relative activities in each run with the full loop microchip design compared to the abacus microchip design. This was believed to be a result of a higher ratio of micromixer loops over a shorter channel for the full loop microchip, therefore more mixing of reagents in a shorter distance.
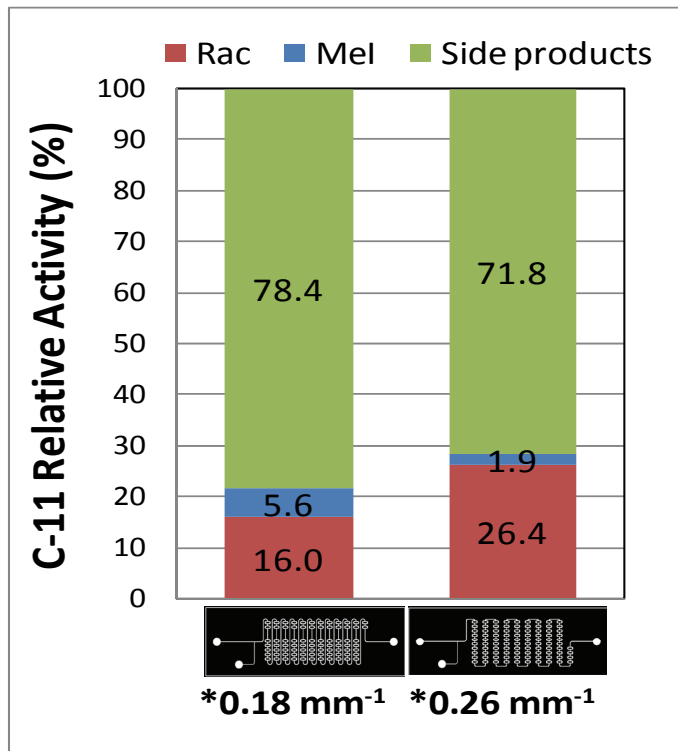
Note: *Shows the number of micromixers/channel length ratio in the microchip. Abacus = 79 loops/437 mm and full loop = 94 loops/356 mm.

Figure 3-15 Shows the [^{11}C]Rac, unreacted [^{11}C]MeI and C − 11 side products for experiments carried out on the abacus and full loop microchip designs at a flow rate of 2 µl/min in premix mode at 82 ^{0}C.

Moreover due to high levels of unreacted [^{11}C]MeI, the [^{11}C]Rac conversion was calculated using the [^{11}C]Rac's peak areas for further analysis of the collected data (see Equation 3-3). The [^{11}C]Rac conversion is the [^{11}C]Rac activity as a ratio of all the C − 11 compounds produced in each run. From the measured absolute activity of the product sample we calculated only the amount of [^{11}C]MeI that was utilized for the reaction while disregarding any activity losses (e.g. unreacted [^{11}C]MeI). Using the conversion value we were able to evaluate the extent of [^{11}C]MeI conversion into [^{11}C]Rac versus other undesired side products. This value along with the [^{11}C]Rac relative activity were considered to be an accurate evaluation of the methylation efficiency in the microchip.

Equation 3-3: [^{11}C]Rac conversion (%): accounts for the C − 11 side products produced during the methylation process.

$$[^{11}\text{C}]\text{Rac conversion (\%)} = \frac{[^{11}\text{C}]\text{Rac RAD HPLC pk area} * 100\%}{\text{Total RAD HPLC pk areas} - \text{unreacted } [^{11}\text{C}]\text{MeI RAD HPLC pk areas}}$$

From Table 3-7 it was observed that the [^{11}C]Rac conversion was greater than the relative activity values displayed (with the exception of the full loop microchip experiment at a flow rate of 2 µL/min). This was mainly due to the inadequate utilization of [^{11}C]MeI. Also, the premix mode showed a higher conversion of [^{11}C]MeI into [^{11}C]Rac in each run when compared to the flow mix mode (see Table 3-7). For instance, at a flow rate of 10 µL/min the conversion was ~1.6-fold higher (12.7% - 20.5%) in the premix mode than in the flow mix mode. Meanwhile, at reduced flow rates the conversion values slightly decreased in the premix mode. As a result of this behaviour it was implied that [^{11}C]Rac conversion might be more efficient at higher flow rates in the premix mode.

Additionally, at the same flow rate of 2 µL/min the [^{11}C]Rac conversion increased when using the full loop design by ~10% (16.9% – 25.5%) compared to the abacus design which was consistent with the observed increase in the relative activities. Also, the experiment on the full loop microchip at 2 µL/min showed repeatability with consecutive runs on the same microchip. However, the conversion values were still low at 2 µL/min due to the increase of undesirable side products.

Table 3-7 [^{11}C]Rac conversion at varied flow rates using the abacus and full loop microchip where reagents undergo flow mix and premix reaction modes, at 82 ^{0}C.

Microchip/Reaction mode	Flow rate (µL/min)	[^{11}C]Rac Relative activity (%)	[^{11}C]Rac conversion (%)
Abacus/ Flow mix	10	2.0	**12.7**
	5	4.0	**16.6**
	2	5.1	**10.5**
Abacus/ Premix	10	10.0	**20.5**
	5	11.2	**16.8**
	2	16.0	**16.9****
Full loop/ Premix	2	25.2	**25.2**
		25.2	**26.3**
		25.6	**25.6**
		26.4	**26.9**

**Calculation shown in Appendix B, Section 5.2.2.2.

Furthermore, we continued to evaluate the data by calculating the RCY (defined by Equation 3-4) using the estimated initial activity of [^{11}C]MeI. This

value was calculated at various flow rates for the different microchip designs in the premix mode. It was anticipated that decreasing the flow rate would decrease the RCY similar to the relative activity.

Equation 3-4 [^{11}C]Rac RCY equation: accounts for time variation and activity loss (unreacted and undetected in final product).

$$[^{11}\text{C}]\text{Rac RCY (\%)} = \frac{[^{11}\text{C}]\text{Rac activity}^{\neq} * 100\%}{\text{Initial } [^{11}\text{C}]\text{MeI activity}^{\neq} \text{ in each product sample}}$$

$^{\neq}$*All activities were decay-corrected, see Appendix B, Section 5.2.2.2 for definition.*

Moreover, from Table 3-8, it was observed that the use of the full loop microchip, where the ratio of micromixer loops to microchannel length is higher, lead to an increase in RCYs. For example, at a flow rate of 2 μL/min, using the full loop microchip we were able to achieve a RCY that is ~3-fold higher than that achieved by the abacus microchip. Meanwhile, results showed that the decrease in flow rate had no apparent effect on the RCY and that the minor change in values can correspond to experimental errors.

Table 3-8 [^{11}C]Rac RCY and absolute product activity at varied flow rates using the abacus and full loop microchip in the premix mode, at 82 ^{0}C.

Microchip	Flow rate (µL/min)	[^{11}C]Rac Relative activity (%)	[^{11}C]Rac conversion (%)	[^{11}C]Rac RCY (%)	*[^{11}C]Rac absolute activity (mCi)
Abacus	10	10.0	**20.5**	**3.3**	0.411
	5	11.2	**16.8**	**3.0**	0.386
	2	16.0	**16.9****	**2.8****	0.330**
Full loop	2	25.2	**25.2**	**11.2**	0.642
		25.2	**26.3**	**7.4**	0.362
		25.6	**25.6**	**7.2**	0.344
		26.4	**26.9**	**9.8**	0.414

Note: There was residual [^{11}C]MeI in the syringes, reaction vials and the microchip and that the calculated RCY may be an underestimation.
*Decay-corrected activity at the EOB.
**Calculation shown in Appendix B, Section 5.2.2.2.
* A portion of these data are also represented on Table 3-7.*
See Appendix A, Section 5.1.4.2, Table 5-4 for absolute activity values of [^{11}C]MeI and product sample.

However, even the best crude RCYs given by the full loop microchip were lower than those reported by conventional methods [24, 80]. Although the micromixer design performed well in the cold synthesis, we suspect that it is not efficient for this radiolabeling process. Also, the total radioactivity in the product samples for each run did not account for all the estimated (flow rate*time) initial [^{11}C]MeI activity. A possible explanation for these low values is activity loss through evaporation across the PDMS porous walls as [^{11}C]MeI has a b.p. of 42.4 ^{0}C, or even absorption of [^{11}C]MeI by the PDMS porous walls (see Appendix A, Section 5.1.4.2, Table 5-6) [8, 81]. Other losses are possible during fluid transfer from the vials to the syringes, from the syringes to the microchip (e.g.

dead volume in tubing), or unreacted residual volumes in the syringe or microchannels at the end of the experiment (see Appendix A, Section 5.1.4.2, Table 5-6).

3.5 Simulation of microchip synthesis

3.5.1 Simulation of an "ideal" plug-flow reactor (PFR) for Rac synthesis

The reaction engineering lab (REL) is a module that assumes that the reagents are reacting in a perfectly mixed environment where the reaction kinetics control the reaction progress. Two PFRs (see Figure 2-13 for definition) with different microchannel lengths were used to study the synthesis process. Initially, the default hot synthesis process parameters ([DMR] = 21.6 mmol/L (5.4 µmol/250 µL), [[^{11}C]MeI] = 0.024 mmol/L (6 nmol/250 µL) and k = 5.663×10^{-4} (L/(mmol·s)) at a flow rate of 15 µL/min) were explored on PFR 1, with a microchannel length of 31.0 mm. The results showed that as the reagents travel further down the microchannel there is more time (residence time) to generate Rac and hence gradually increasing the yield (see Figure 3-16). Then reaction conditions were varied in both PFRs for comparison. From the results the lowest final [^{11}C]Rac yield of ~0.8% observed was at a flow rate of 15 µL/min. This value was then used to normalize all the acquired data (see Experimental, Section 2.7.4 and Appendix B, Section 5.2.3.3 for sample calculation).
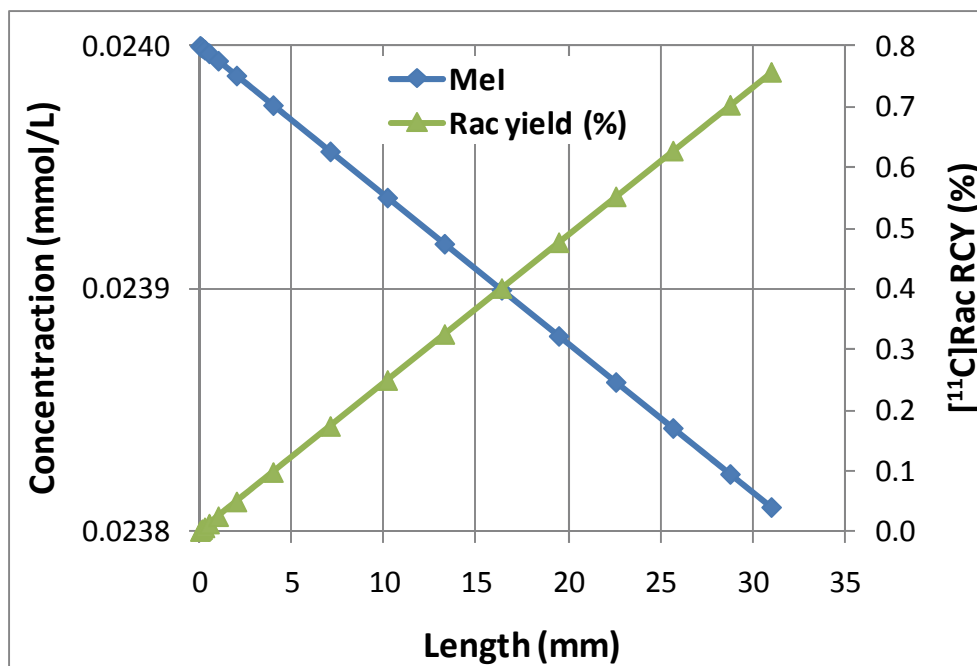
Note: Reaction conditions include using reagent concentrations of [DMR] = 21.6 mmol/L (5.4 µmol/250 µL) and [[^{11}C]MeI] = 0.024 mmol/L (6 nmol/250 µL) and k = 5.663×10^{-4} (L/(mmol·s)).

Figure 3-16 [^{11}C]Rac synthesis in PFR 1 (31.0 mm) as the reagents travel down the microchannel length at a flow rate of 15 µL/min.

As the volumetric flow rate of the reagents was varied, an effect on the yields was observed (see Figure 3-17). The normalized data showed an increase in Rac yield by a factor of ~7 when the flow rate was reduced from 15 µL/min to 2 µL/min.
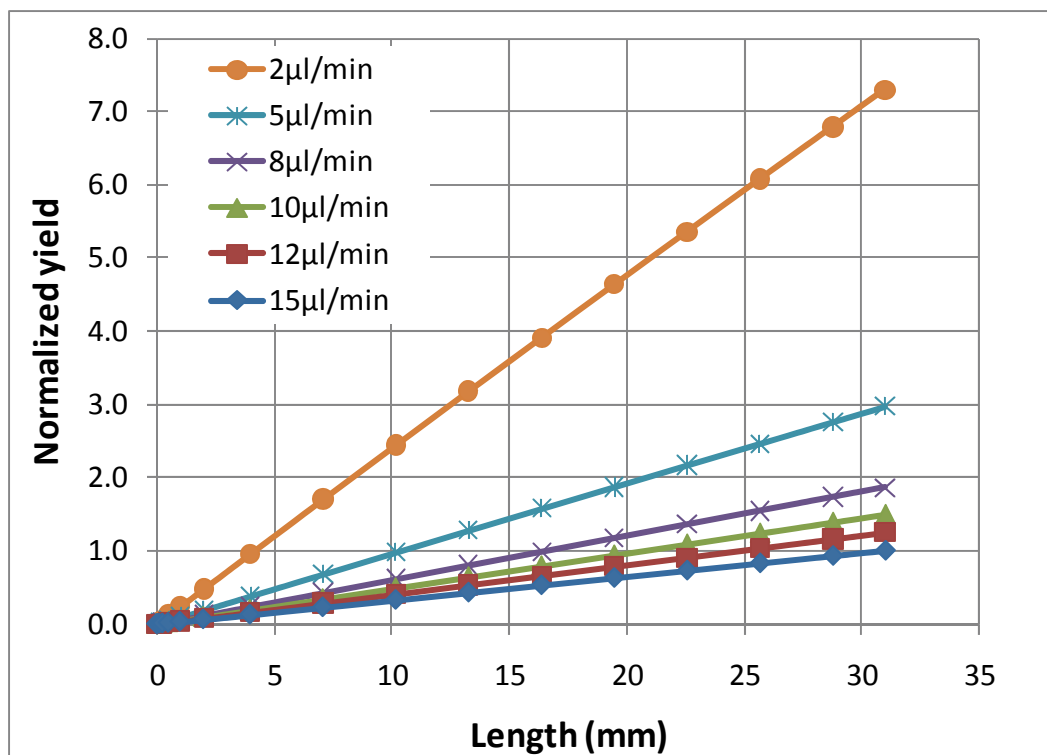
Note: Reaction conditions include using reagent concentrations of [DMR] = 21.6 mmol/L (5.4 µmol/250 µL) and [[^{11}C]MeI] = 0.024 mmol/L (6 nmol/250 µL) and k = 5.663×10^{-4} (L/(mmol·s)).

Figure 3-17 Effect of flow rate on [^{11}C]Rac synthesis in PFR 1 (31.0 mm) as the reagents travel down the microchannel length.

Similarly, the flow rate variation study was carried out on another plug-flow reactor, PFR 2 with a longer channel (L = 45.6 mm). When the values were normalized with respect to PFR 1, at a flow rate of 15 µL/min it became apparent that a reactor with a longer microchannel (PFR 2) had an effect of producing higher [^{11}C]Rac yields as a result of a longer residence time (see Figure 3-18 and Table 5-8 for data). For example, at a flow rate of 15 µL/min increasing the microchannel length from 31.0 mm (PFR 1) to 45.6 mm (PFR 2) showed an increase in the normalized [^{11}C]Rac yield by a factor of ~1.5, which was similar to

the increase in length ratio between the two microreactors. Furthermore, reducing the flow rate from 15 μL/min to 2 μL/min, PFR 1 showed an increase in the normalized [¹¹C]Rac RCY from 1.0% to 7.3%, while PFR 2 showed a higher increase from 1.5% to 10.6% showing a ~7-fold increase for both PFRs. This behaviour was similar to the flow rate variations in the experimental results (see Table 3-5).

Note: Reaction conditions include using reagent concentrations of [DMR] = 21.6 mmol/L (5.4 μmol/250 μL) and [[¹¹C]MeI] = 0.024 mmol/L (6 nmol/250 μL) and k = 5.663×10⁻⁴ (L/(mmol·s)).
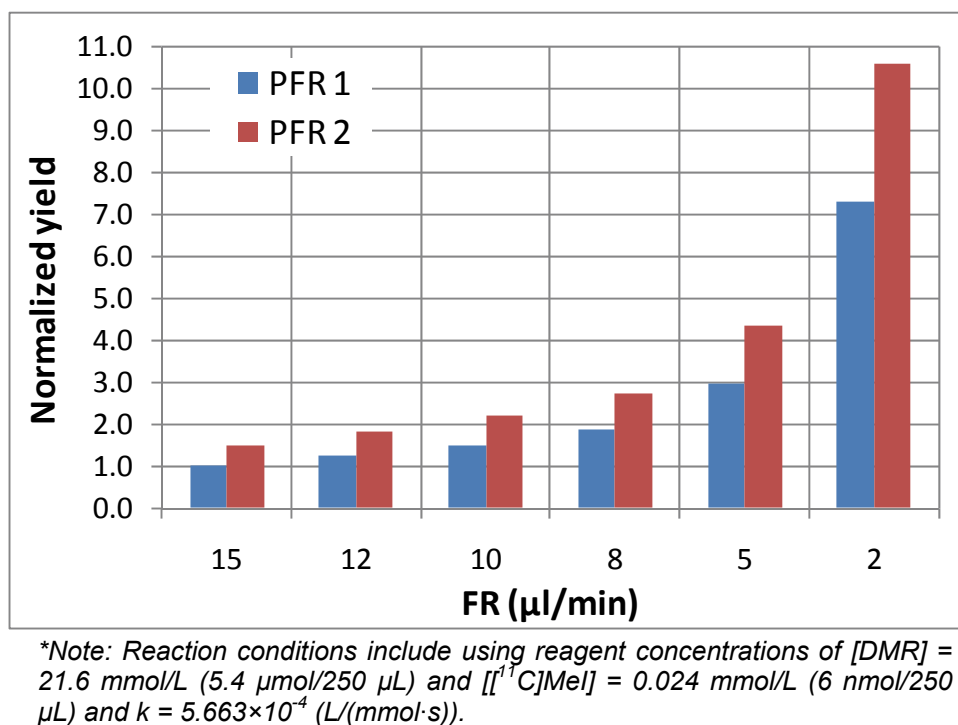
Figure 3-18 Normalized final [¹¹C]Rac yields in PFR 1 (31.0 mm) and PFR 2 (45.6 mm) in a flow rate variation experiment.

Finally, varying the MeI and DMR concentrations had a similar effect on the hot synthesis compared to the cold synthesis process. It was observed that [¹¹C]Rac RCYs were lower in PFR 2 than the Rac yields for the modelled cold

synthesis (using [DMR] = 21.6 mmol/L (5.4 µmol/250 µL) and [MeI] = 53.4 mmol/L (2.5 µL/750µL)) (see Figure 3-19). For example, at a flow rate of 2 µL/min the normalized Rac yield generated by the cold synthesis simulation (23.8%) was larger by ~2-folds than the hot synthesis value (10.6%). This indicated that the higher concentration of MeI in the cold synthesis (53.4 mmol/L) provides an advantage over the hot synthesis process with a lower [^{11}C]MeI concentration (0.024 mmol/L).
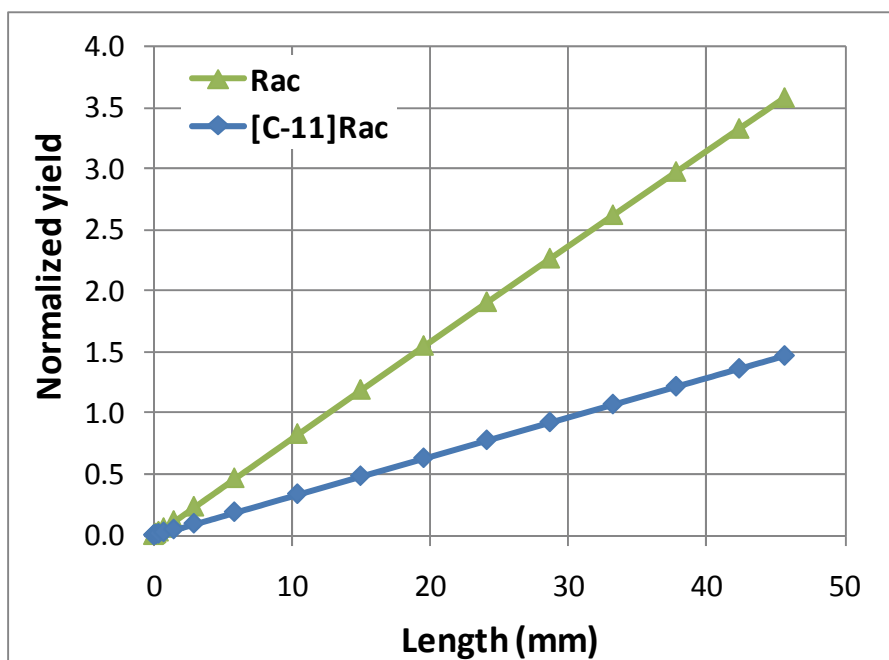
Note: Reaction conditions include using reagent concentrations of [DMR] = 21.6 mmol/L (5.4 µmol/250 µL), [MeI] = 53.4 mmol/L (2.5 µL/750 µL) and [[^{11}C]MeI] = 0.024 mmol/L (6 nmol/250 µL) with k = 5.663×10^{-4} (L/(mmol·s)). See Table 2-1 for the different reaction rate equations in the hot and cold synthesis simulation. See Appendix A, Section 5.1.5.1, Table 5-8 raw data.

Figure 3-19 Normalized [^{11}C]Rac RCYs and Rac yields in PFR 2 (45.6 mm) as the reagents travel down the microchannel length at a flow rate of 15 µL/min.

Therefore, the calculated yields for the ideal PFR microreactor with the given volumes show optimum conditions with a longer microchannel (45.6 mm), a slow flow rate (2 μL/min) and higher concentrations. However, considering this model does not incorporate the microreactor's geometry or reagent diffusion coefficients, it is unable to account for the laminar flow, the micromixer designs and the reagent species physical properties [68]. In addition, the REL model assumes that the reactions are carried out in a perfectly mixed environment and that the microchannel provides reaction time without taking into consideration the required "reagent mixing" time. Hence, it was expected that the calculated yields are overestimated values.

3.5.2 Mixing and chemical reaction simulation

Prior to implementing a chemical synthesis model the flow and micromixing simulations were carried out. The MEMS module creates a "space-dependent" model where the microchip dimensions are considered for the simulation.

3.5.2.1 Microchannel flow simulation

The Navier-Stokes equation for the MEMS module was used to simulate the flow properties within the microchannels (see Figure 3-20). For the abacus microchip RU the flow field displayed laminar flow properties with R_e values that were significantly low (< 2300) (see Table 5-12 for R_e at different flow rates). In Figure 3-20, the magnitude of velocity is displayed through the size of the arrow in the given plot. Therefore, due to laminar flow a parabolic velocity field was

present within the microchannels where the maximum velocity is experienced in the centre of the channel expressed with a dark red color and zero-velocity is experienced at the channel walls expressed with a dark blue color. This velocity behavior was observed throughout the microchannels and micromixer loops design.

Furthermore, it was observed that the side inlet-channel experiences a higher velocity than the main inlet-channel (see Figure 3-20(a)). In the 2D model, the same volumetric flow rate was applied to both inlets, and considering that the side (0.05 mm) inlet-channel is smaller in width than the main (0.10 mm) inlet-channel the fluid flowing through it experiences double the velocity. For example, in the case of 2 µL/min flow rate, the main and side inlet-channels' maximum velocities were around 3.3 mm/s and 6.6 mm/s respectively.
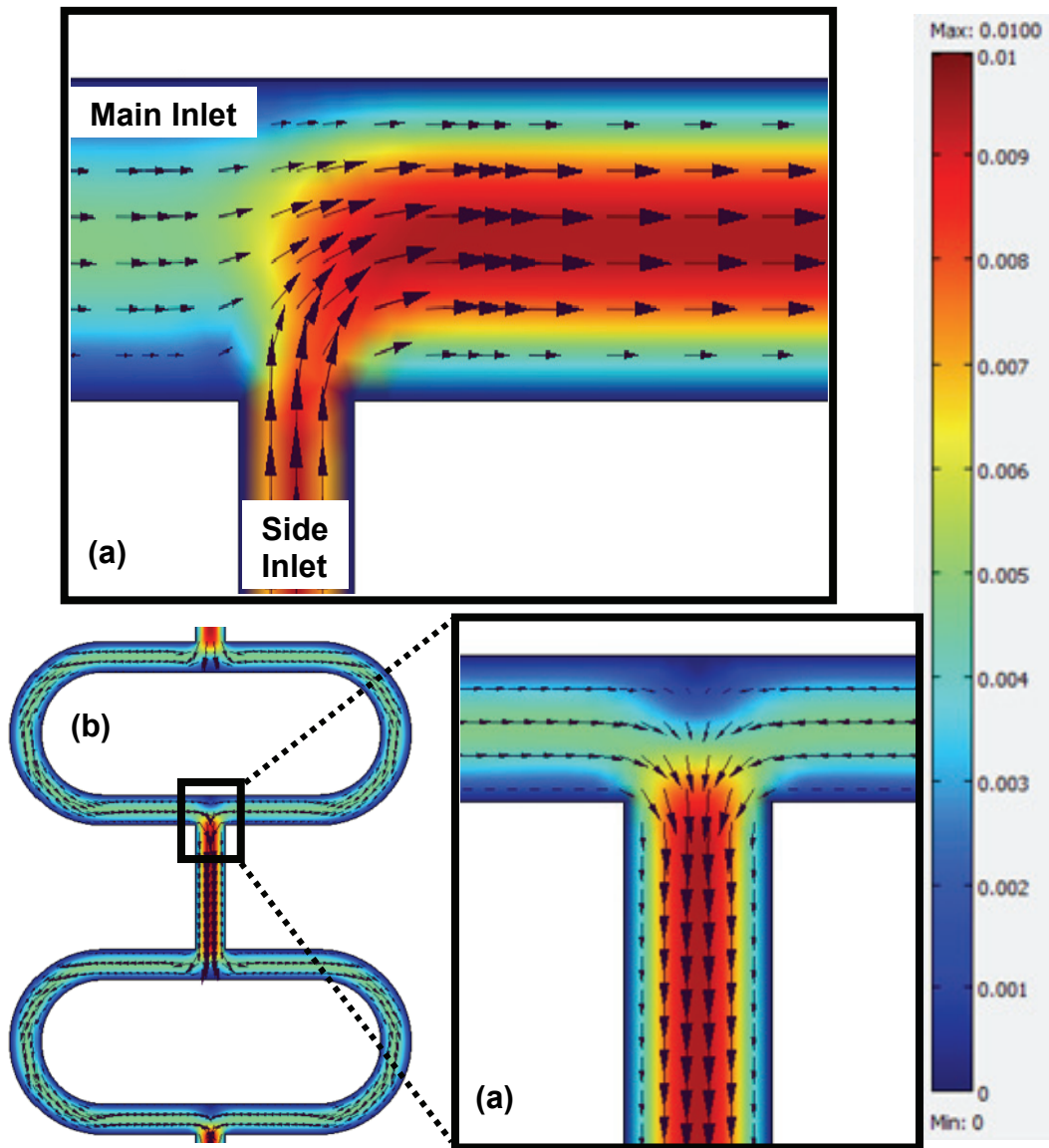
Figure 3-20 Surface and arrow plot diagrams showing the velocity field properties in the microchip for the (a) Inlet T-junction and (b) 5th – 6th loop. (c) Inset of the junction at the 5th loop outflow for the abacus design RU was modeled (see Figure 2-14 for diagram) at 2 µL/min.

In the microchannel where the flow splits, the velocity force is also splits

equally. Once the two channels recombine, the maximum velocity is experienced

in the larger channel (see Figure 3-20(b)). Also, at the recombination junction the fluids experience a zero-velocity due to the collision of the two streams, before continuing at the maximum velocity.

3.5.2.2 Micromixing simulation

The mixing within the microchannels was investigated using the diffusion coefficient of an organic molecule such as fluorescein (D = 5 ×10^{-10} m^2/s) in water. The concentration values used were 1 mmol/L at the main inlet and 0 mmol/L at the side inlet. Therefore, for complete mixing of the two fluid streams, the outlet concentration should be 0.5 mmol/L. In this case, the average outlet concentration was simulated to be 0.51 mmol/L at a flow rate of 12, 6 and 2 µL/min (see Appendix A, Section 5.1.5.2, Table 5-9). This was consistent with our experimental mixing results that displayed an even color distribution of green food-dye when the blue and yellow fluid streams were combined. However, on the molecular level when the concentration distribution plots were examined it was clear that the concentration obtained at the outlet of the RU is only an "average" of a high concentration on one-side of the channel and a low concentration on the other side (see Figure 3-21). It was apparent that instead of generating multiple sub-streams from the main fluid stream, the micromixer was splitting the reagents on both sides of the microchannel. This was also an indication that mixing is mainly occurring through diffusion in the microchannels. For example, although the final concentration is similar at the different flow rates, examining the concentration distribution plots for the abacus design RU at the

different flow rates showed a variation in the diffusion level within the microchannels, shown at the last micromixer loop (see Figure 3-21).
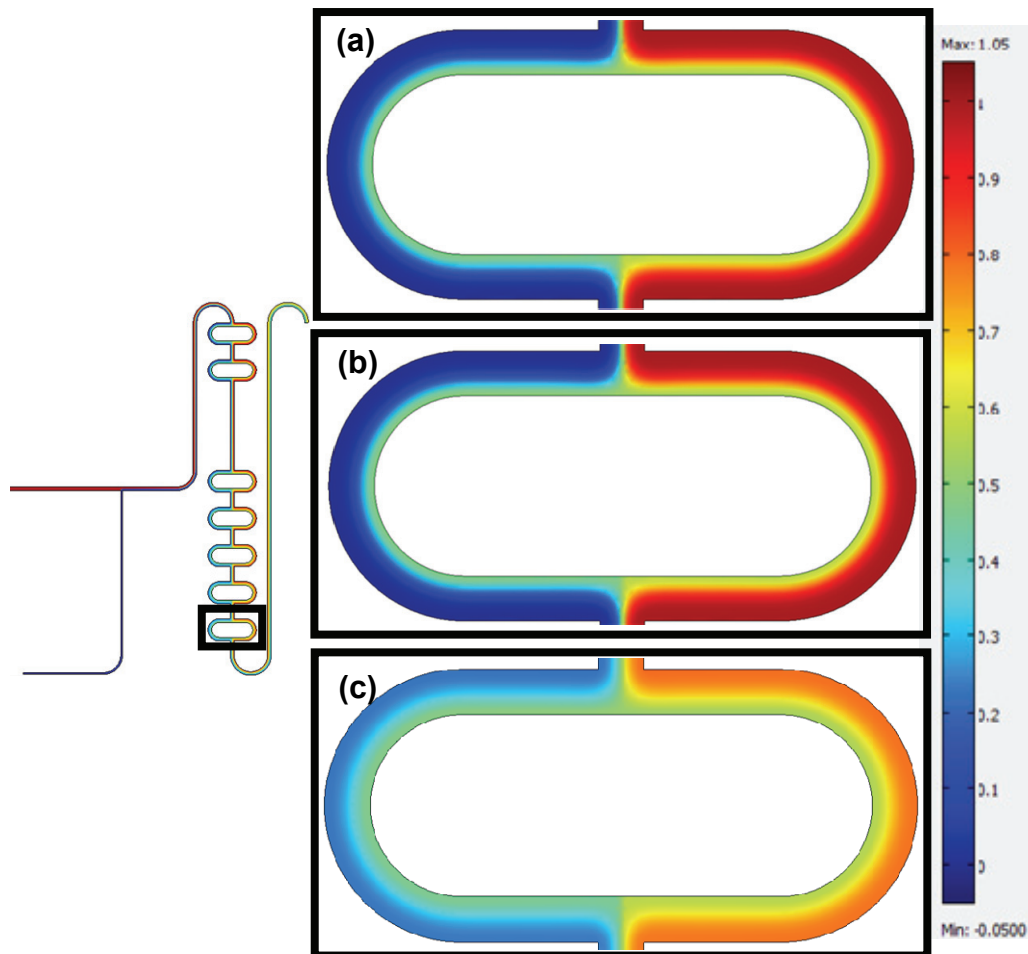
Note: The scale represents the concentration distribution (mmol/L)

Figure 3-21 Concentration (mmol/L) surface plot diagrams in the last loop at a flow rate of (a) 12 µL/min, (b) 6 µL/min and (c) 2 µL/min for the abacus design RU's mixing simulation.

3.5.2.3 Chemical reaction module

In this section the reaction kinetics were combined with the microchannel design in order to create a space-dependent model of the three microchip

designs' RUs. It was assumed that the carrier solvent is water with the reagent species diffusion properties represented by an estimated diffusion coefficient for the reaction solvents mixture (DMSO and MeCN) since they are the dominant species in the solution [72, 75]. Using this generated model we were able to vary the flow rate, reagent species concentrations, microchip design and reaction mode parameters. The product concentration calculated at the RUs' outlet was used to evaluate the reaction efficiency. Comparison of the achieved yields was a good indication of how the reaction parameters had an effect on product formation as the reagents flow through the microchannel. For these simulations, the rate constant and diffusion coefficient values were also varied in order to cover the estimated reaction condition ranges [70, 74, 76]. It is important to note that the rate constant values used were obtained from a similar methylation of a less substituted phenoxide site (3-nitrophenol). Since it is more acidic than our precursor DMR, the calculated values are expected to reflect a faster rate of reaction than is actually expected of our radiolabeling process [70].

The normalized yields (with respect to the no loop RU investigation at default parameters) generated with the hot synthesis investigation on the three microchip RUs agreed with the REL's, PFR 1 and PFR 2 result patterns (see Figure 3-22). The no loop design RU, having the shortest microchannel of 31.0 mm, which corresponded to the channel length of PFR 1, produced the lowest yields. Meanwhile, the abacus design RU having the longest microchannel of 45.6 mm, which corresponded to the channel length of PFR 2, produced the

highest yields. This correlation was also consistent when the [^{11}C]Rac yields increased with the reduced flow rates.
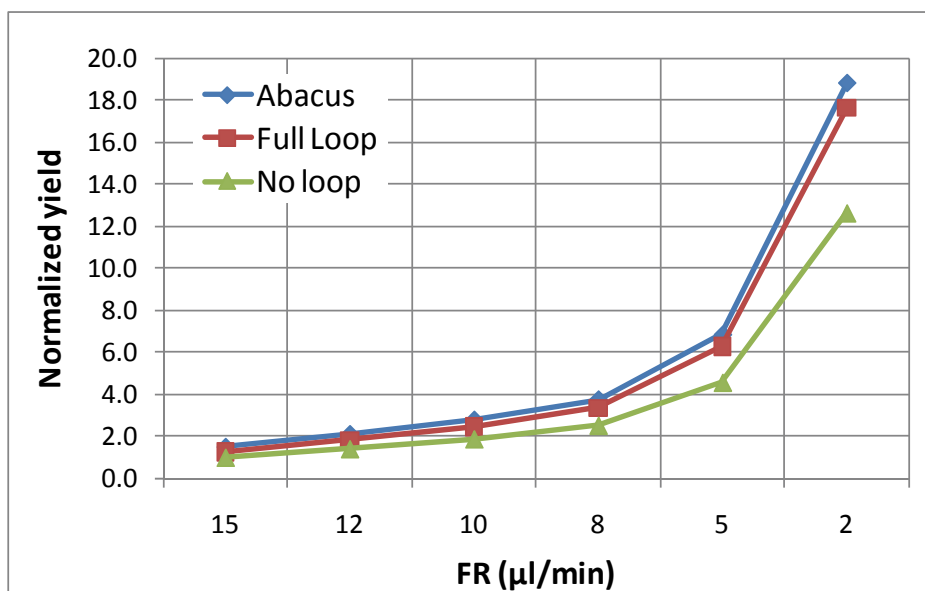
Note: Reaction conditions include using D = 10^{-9} m^2/s, k =5.663×10^{-4} (L/(mmol·s)) with reagent concentrations of [DMR] = 21.6 mmol/L and [^{11}C]MeI = 0.024 mmol/L in flow mix mode.
***See Appendix 5.1.5.3, Table 5-10 for data.*

Figure 3-22 Flow rate effect on the normalized [^{11}C]Rac yields modelled in the no loop (31.0 mm), abacus (45.6 mm) and full loop (42.8 mm) designs' RU.

Although the average [^{11}C]Rac concentration was higher for the abacus RU, the surface plot diagrams have shown a higher [^{11}C]Rac concentration distribution in the micromixer loops of the full loop RU (see Figure 3-23(e)) and (f)). From these diagrams it was apparent that with a "dark red color" more [^{11}C]Rac was generated at the centre of last micromixer loop in the 1st meander with the full loop design compared to the abacus design (see Figure 3-23(g)). This effect was attributed to the increase in fluid stream collisions, which resulted

in an increase of product generation. Therefore, explaining the higher concentration distribution in the full loop design (10 loops) compared to the abacus design (7 loops), due to a higher number of micromixer loops.
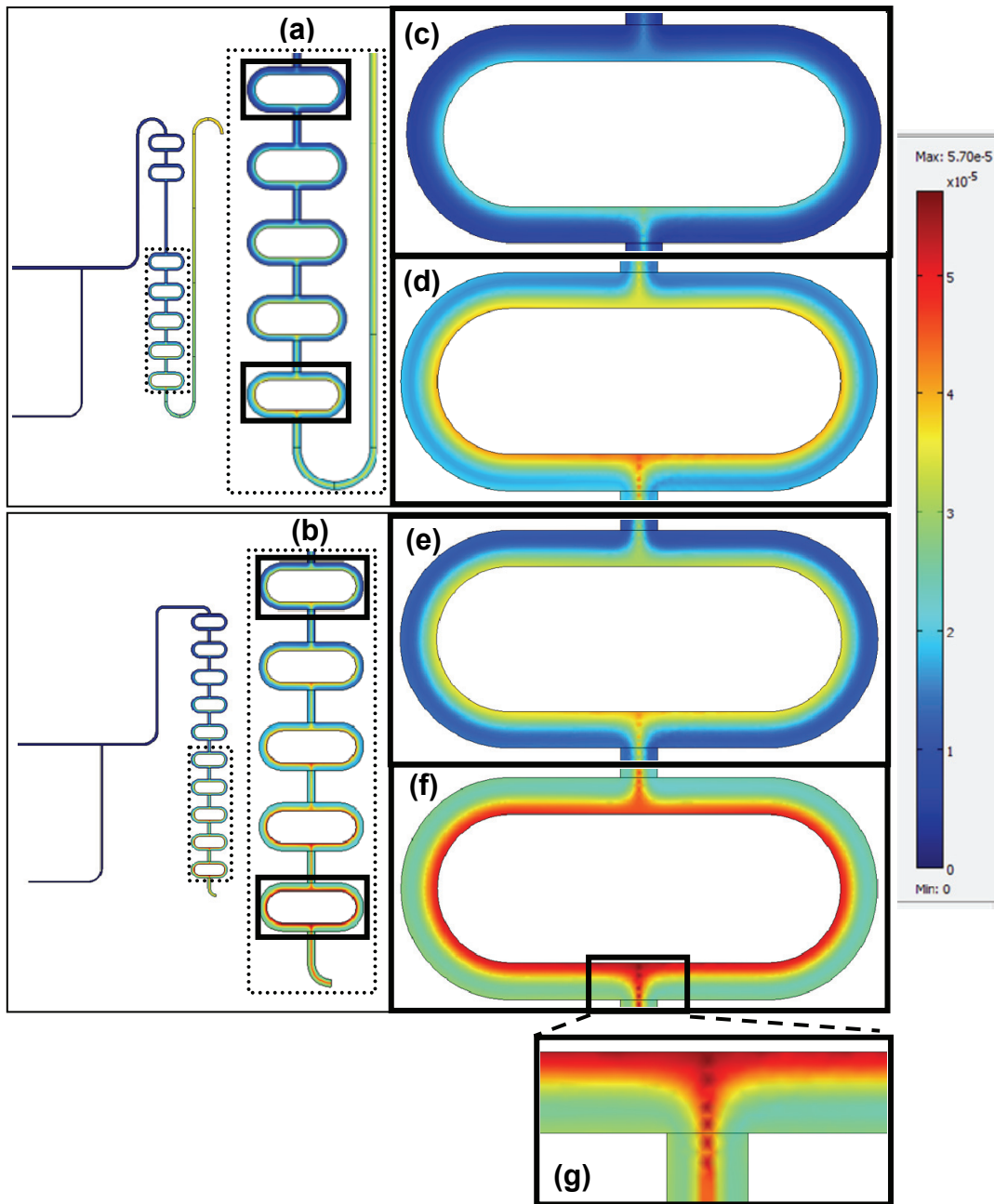
Note: Reaction conditions include using a flow rate of 15 µL/min, D = 10^{-9} m^2/s, k = 5.663×10^{-4}(L/(mmol·s)), [DMR] of 21.6 mmol/L, [^{11}C]MeI of 0.024 mmol/L in flow mix mode. The scale shown represents the concentration distribution of [^{11}C]Rac (mmol/L).

Figure 3-23 [^{11}C]Rac concentration (mmol/L) surface plot diagrams for the last 5 micromixer loops in the (a) abacus and (b) full loop design RUs for the hot synthesis. The Insets show the (c) 3rd and (d) 7th loop of the abacus design and the (e) 5th and (f) 10th loop of the full loop design. (g) Shows an inset of the 10th loop recombination junction (collision area = "hot spot").

Moreover, the increase in [11C]Rac concentration after each micromixer loop in the full loop design was larger than in the no loop (serpentine) design RU (see Figure 3-24). This was an indication of the micromixer loop structure generating some passive mixing. In addition, the premix mode showed a significant improvement in product generation in the microchannels in comparison to the flow mix mode. For example, at a flow rate of 15 μL/min and, a ~4–fold (1.3 to 5.9) increase in the normalized [11C]Rac yield was observed when the reagents were modelled in the premix mode compared to the flow mix mode using the full loop RU.
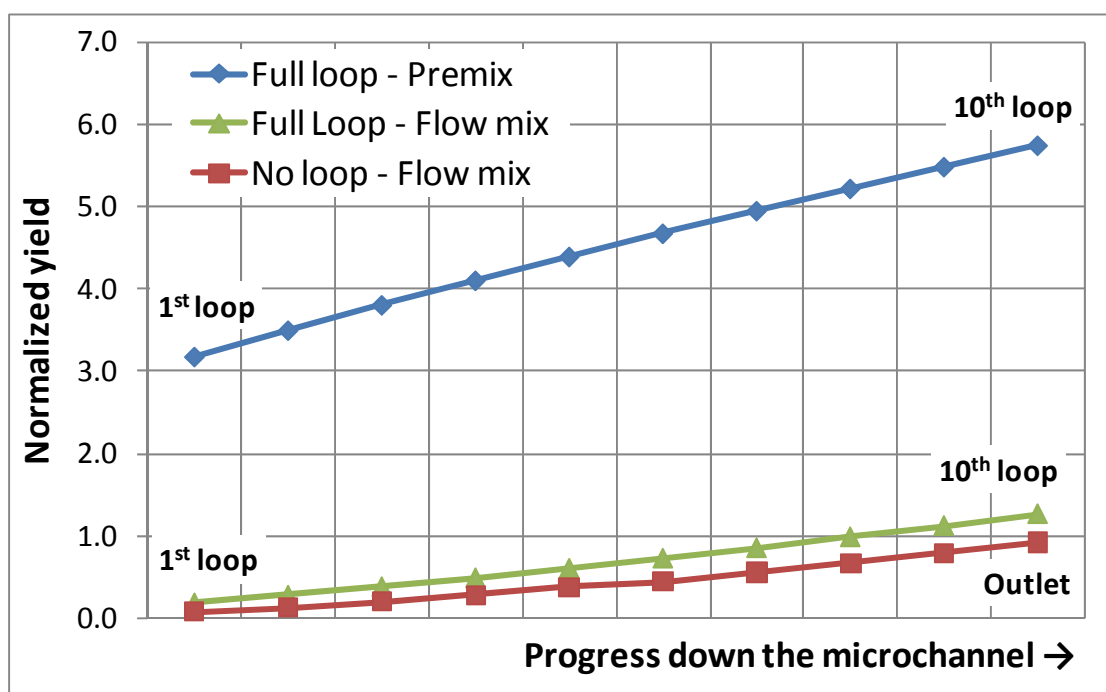
*Note: Reaction conditions include a flow rate of 15 μL/min, using $D = 10^{-9}$ m^2/s, k $=5.663 \times 10^{-4}$ (L/(mmol·s)) with reagent concentrations of [DMR] = 21.6 mmol/L and [11C]MeI = 0.024 mmol/L in flow mix mode.

Figure 3-24 [11C]Rac product generation down the microchannel of the full loop (flow mix and premix mode) and no loop design for the hot synthesis.

Furthermore, the flow mix and premix modes were modelled at various flow rates (see Figure 3-25). Examining the surface plot diagrams showed an increase in [^{11}C]Rac concentration when switching from flow mix to premix mode which was an indication of a higher reaction efficiency. Also, reducing the flow rate from 5 μL/min to 2 μL/min displayed an increase in microchannel [^{11}C]Rac concentrations for both reaction modes.
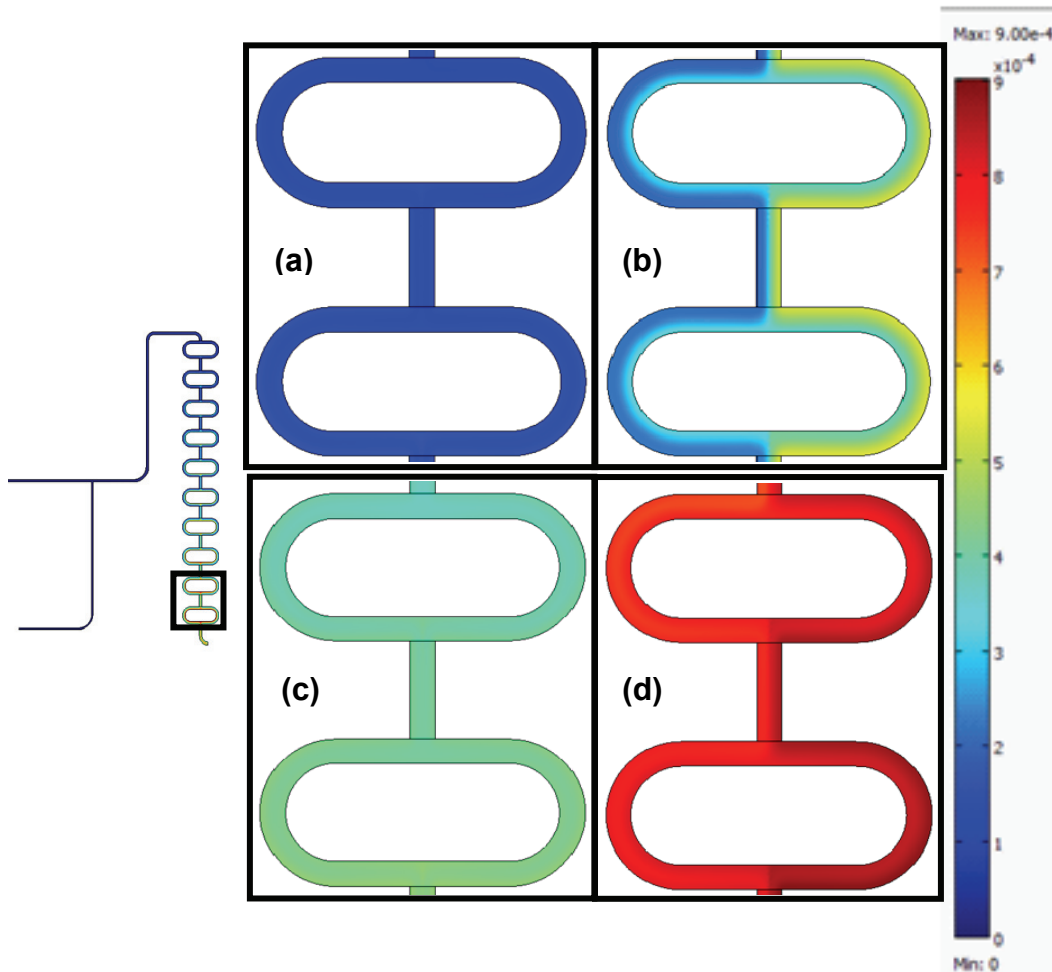
Note: Reaction conditions include using $D = 10^{-9}$ m^2/s, $k = 5.663 \times 10^{-4}$ $(L/(mmol \cdot s))$ with reagent concentrations of $[DMR] = 21.6$ mmol/L and $[^{11}C]MeI = 0.024$ mmol/L. The scale shown represents the concentration distribution of $[^{11}C]Rac$.

Figure 3-25 $[^{11}C]Rac$ concentration (mmol/L) surface plot diagrams for the 9th and 10th micromixer loops in the full loop design RU for the hot synthesis. (a) A flow rate of 5 µL/min was used in flow mix mode, (b) a flow rate of 5 µL/min was used in premix mode, (c) a flow rate of 2 µL/min was used in flow mix mode and (d) a flow rate of 2 µL/min was used in premix mode.

In addition, other parameters such as the diffusion coefficients, reagent concentrations and reaction rate constant were varied (see Table 3-9). In this case the diffusion coefficient (D) values covered a range for the change in the

solvent's physical behaviour when temperature is increased from 25 ^{0}C to 125 ^{0}C [76]. This wide range was covered in order to explore the effect of the change in diffusivity on the reaction progress. Additionally, the model generated yields that were normalized with respect to the no loop [^{11}C]Rac synthesis simulation using the default parameters.

As expected, the results showed that an increase in the value of diffusivity (D from 10^{-9} to 10^{-8}) will slightly increase the normalized yield by a factor of ~1.1 (from 17.6% to 18.7%). Also, premixing the reagents at low concentrations does not produce the same yields. On the other hand increasing the concentrations of the reagents to reflect the cold synthesis experimental values ([MeI] = 53.4 mmol/L and [DMR] = 21.6 mmol/L) displayed a ~2-fold (17.6% to 41.6%) increase in the normalized Rac yield. Furthermore, a drop in the rate constant showed a large effect on the normalized Rac yield as expected (1/100*k reaction rate constant gives 1/100*RCY).

Table 3-9 The effect of reagent concentration, diffusion coefficient and rate constant variation on the normalized Rac yield on the full loop RU using a flow rate of 2 µL/min in flow mix mode.

Variation	Reaction condition	Normalized Rac yield
	*Default concentrations, $D = 10^{-9}$ m^2/s, $k = 5.663 \times 10^{-4}$ L/(mmol·s), Flow mix	17.6
D (m^2/s)	*Default concentrations, **$D = 10^{-8}$ m^2/s**, $k = 5.663 \times 10^{-4}$ L/(mmol·s), Flow mix	18.7
k (L/(mmol·s))	*Default concentrations, $D = 10^{-9}$ m^2/s, **$k = 5.663 \times 10^{-6}$ L/(mmol·s)**, Flow mix	1.80×10^{-1}
	*Default concentrations, $D = 10^{-9}$ m^2/s, **$k = 5.663 \times 10^{-8}$ L/(mmol·s)**, Flow mix	1.80×10^{-3}
Reagent amount (mmol/L)	****High concentrations**, $D = 10^{-9}$ m^2/s, $k = 5.663 \times 10^{-4}$ L/(mmol·s), Flow mix	41.6
	High concentrations, $D = 10^{-9}$ m^2/s, $k = 5.663 \times 10^{-4}$ L/(mmol·s), **Premix	75.1

Note: The final yields produced by the no loop design RU simulation with default reaction conditions at a flow rate of 15 µL/min is set to 1 and is used to normalize all the raw data. A portion of these data are also represented on Table 5-11.

*Default: Reaction conditions include using [[^{11}C]MeI] = 2.4×10^{-2} mmol/L and [DMR] = 21.6 mmol/L which are related to the hot synthesis concentrations. See Table 2-1 for species rate of reaction equations.

**High concentration: Reaction conditions include using [MeI] = 53.4 mmol/L and [DMR] = 21.6 mmol/L which are related to the cold synthesis concentrations. See Table 2-1 for species rate of reaction equations.

4: CONCLUSION AND FUTURE WORK

4.1 Conclusions

The microchip radiolabeling results displayed a unique behaviour for each reaction (i.e. [^{11}C]MET and [^{11}C]Rac) mechanism. The [^{11}C]MET synthesis produced high relative activities at temperatures as low as 42 ^{0}C and a flow rate of 10 μL/min in flow mix mode (see Table 3-3 and Table 3-4). Additionally, the [^{11}C]MET synthesis was affected by solvent variation achieving relative activities as high as 97.3 – 100%, by changing the reaction solvent from EtOH/H_2O to acetone/H_2O demonstrating an efficient [^{11}C]MeI conversion process. Also, the isocratic HPLC method used for the product analysis eluted the [^{11}C]MeI and [^{11}C]MET peaks within 3 min and only required short wait times between runs which was considered an advantage when working with small amounts of short-lived activity and multiple product collections.

On the other hand, the microchip synthesis of [^{11}C]Rac produced lower relative activities in the flow mix mode (see Table 3-5). These values were increased with the increase in residence time through reduced flow rates and premixed reagents. Meanwhile, temperature changes displayed no effect on the [^{11}C]Rac relative activity for each run which was attributed to a trade-off effect due to activity loss at higher temperatures. Additionally, we were able to increase the [^{11}C]Rac relative activity, with the increase in the number of loops to channel length ratio when using the full loop microchip design which can be attributed to

improved mixing and reagent interaction. Also, using the premix mode showed a more significant effect on the radiolabeling efficiency by increasing the [^{11}C]Rac relative activity by a factor of 3 compared to the micromixers' effect which only improved this value by a factor of ~1.5. On the other hand, the increase in residence time was a disadvantage to the acquired [^{11}C]MeI conversion and [^{11}C]Rac RCYs. This was because an increase in residence time and reagent interaction time meant an increase in the possibility of other radiolabeling reactions and side product generation.

Furthermore, completing the computational fluid dynamics investigation has provided a better understanding of the flow, mass transport and kinetic behaviour of the cold and hot synthesis processes in the microchip. Incorporating the "ideal" plug-flow reactor (PFR) kinetics with a "space-dependent" model was used to compare the efficiency of each of the three given microreactor designs. Initially, it became apparent that the REL module generated yields for the "ideal" PFR investigation that were higher than those obtained by the space-dependent model. For example, modelling the PFR 2 microreactor using the hot synthesis concentrations generated a Rac yield that was higher than the value produced by the abacus microchip RU modelled at a flow rate of 2 μL/min in premix mode (using the MEMS module) by a factor of 4 (see Appendix A, Section 5.1.5, Table 5-8 and Table 5-10). Therefore, indicating that although the micromixer designs generate some passive mixing, they are still not sufficient for this process.

Moreover, the "space-dependent" model demonstrated that the fully mixed streams observed during the visual mixing experiments do not always provide

accurate information about the flow and transport of species at the molecular level (see Figure 3-6 and Figure 3-21). Hence, if fully mixed solutions are visualized at the outlet, it is not necessarily an indication that liquid streams have been efficiently mixed at the molecular level. When this model was applied to the synthesis process, the abacus design's repeating-unit (RU) produced higher yields compared to the full loop design's RU. Despite this, it was observed that the mixing within the microchannels in certain areas was better in the full loop design, due a higher ratio of micromixer loops (see Figure 3-23 and Figure 3-24). This finding coincided with our cold and hot synthesis experimental results, which show higher yields with the full loop microchip at a higher micromixer loop to channel length ratio (see Table 3-7).

Also, the significantly lower hot synthesis [^{11}C]MeI concentration resulted in lower yields in our modeling results similar to experimental results (see Figure 3-19 and Table 3-9). On the other hand, reducing the flow rate and premixing the reagents increased the yields in both investigations. These results confirmed that even under microchip synthesis conditions; working with smaller concentrations for a pseudo-first order reaction, the residence time and reagent contact are important variables that affect the reaction yields.

Therefore, it can be deduced that even on a microscale the methylation process is dependent on the inherent reaction kinetics of the given mechanism. This can be related to the fact that during the liquid-liquid radiolabeling process, the much lower [^{11}C]MeI amounts and pseudo-first order kinetics has more control over the rate of the reaction than other parameters (such as channel

115

length). Hence, confirming the difference in the results shown by the [^{11}C]Rac hot synthesis process compared to the cold synthesis process. Also, implementing a more efficient micromixer design that is capable of reducing diffusion distances and increasing reagent species interaction, is very important in the case of a less efficient radiolabeling process such as the [^{11}C]Rac synthesis than in an inherently fast radiolabeling process, such as the [^{11}C]MET synthesis. Finally, considering that the acquired [^{11}C]Rac crude yields (unpurified) are still lower than the conventional methods' reported yields ([^{11}C]Rac = 50 – 65%), it was clear that this microchip technique is not ideal for the [^{11}C]Rac radiolabeling process. It was suspected that the reduced precursor masses, micromixer design, microchip porous material, channel length, residence time and sample transfer are all factors that play a role in negatively affecting the radiolabeling process efficiency and hence reducing the yields.

4.2 Future work

4.2.1 Fabrication and system design

It is important to note that the experimentation process confirmed that the polymer (PDMS) material might not be ideal for the radiolabeling processes [8]. Its use for prototyping could create issues through solvent incompatibility, particle absorption or evaporation through its porous walls. All these possibilities can cause reagent loss and hence depreciate the product yields. Therefore, working with glass even for prototyping experiments might be beneficial for this process.

Furthermore, estimating temperature values was a challenge considering that we were unable to find out the exact temperatures within the microchannels. Also, with the microchip PDMS surface temperatures there was a possibility that the glass-bottom of the microchip was at a higher temperature. Therefore, for future purposes a new heating device should be considered. Since the stainless steel-Al microchip holder in this case is compatible with high temperature operations the possibility of using an enclosed heating device would be beneficial to the synthesis process. This can provide a more accurate reflection of reaction temperatures. Other possibilities include redesigning the microchip holder with a larger well and an electronic-connection feature in order to fit customized (e.g. Peltier) heaters which can be calibrated and would provide heating through contact with the microchip surface.

Another, important feature that should be addressed in the future is the monitoring of radioactivity during the radiolabeling process. Considering that the detection areas are very small with a microdevice, this might be a challenge. However, it is important to monitor the initial [^{11}C]MeI activity that is entering the microchannels for a better yield estimation. For example, if the microchip holder was enclosed in a localized shielding system then placing a small radiation detector next to the [^{11}C]MeI tubing could allow the user to generate a better estimate of the initial activity for each run through a hands-free detection method.

4.2.2 Radiolabeling process

The $[^{11}C]$MET and $[^{11}C]$Rac cold (C – 12) masses in the collected product samples can be determined in order to calculate the specific activities. One way to achieve this is using the standard addition method.

4.2.3 Computational analysis

A numerical simulation for the flow and species transfer of the reaction progress can be evaluated for comparison to the computational analysis carried out in this investigation. Also, the simulation can be expanded to the full microchip designs' micromixing and reaction modelling using a larger computer memory. Furthermore, implementing other passive micromixer designs to this continuous-flow synthesis model can possibly assist in the microchip redesign process.

Initially, it would be beneficial to carry out the experimental procedures to determine the actual rate constant and activation energy values for this radiolabeling process. Then these values can be used for a more accurate simulation that incorporates temperature variations for the study of multiple microchip designs. Similar to the literature, studying the concentration distributions in different sections of the microchannel for this pseudo-first order reaction can provide a better understanding of the reagent species distribution and interaction. Additionally, a model can be created to investigate the microchip holder and heating device (hot plate) to investigate the heat transfer efficiency.

4.2.4 Microchip redesign

Generating a new microchip design or implementing an existing one requires the examining of optimal parameters that would be beneficial for this pseudo-first order reaction. Due to the low [^{11}C]MeI concentrations it seems necessary to implement a better micromixing device to further reduce diffusion distances. It is believed that achieving better mixing in a shorter channel would be beneficial by reducing the reaction time and hence the possibility for side reactions. For example, a design incorporating a multi-lamination feature along with micromixer beads where two "micromixing" features are combined, could achieve better mixing over short distances [49, 82]. Also, conducting the cold synthesis can be replaced by an extensive CFD study of the process as an initial investigation.

5: APPENDICES

5.1 Appendix A: Data and results

5.1.1 Microchip dimensions

These values provide detailed information about the fabricated microchip designs in our investigation.

Table 5-1 Shows the various PDMS-glass microchip designs and their properties

Microfluidic chip	*Channel width (µm)	*Channel depth (µm)	**Reaction channel length (mm)	Approximate Internal volume (µL)
Meander/No loop	100	100	272	2.7
Abacus	100	100	437	4.4
Full loop	100	100	356	3.6

*Estimated according to fabrication specifications.
**Calculated starting at the main and side inlet junction using the COMSOL Multiphysics® software.

The full loop (channel length = 356 mm) microchip design was implemented in order to maximize the number of micromixer loop structures over the given microchip length in comparison to the no loop (serpentine microchannel with length = 272 mm) design. The abacus (channel length = 437 mm) microchip design was implemented for two reasons: first, to explore the effect of combining the serpentine feature with the micromixer loop feature on a single microchip. Second, alternating between a channel with micromixer loops and a serpentine

channel increases the length compared to the no loop and full loop microchip designs in the same microchip device dimensions.

5.1.2 Temperature Calibration

When observing the synthesis results it was apparent that the optimal reaction temperatures as displayed on the hot plate dial were in reality higher than expected. Understandably, the hot plate reading did not provide the actual temperature on the hot plate surface and within the microchannel, therefore a temperature calibration experiment was carried out using a thermocouple instrument.

The thermocouple works by generating a temperature reading according to a small voltage caused by the temperature difference in two dissimilar metals in each probe. When using the aluminum chip holder base it was found that the temperature on the surface of the hot plate surface was lower than that of the hot plate dial reading (see Figure 5-2). Setting the hot plate dial to higher temperatures showed that the measured microchip surface temperatures increased at a lower rate. This was probably because the Al base is a conducting material and can dissipate heat away from the microchip and therefore reduce its temperature increase rate.
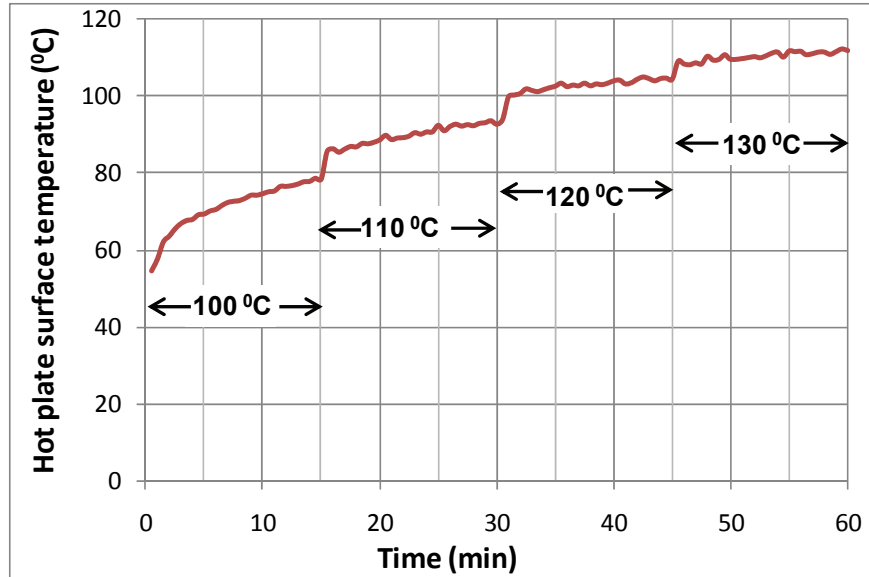
Figure 5-1 Shows the hot plate surface temperature in the Al base holder surface thermocouple temperature readings. The change in the hot plate dial setting is shown at every interval (100 ^{0}C – 130 ^{0}C).
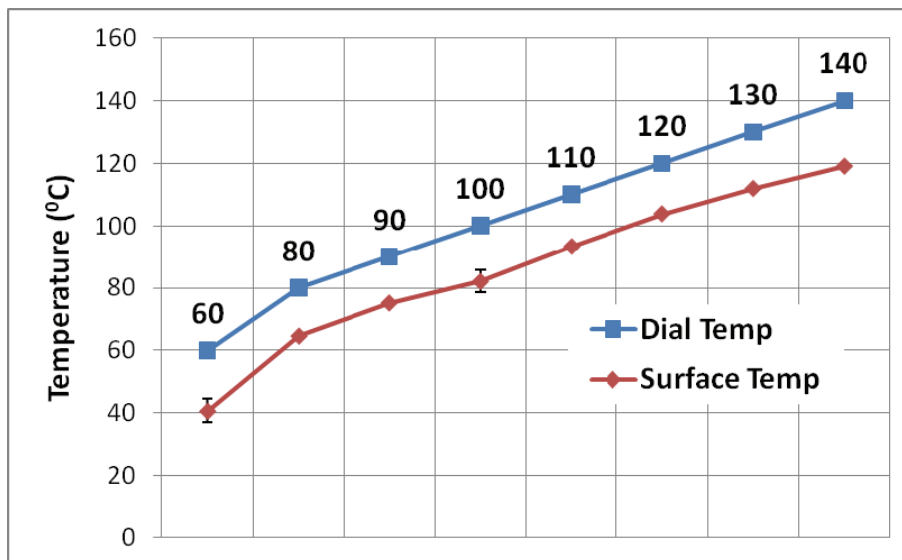
Figure 5-2 Temperature calibration for the PDMS-glass microchip in an Al chip-holder base showing the average hot plate surface temperatures relative to the temperature reading on the hot plate dial.

The hot plate surface temperatures were experimentally determined to be 18 ± 4 ^{0}C lower than the hot plate dial reading. These values were consequently used as experimental temperatures for the microchip synthesis. The hot plate was turned on 15 – 30 min before the start of synthetic experiments and wait times between 3 – 5 min were used between runs by collecting waste vials (not used for analysis).

5.1.3 Cold Rac synthesis

The UV-HPLC shown in Figure 5-3 is an example of a product sample that has been spiked with the IS (2,4-dihydroxybenzoic acid) for the purpose of Rac concentration calculation.
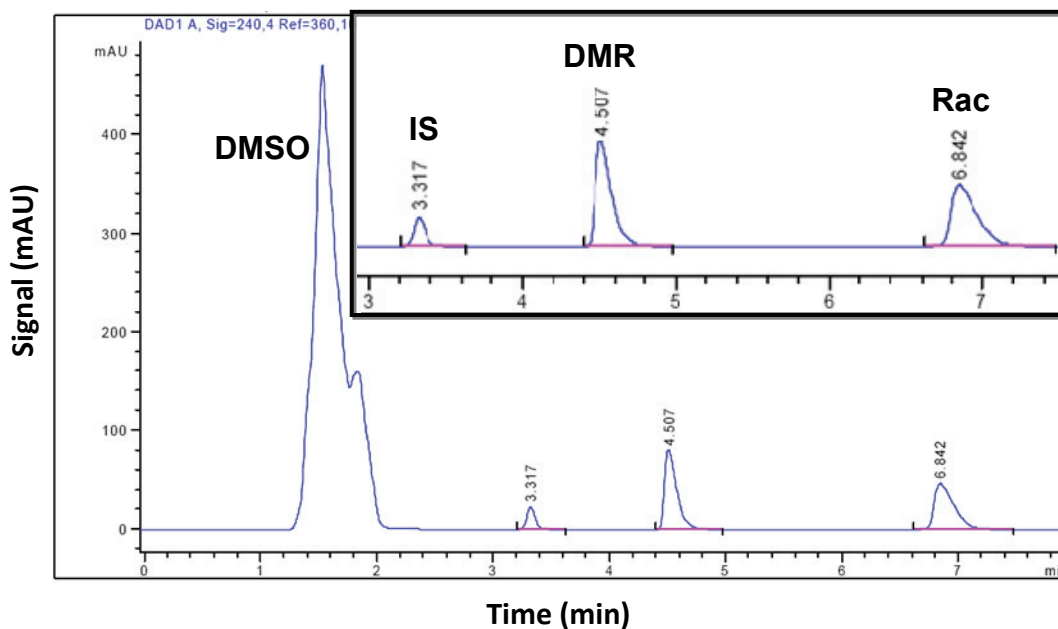
Figure 5-3 Shows the UV-HPLC chromatogram of a IS:DMR:Rac (2:1:1) standard solution. The IS, DMR, and Rac and concentrations used were 130 μM, 523 μM and 480 μM which eluted at 3.3, 4.5 and 6.8 min respectively. The inset expands the region at t = 3 – 8 min.

IS calibration curves were used to quantify the DMR and Rac concentrations in each product sample for the microchip cold synthesis. The concentration ranges were used cover the experimentally relevant values as tabulated in Table 5-2 (the 3 compounds separated in Figure 5-3). These calibration curves were created from the ratio of the DMR peak area or the Rac peak area to the IS peak areas (see Figure 5-4 and Figure 5-5).

Table 5-2 Concentration range of [DMR] and [Rac] used in calibration.

Standard Concentrations (mM)	
[DMR]	[Rac]
0.0024	0.0026
0.0048	0.0052
0.0240	0.0261
0.0480	0.0523
0.2401	0.2614
0.4802	0.5228
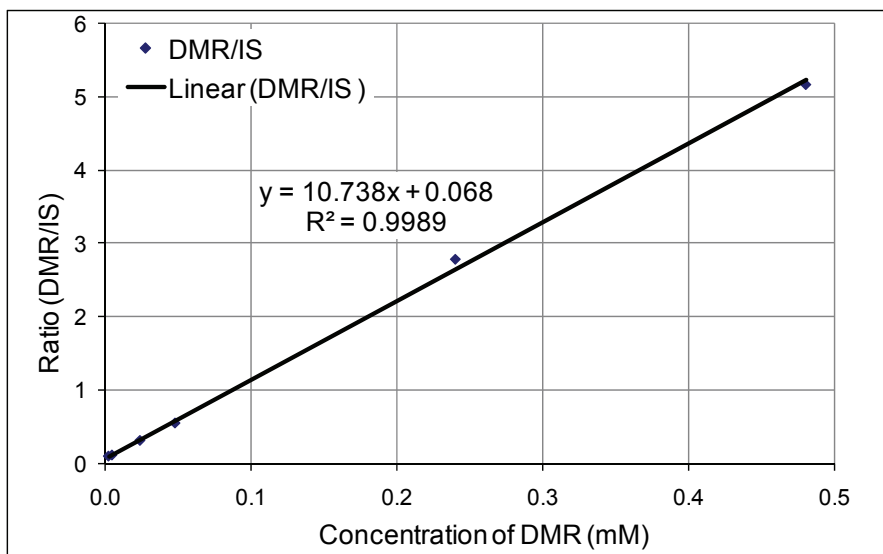
Figure 5-4 Calibration curve using a 1:1 DMR to IS (2,4-dihydroxybenzoic acid) concentrations.
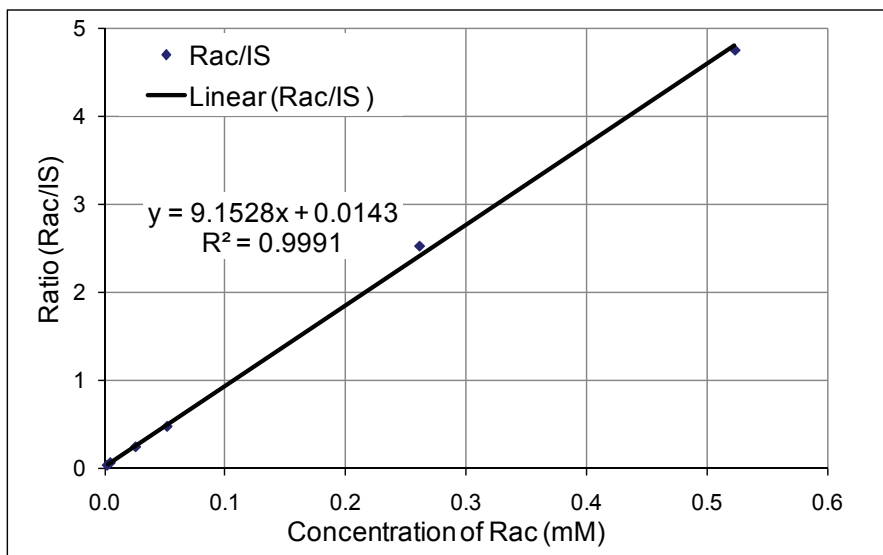
Figure 5-5 Calibration curve using a 1:1 Rac to IS (2,4-dihydroxybenzoic acid) concentrations.

Furthermore, the microchip cold synthesis was conducted on all 3 microchip designs at different temperatures producing various Rac yields and concentrations as shown in Table 5-3. The Rac yields shown in Table 3-1 were calculated using the initial DMR concentrations (~0.2 – 0.4 µmol in 400 µL) and the calculated Rac concentrations shown in Table 5-3.

Table 5-3 Rac concentrations for the cold synthesis performed on the no loop, abacus and full loop microchip designs at 62 – 92 ^{0}C.

Temperature (^{0}C)	[Rac] (µM)		
	No Loop (microchip 1)	Abacus (microchip 3)	Full loop (microchip 5)
62	-	39.9 ± 5.9	156.1 ± 23.5
72	10.6	53.6 ± 5.2	-
82	22.5	77.8*	-
92	35.0	-	-

Note: Reaction conditions include using 0.2 – 0.4 µmol (in 400 µL) of DMR and 120.2 µmol of MeI in 750 µL was used in each reaction at the same flow rate of 8 µL/min in each inlet (16 µL/min for both inlets). All reaction temperatures were calibrated; see Section 5.1.2, Figure 5-1 and Figure 5-2 for more details.
Standard deviation according to the calibration curve is <0.7% for shown data except for data where errors represent standard deviation of results of 2 – 3 experiments.
For the raw data of Rac concentrations see Appendix 5.1.2, Table 5-3.
**For a sample calculation see Section 5.2.1.*

5.1.4 Microchip hot synthesis

5.1.4.1 [^{11}C]MET synthesis

Initially a gradient mobile phase was used for the [^{11}C]MET synthesis. Then with the change in solvent from EtOH to acetone the mobile phase was changed to an isocratic mobile phase with a high MeCN ratio (3:7 Buffer:MeCN). The change was made in order to reduce conditioning time between HPLC runs

and reduce sample loss through activity decay and potential radiolysis while waiting for analysis (see Figure 3-11) [83-84]. HPLC conditioning for the isocratic mobile phase was 3 – 5 min as compared to the ~10 min used for the gradient mobile phase procedure. Another advantage of this method was to obtain a good separation of the L-homo and MET mass peaks on the UV-HPLC, which was a challenge with the gradient mobile phase as seen by the double peaking in Figure 3-10. The MET mass peak's identity was confirmed by spiking standard solution to the product sample as shown by the example in Figure 3-11(b) inset. Since MET has a low UV absorption, a product sample: MET spike ratio of 1:16 was used in order to observe a peak in the chromatogram. MeI (~2.3 min) standard was also added to the product samples in order to spike the solution and determine its location on the UV-HPLC and hence its corresponding [^{11}C]MeI peak (~2.4 min) on the RAD-HPLC.
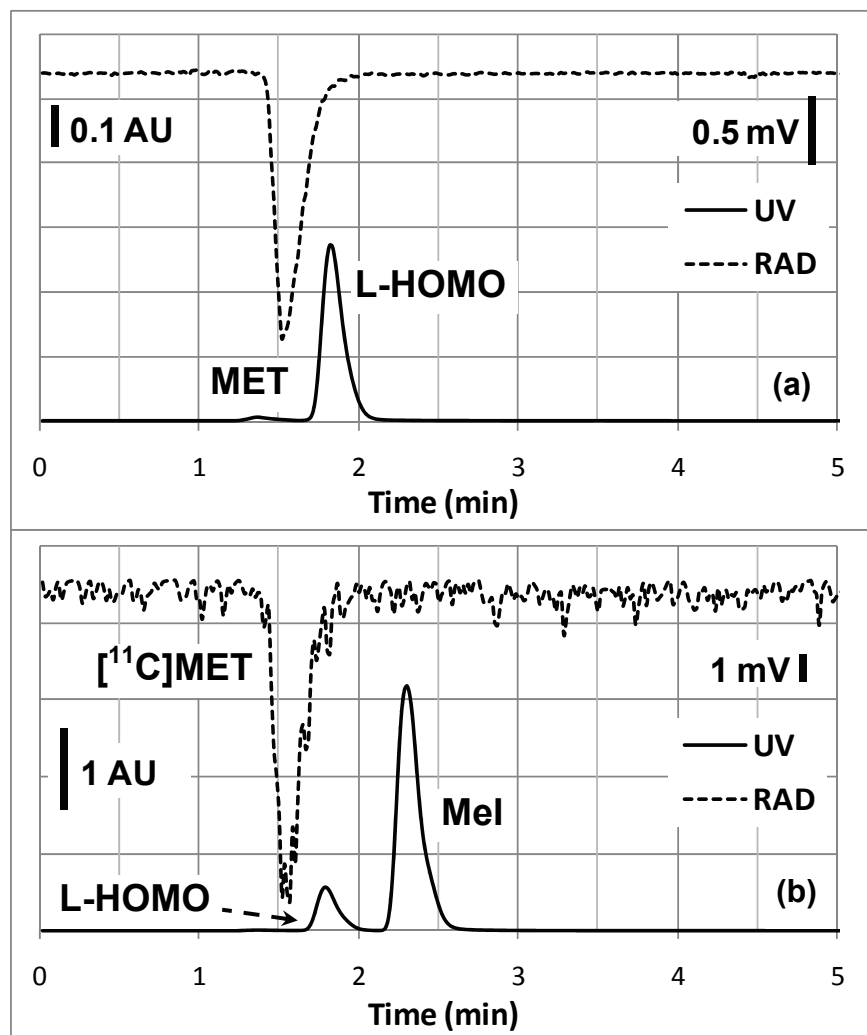
Figure 5-6 (a) UV-HPLC and RAD-HPLC for a product sample using the full loop microchip at 62 ^{0}C and a flow rate of 10 µL/min in Ace/H$_2$O. MET was detected at ~1.4 min and L-homo was detected at ~1.8 min on the UV-HPLC. (b) UV-HPLC and RAD-HPLC for the MeI (10 µL/60 µL) spiking experiment. MeI was detected at ~2.3 min on the UV-HPLC.

5.1.4.2 [^{11}C]Rac synthesis

The radiolabeled precursor [^{11}C]MeI is synthesized by TRIUMF personnel with minimal amounts of the C − 12 counterpart (cold mass). Therefore, when reducing these quantities into smaller aliquots for multiple-run reactions the masses become undetectable through UV-HPLC (see Figure 5-7(a) inset).

Therefore, here the HPLC is shown for a 2 µL/min flow rate with a zoomed-in diagram at 0 – 0.1 AU between 2.5 – 5 min showing no obvious [11C]Rac.
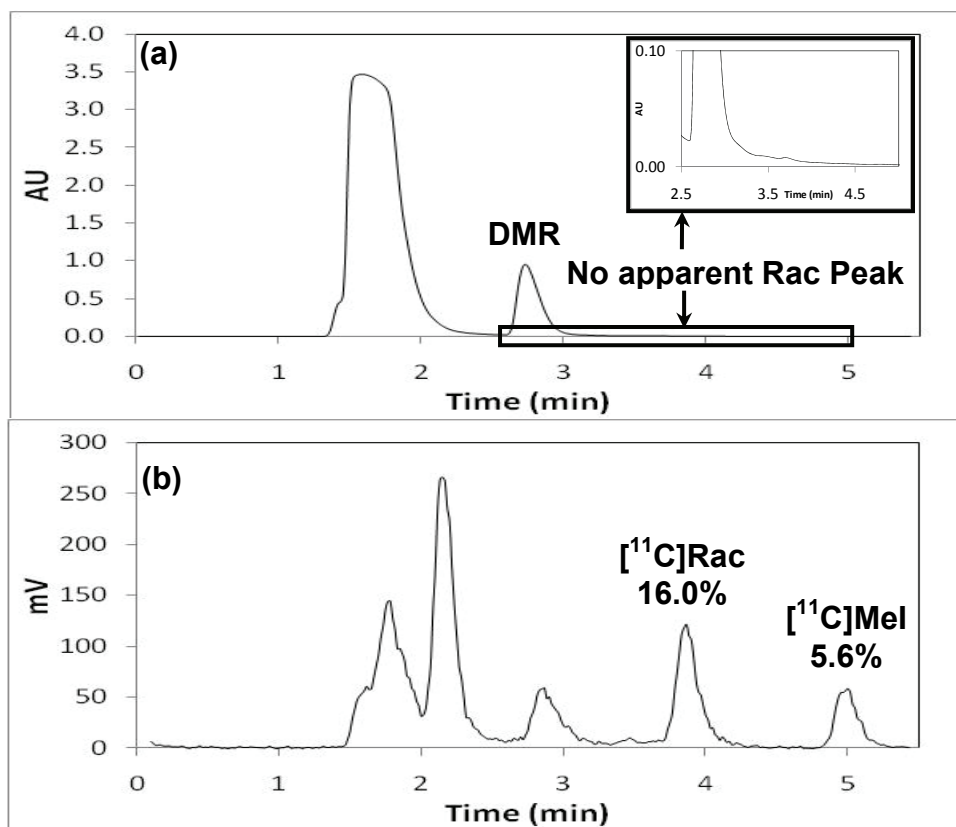
Figure 5-7 (a) UV-HPLC and (b) RAD-HPLC for [11C]Rac synthesis on the abacus microchip at 82 0C and a flow rate of 2 µL/min in premix mode. DMR was detected at ~2.7 min on the UV-HPLC and [11C]Rac and [11C]MeI were detected at ~3.8 and 5.0 min on the RAD-HPLC respectively.

The microchip [11C]Rac synthesis process efficiency was evaluated according to the estimated initial [11C]MeI activities (see Table 5-4 and Table 5-5). The [11C]MeI activities determined from the volume ratio of the dispensed fluid for a run to the total volume of the [11C]MeI is a an estimate of the activity used for that particular run. This information can be used with the [11C]Rac

absolute activity to calculate the RCYs using Equation 3-4. Therefore, the

product samples' activities were measured and decay-corrected using Equation

5-3 for this purpose (see Table 5-4).

Table 5-4 [^{11}C]Rac synthesis calculated total initial and final measured product sample C – 11 activities at varied flow rates using the abacus and full loop microchip where reagents undergo premixed reactions, at 82^{0}C.

Microchip	Flow rate (μL/min)	Estimated initial [DMR] (mmol/L)	*Estimated initial [^{11}C]MeI activity (mCi)	*Product mixture activity (mCi)
Abacus	10	0.2	12.451	4.114
	5	0.2	12.693	3.452
	2	0.2	11.759**	2.067**
Full loop		0.1	5.759	2.553
	2	0.1	4.911	1.442
		0.1	4.799	1.346
		0.2	4.207	1.573

*Decay-corrected activity at the EOB.

 A portion of these data are also represented on Table 3-7, Table 3-8 and Figure 3-14.

**Calculations shown in Section 5.2.2.2

Table 5-5 [^{11}C]Rac synthesis results showing the [^{11}C]MeI and C – 11 side products relative and absolute activities at varied flow rates using the abacus and full loop microchip where reagents undergo premixed reactions, at 82 ^{0}C.

Microchip	Flow rate (μL/min)	[^{11}C] MeI (%)	*[^{11}C]MeI activity (mCi)	C – 11 side products (%)	*Side products activity (mCi)
Abacus	10	83.9	2.107	38.8	1.596
	5	76.2	1.155	55.4	1.911
	2	51.8	0.116	78.4	1.620
Full loop		ND	ND	74.8	1.911
	2	0.06	0.061	70.6	1.017
		ND	ND	74.4	1.002
		0.03	0.029	71.8	1.129

ND = not detected.
*Decay-corrected activity at the EOB.
 A portion of these data are also represented on Table 3-7, Table 3-8 and Figure 3-14.

Furthermore, the activity loss due to the use of a PDMS microchip and experimental setup was monitored by measuring the residue activity in the equipment (the reagent vials for the precursor solution and [^{11}C]MeI solution, syringes and product vials). Once the activity was measured, it was decay-corrected and reported as a percentage of the initial [^{11}C]MeI used in the experiment.

Table 5-6 [^{11}C]Rac synthesis results showing the C – 11 activity loss during two experiments carried out at 82 ^{0}C.

	% Activity (Decay-corrected at EOB)	
	Experiment 1	Experiment 2
Reaction vial 1	4.2	3.5
Reaction vial 2	6.8	9.3
Syringe 1	6.3	9.2
Syringe 2	3.0	1.8
Miscellaneous	63.0	56.4
Product vials (#)[+]	16.7 (14)	19.9 (10)
Initial MeI %	**100**	**100**

Note: The microfluidic system also had activity residue that was not measured. Also these measurements were discontinued due to excessive radiation exposure to the user.
[+]*Number of vials includes waste vials*

5.1.5 Simulation

5.1.5.1 Simulation of an 'Ideal' reactor

The used flow rates were converted to m^3/s from the known reaction values and the cumulative values (a combination of 2 inlet flow rates, see Table 5-7). These values were used for the mass balance (inflow and outflow) setting in the REL to reflect the microchannel flow rate from two combined liquid streams.

Table 5-7 Volumetric flow rate (v) values.

Cumulative Flow rate (µL/min)	v (L/s)
4*	6.7×10^{-8}
10	1.7×10^{-7}
16	2.7×10^{-7}
20	3.3×10^{-7}
24	4.0×10^{-7}
30	5.0×10^{-7}

Two streams of 2 µL/min from each inlet/syringe each give a cumulative flow of 4 µL/min.

Furthermore, for the Rac production down the microreactor length in the cold synthesis, the yield values acquired at different flow rates were normalized with respect to the default 15 µL/min final (outlet of the PFR, see Figure 2-13) yield value of 0.8% (see Table 5-8 and Section 5.1.5.2). The normalized data for these generated yields can be found in Figure 3-18.

Table 5-8 REL acquired final [^{11}C]Rac yield values for the flow rate variation effect on Rac synthesis in PFR 1 (31.0 mm) and PFR 2 (45.6 mm).

Flow rate (µL/min)	Final [^{11}C]Rac yields (%)	
	PFR 1 (31.0 mm)	PFR 2 (45.6 mm)
15	0.8	1.1 *
12	0.9	1.4
10	1.1	1.7
8	1.4	2.1
5	2.2	3.3
2	5.5	8.0

Note: Reaction conditions include using reagent concentrations of [DMR] = 21.6 (5.4 µmol/250 µL) and [[^{11}C]MeI] = 0.024 mmol/L (6 nmol/250 µL) with k = 5.663×10^{-4} (L/(mmol·s)). PFR 1 and PFR 2 represent a tube-like microchannel with the same length as the no loop RU and the abacus RU respectively.
A portion of these data are also represented in Figure 3-19.
*Calculations shown in Section 5.2.3.1.

5.1.5.2 Microchannel flow and mixing investigation

Calculated concentrations for mixing results with the diffusion coefficient of an organic molecule (fluorescein, D = 5 ×10^{-10} m^2/s) in water for initial concentrations of 0 and 1 mmol/L at each inlet:

Table 5-9 Outlet concentrations for mixing in the various microchip designs' RUs at a flow rate of 12, 6 and 2 µl/min at each inlet with an initial species concentrations of 0 mmol/L and 1 mmol/L, respectively.

Cumulative Flow rate (µL/min)	No loop	Abacus	Full loop
	Final outlet concentrations (mmol/L)		
24	0.5054	0.5091	0.5048
12	0.5073	0.5113	0.5034
4	0.5073	0.5112	0.5059

5.1.5.3 Reaction modeling

The RU's outlet concentrations acquired in the hot synthesis modelling flow rate study in the 2 mixing modes are displayed in Table 5-10. These values show the flow rate and reaction mode effect on the RCYs.

Table 5-10 Reaction mode effect on the [^{11}C]Rac yields in the no loop, abacus and full loop design at various flow rates.

Flow rate (µL/min)	[^{11}C]Rac RCY (%)				
	No loop Flow mix	Abacus Flow mix	Abacus Premix	Full loop Flow mix	Full loop Premix
15	0.11	0.16	0.64	0.14	0.63
12	0.15	0.23	-	0.20	-
10	0.20	0.30	0.90	0.26	0.87
8	0.27	0.40	-	0.36	-
5	0.49	0.73	-	0.67	-
2	1.35	2.01	3.65	1.88	3.55

Note: Reaction conditions include using reagent concentrations of [DMR] = 21.6 (5.4 µmol/250 µL) and [[^{11}C]MeI] = 0.024 mmol/L (6 nmol/250 µL) with k = 5.663×10^{-4} (L/(mmol·s)) and D = 10^{-9}m^2/s.
**Calculation shown in Section 5.2.3.3.

Also, actual yields calculated from other investigated parameters (D, reagent concentrations and k) for the synthesis modelling are shown in Table 5-11. This data has been normalized for better reference and data analysis.

Table 5-11 The effect of reagent concentration, diffusion coefficient and rate constant variation on the [^{11}C]Rac yield on the full loop RU using a flow rate of 2 µL/min in flow mix mode.

Variation	Reaction condition	Rac yield (%)
	*Default concentrations, $D = 10^{-9}$ m^2/s, $k = 5.663\times10^{-4}$ L/(mmol·s), Flow mix	1.88
D (m^2/s)	*Default concentrations, **$D = 10^{-8}$ m^2/s**, $k = 5.663\times10^{-4}$ L/(mmol·s), Flow mix	1.99
k (L/(mmol·s))	*Default concentrations, $D = 10^{-9}$ m^2/s, **$k = 5.663\times10^{-6}$ L/(mmol·s)**, Flow mix	1.92×10^{-2}
	*Default concentrations, $D = 10^{-9}$ m^2/s, **$k = 5.663\times10^{-8}$ L/(mmol·s)**, Flow mix	1.92×10^{-4}
Reagent amount (mmol/L)	****High concentrations**, $D = 10^{-9}$ m^2/s, $k = 5.663\times10^{-4}$ L/(mmol·s), Flow mix	4.44
	High concentrations, $D = 10^{-9}$ m^2/s, $k = 5.663\times10^{-4}$ L/(mmol·s), **Premix	8.00

Note: The final yields produced by the no loop design RU simulation with default reaction conditions at a flow rate of 15 µL/min is set to 1 and is used to normalize all the raw data. A portion of these data are also represented in Section 5.1.5.3, Table 5-11.
*Default: Reaction conditions include using [[^{11}C]MeI] = 2.4×10^{-2} mmol/L and [DMR] = 21.6 mmol/L which are related to the hot synthesis concentrations.
**High concentration: Reaction conditions include using [MeI] = 53.4 mmol/L and [DMR] = 21.6 mmol/L which are related to the cold synthesis concentrations.

5.2 Appendix B: Sample calculations

5.2.1 Cold Rac synthesis

An example of Rac yield calculations as shown in Table 3-1 is demonstrated using the experimental data results for the abacus (microchip 3) where 40 µL (flow rate: 2 × 8 µL/min and 5 min collection) of 0.24 µmol of DMR and 40 µL of 120.2 µmol MeI are used at a reaction temperature of 82 ^{0}C. Then the [Rac] mM calculation using the IS method is as follows:

From the Rac calibration curve equation (see Figure 5-5):

$$y = 9.1528x + 0.0143$$

Where y is the peak area ratio of Rac to IS and x = [Rac] mM. From the results the Rac peak area = 61.2476 and the IS peak area = 84.3664. Therefore, x can be calculated:

$$x = \frac{\left(\frac{61.2476}{84.3664}\right) - 0.0143}{9.1528}$$

$$= 0.0778 \text{ mM}$$

In this case the collected volume was 80 μL (5 min run time at a flow rate of 8 μL/min from 2 syringes) of product solution and 100 μL of ammonium formate was added to quench the solution, hence a total of 180 μL. Therefore, the number of moles of Rac (n_{Rac}) are:

$$n_{Rac} = 77.8 \text{ μM} * 180 \text{ μL}$$

$$= 1.4 \times 10^{-2} \text{μmol}$$

Therefore the Rac yield (%) is:

$$\text{Rac yield (\%)} = \frac{n_{Rac}}{n_{DMR}} * 100\%$$

$$= \frac{1.4 \times 10^{-2} \text{ μmol}}{0.24 \text{ μmol}} * 100\%$$

$$= 5.8 \text{ \% (Listed in Table 3-1)}$$

5.2.2 Hot synthesis

5.2.2.1 [^{11}C]MET synthesis

An example of [^{11}C]MET relative activity calculations is demonstrated using the experimental data results for abacus microchip design, in flow mix mode at a flow rate of 10 uL/min at 42 ^{0}C (see Table 3-3). The relative activity is calculated from the total detected C − 11 peak areas using Equation 3-1, as follows:

$$[^{11}\text{C}]\text{MET Relative Activity (\%)} = \frac{[^{11}\text{C}]\text{MET RAD HPLC pk area} * 100\%}{\text{Total RAD HPLC pk areas}}$$

$$= \frac{(731289)\ \text{mV} \cdot \text{min} * 100\%}{(771980 + 731289\ )\text{mV} \cdot \text{min}}$$

$$= 48.6\% \text{ (Listed on Table 3-3)}$$

$$[^{11}\text{C}]\text{MeI Activity (\%)} = \frac{[^{11}\text{C}]\text{MeI RAD HPLC pk area} * 100\%}{\text{Total RAD HPLC pk areas}}$$

$$= \frac{(771980)\ \text{mV} \cdot \text{min} * 100\%}{(771980 + 731289\ )\text{mV} \cdot \text{min}}$$

$$= 51.4\% \text{ (Listed on Table 3-3)}$$

5.2.2.2 [^{11}C]Rac synthesis

To better understand the radiolabeling process one must know the units of radioactivity. The activity (A) of a sample is usually expressed through the decay rate of the parent nucleus. The unit often used for this is disintegrations per second (dps) and the equation for activity can be written as follows:

Equation 5-1 Activity of a radionuclide [5].

$$A = -\frac{dN}{dt}$$

Where, N is the initial number of parent nuclei and t is the decay time. One dps is equivalent to 1 becquerel (Bq) which is the SI unit for activity [3, 5]. Another commonly used unit is Curie (Ci) which is equivalent to 3.7×10^{10} Bq. It is worth noting that Ci levels of activity are considered very "hot" and are highly radioactive [5]. Therefore, working levels of activity for radiotracer studies are usually at mCi levels of activity [5]. Also, the activity values are used to calculate the specific activity (SA) which is ratio of the activity (Ci) of a radiolabeled compound to its non-radioactive counterpart (C – 12 mol) [3, 5, 15]. This variable is dependent on the radionuclide decay and hence decreases with time [15].

An important property of a radionuclide is its half-life which is the time it takes for the radioactive nuclide to decay by half of its amount. It is calculated using the following equation:

Equation 5-2 Half-life equation.

$$t_{1/2} = \frac{\ln 2}{\lambda}$$

Where λ (min^{-1}) is the decay constant for the particular radionuclide [5]. The half-life value is important in determining the ^{11}C – labelled precursor initial activity required depending on the duration of the radiotracer production process which usually includes the purification and quality control (see Equation 5-3) [11].

Equation 5-3 Radioactivity decay-correction equation.

$$A_0 = A_t \cdot e^{\lambda t}$$

Where A_0 (Ci) is the activity at the end of target bombardment (End of bombardment = EOB), A_t (Ci) is the measured activity at time t (min) after EOB and λ is given by Equation 5-2. For example, a 45-min production process for ^{11}C- radiolabeling results in up to 80% of decay related losses.

The radiolabeled precursor's activity value was then used to calculate the radiotracer decay-corrected yields. Where A_0 (Ci) is the activity at EOB, A_t (Ci) is the absolute activity at time t (min) after EOB and λ= ln $2/t_{1/2}$ (min^{-1}) is the decay constant with a C – 11 half-life ($t_{1/2}$) of 20.4 min. Therefore, for a reaction where a collected product sample's activity was 0.401 mCi at 48 min and 16 s after EOB ($[^{11}$C]Rac synthesis on the abacus microchip at a flow rate of 10 uL/min at 82 ^{0}C in premix mode), then the decay-corrected activity can be calculated as follows:

$$A_0 = 0.401 \text{ mCi} * \exp\left(\frac{\ln 2}{20.4 \text{ min}} * 48.2667 \text{ min}\right)$$

$$= 2.067 \text{ mCi (Listed on Table 5-4)}$$

Using the $[^{11}$C]Rac relative activity and the decay-corrected product activities the $[^{11}$C]Rac activity was calculated, and then used to calculate the conversion and RCY (see Equation 3-3 and Equation 3-4) in the following procedure.

Step 1: Calculating the estimated initial $[^{11}$C]MeI activity (A_0)
The trapped $[^{11}$C]MeI activity = 124.522 mCi, therefore,

$$\text{Initial } [^{11}\text{C}]\text{MeI } (A_0) \text{ in sample} = \frac{(\text{flow rate} * \text{Collection time})}{\text{MeCN volume}} * [^{11}\text{C}]\text{MeI activity}$$

$$= \frac{(2\mu\text{L/min} * 14.2\text{min})}{300\mu\text{L}} * 124.522\text{mCi}$$

$$= 11.759 \text{ mCi (Listed on Table 5-4)}$$

Step 2: Calculate the product sample [^{11}C]Rac activity

$$[^{11}\text{C}]\text{Rac absolute activity} = [^{11}\text{C}]\text{Rac Activity } (\%) * \text{Product sample activity}$$

$$= 16.0\% * 2.067 \text{ mCi}$$

$$= 0.331 \text{ mCi (Listed on Table 3-8)}$$

Step 3: Calculate the [^{11}C]Rac conversion and RCY (%)

$$[^{11}\text{C}]\text{Rac conversion } (\%) = \frac{[^{11}\text{C}]\text{Rac RAD HPLC pk area} * 100\%}{\text{Total RAD HPLC pk areas} - \text{unreacted } [^{11}\text{C}]\text{MeI RAD HPLC pk areas}}$$

$$= \frac{(962750) \text{ mV} \cdot \text{min}}{(6029693 - 338694)\text{mV} \cdot \text{min}} * 100\%$$

$$= 16.9\% \text{ (Listed on Table 3-7)}$$

$$[^{11}\text{C}]\text{Rac RCY } (\%) = \frac{[^{11}\text{C}]\text{Rac Activity} * 100\%}{\text{Initial } [^{11}\text{C}]\text{MeI activity in each product sample}}$$

$$= \frac{0.331 \text{ mCi}}{11.759 \text{ mCi}} * 100\%$$

$$= 2.8\% \text{ (Listed on Table 3-8)}$$

5.2.3 Simulation

5.2.3.1 Simulation of an 'Ideal' reactor

The REL data was normalized using PFR 1's default conditions (using reagent concentrations of [DMR] = 21.6 mmol/L (5.4 µmol/250 µL) and [[^{11}C]MeI] = 0.024 mmol/L (6 nmol/ 250 µL) and k = 5.663×10^{-4} (L/(mmol·s)) at a flow rate of 15 µL/min (5.0 × 10^{-7} L/s). The RCY produced was 0.7552% and was set to 1. Therefore at a flow rate of 2 µL/min the RCY of 5.5117% can be normalized as follows:

$$\text{Normalized Rac yield} \ = \ \frac{\text{RCY at 2 µL/min}}{\text{RCY at 15 µL/min}}$$

$$= \ \frac{5.5118\%}{0.7552\%}$$

$$= \ 7.3\% \text{ (Displayed in Figure 3-17)}$$

The molar flow rate (F_i) was used in the REL investigations as the property of mass flow of reagent species within the PFR. An example of this calculation is demonstrated for the [DMR] = 21.6 mmol/L (5.4 µmol/250 µL) and v = 15 µL/min = 5.0 × 10^{-7} L/s.

$$F_i = c_i * v$$

$$= \left(21.6 \ \frac{\text{mmol}}{\text{L}}\right) * \left(5 \times 10^{-7} \ \frac{\text{L}}{\text{s}}\right)$$

$$= 1.1 \times 10^{-5} \ \frac{\text{mmol}}{\text{s}}$$

The COMSOL software used the following equation to calculate the Rac yield:

$$\text{Rac yield (\%)} = \frac{\text{F\_Rac}}{\text{F}_0\_\text{MeI}} * 100\%$$

An example of this calculation is demonstrated using the results for the PFR 1 hot synthesis investigation at a flow rate of 15 µL/min using reagent concentrations of [DMR] = 21.6 mmol/L (5.4 µmol/250 µL) and [[^{11}C]MeI] = 0.024 mmol/L and k = 5.663×10^{-4} (L/(mmol·s)).

$$\text{F}_0\_\text{MeI} = \text{c}_0\_\text{MeI} * v$$

$$= \left(0.024\frac{\text{mmol}}{\text{L}}\right) * (5.00 \times 10^{-7}\frac{\text{L}}{\text{s}})$$

$$= 1.20 \times 10^{-8}\frac{\text{mmol}}{\text{s}}$$

From results, F_Rac = 1.330×10^{-10} mol/s therefore:

$$\text{Rac yield (\%)} = \frac{1.330 \times 10^{-10}\frac{\text{mol}}{\text{s}}}{1.2 \times 10^{-8}\frac{\text{mol}}{\text{s}}} * 100\%$$

$$= 1.1\% \text{ (Listed on Table 5-8)}$$

5.2.3.2 Microchannel flow calculations

Reynold's number (R_e) is a dimensionless parameter that represents the ratio of inertial forces to the viscous forces for a given flow (see Equation 5-4). This value can be used to describe the relative pressure-driven flow within the

microchannels [71]. Reynolds numbers >2300 indicate turbulent flow while values <2300 indicate laminar flow [71].

Equation 5-4 Reynolds number.

$$R_e = \frac{\rho v d}{\eta}$$

Where ρ = density of the fluid (kg/m^3), v = average velocity of the fluid (m/s), η = dynamic viscosity in kg/(s*m) and d = effective hydraulic diameter in m. Since the Reynolds number value is proportional to d – which is very small in the case of microfluidics – it can be assumed that R_e is very small and hence flow is laminar in most cases. Table 5-12 shows the R_e calculated for the microchannels demonstrating laminar flow at various flow rates.

Table 5-12 Reynolds number for the various flow rates investigated in the micromixing and chemical synthesis simulations for our 100 μm × 100 μm microchannels.

Flow rate (μL/min)	R_e
15	5.60
12	4.48*
10	3.73
8	2.99
6	2.24
5	1.87
2	0.75

**Calculation shown below.

First the effective hydraulic diameter is corrected for different microchannel dimensions.

$$d = \frac{64 D_h}{k}$$

Where, D_h = hydraulic diameter, k = correction factor for a cross-section. In the case of a 100 μm square channel, $k = 56.91$ [71]:

$$d = \frac{64(100 \text{ μm})}{56.91}$$

$$d = 112 \text{ μm}$$

Therefore, for water ($\rho = 10^3$ kg/m^3, $\eta = 10^{-3}$ kg/(m·s)), flowing at 0.02 m/s (12 μL/min):

$$R_e = \frac{\left(10^3 \frac{\text{kg}}{\text{m}^3}\right)(0.04 \frac{\text{m}}{\text{s}})(112 \text{ μm})}{(10^{-3} \frac{\text{kg}}{\text{m} \cdot \text{s}})}$$

$$= 4.48 \text{ (Listed on Table 5-12)}$$

This value is significantly lower than 2300, which indicates laminar flow in the microchannels for our process [71]. It is usually very low in the case of microfluidics indicating laminar flow in most cases.

5.2.3.3 Reaction modelling

Rac yields were calculated with respect to the initial MeI concentrations for the space-dependant model.

$$\text{Rac yield (\%)} = \frac{[\text{Rac}]}{[\text{MeI}]_0} * 100\%$$

For example, for the abacus design RU's hot synthesis investigation at a flow rate of 15 µL/min and k = 5.663×10^{-4} (L/(mmol·s)) with reagents concentrations of [DMR] = 21.6 mmol/L (5.4 µmol/250 µL) and [^{11}C]MeI = 0.024 mmol/L (6 nmol/ 250 µL) in flow mix mode, the Rac yield was calculated as follows:

At the outlet the generated [Rac] = 3.854×10^{-5} mmol/L is therefore;

$$\text{Rac yield (\%)} = \frac{3.854 \times 10^{-5} \frac{\text{mmol}}{\text{L}}}{2.4 \times 10^{-2} \frac{\text{mmol}}{\text{L}}} * 100\%$$

$$= 0.16\% \text{ (Listed on Table 5-10)}$$

The MEMS module data was normalized using the no loop design RU's default conditions (using reagent concentrations of [DMR] = 21.6 mmol/L (5.4 µmol/250 µL) and [[^{11}C]MeI] = 0.024 mmol/L (6 nmol/ 250 µL) and k = 5.663×10^{-4} (L/(mmol·s)) at a flow rate of 15 µL/min (5.0 × 10^{-7} L/s). The RCY produced was 0.1066% and was set to 1 (see Table 5-8). Therefore at a flow rate of 2 µL/min, the RCY for the full loop RU is 1.8786% can be normalized as follows:

$$\text{Normalized Rac yield} = \frac{\text{RCY at 2 µL/min}}{\text{RCY at 15 µL/min}}$$

$$= \frac{1.8786\%}{0.1066\%}$$

$$= 17.6\% \text{ (Listed on Table 3-9)}$$

REFERENCE LIST

1.   Blokland, J.A.K., et al., *Positron emission tomography: a technical introduction for clinicians.* European Journal of Radiology, 2002. **44**(1): p. 70-75.

2.   Miller, P.W., et al., *Synthesis of C-11, F-18, O-15, and N-13 Radiolabels for Positron Emission Tomography.* Angewandte Chemie-International Edition, 2008. **47**(47): p. 8998-9033.

3.   Welch, M.J. and C.S. Redvanly, *Handbook of radiopharmaceuticals : radiochemistry and applications*. 2003, New York: J. Wiley. xiv, 848 p. 42 - 44, 73 - 75, 142-169.

4.   Bailey, D.L., SpringerLink (Online service), and MyiLibrary., *Positron emission tomography basic sciences*. 2005, Springer: New York. p. x, 382 p. 30-32, 50.

5.   Ehmann, W.D. and D.E. Vance, *Radiochemistry and nuclear methods of analysis*. Chemical analysis ;. 1991, New York: Wiley. xviii, 531 p. 113-121, 313-318, 338-340, 466-470.

6.   Valk, P.E. and SpringerLink (Online service), *Positron emission tomography clinical practice*. 2006, Springer: London. p. xiv, 475 p.3.

7.   Phelps, M.E., *Molecular imaging with positron emission tomography.* Annual Review of Nuclear and Particle Science, 2002. **52**: p. 303-338.

8.   Wang, M.W., et al., *Microfluidics for Positron Emission Tomography Probe Development.* Molecular Imaging, 2010. **9**(4): p. 175-191.

9.   Paans, A.M.J., et al., *Positron emission tomography: the conceptual idea using a multidisciplinary approach.* Methods, 2002. **27**(3): p. 195-207.

10.   Hoehr, C., et al., *TR13 Safety Report.* 2009.

11.   Serdons, K., A. Verbruggen, and G.M. Bormans, *Developing new molecular imaging probes for PET.* Methods, 2009. **48**(2): p. 104-111.

12.   *Positron Emission Tomography Programme at the University of British Columbia* [September 10, 2010]; Available from: http://legacyweb.triumf.ca/pethome/pethome.htm, http://www.pet.ubc.ca/.

13.   Cheung, M.K. and C.L. Ho, *A simple, versatile, low-cost and remotely operated apparatus for [11C]acetate, [11C]choline, [11C]methionine and [11C]PIB synthesis.* Appl Radiat Isot, 2009. **67**(4): p. 581-9.

14. Link, J.M., K.A. Krohn, and J.C. Clark, *Production of [11C]CH3I by single pass reaction of [11C]CH4 with I2.* Nucl Med Biol, 1997. **24**(1): p. 93-7.

15. Lu, S.Y., et al., *Syntheses of C-11- and F-18-labeled carboxylic esters within a hydrodynamically-driven micro-reactor.* Lab on a Chip, 2004. **4**(6): p. 523-525.

16. Lu, S.Y. and V.W. Pike, *Micro-reactors for PET tracer labeling.* Ernst Schering Res Found Workshop, 2007(62): p. 271-87.

17. *GE Healthcare.* September 18, 2010]; Available from: http://www.gehealthcare.com/euen/fun_img/products/radiopharmacy/products/tracercenter_radiopharmacy.html.

18. Langstrom, B., et al., *SYNTHESIS OF L- METHYL-C-11 METHIONINE AND D- METHYL-C-11 METHIONINE.* Journal of Nuclear Medicine, 1987. **28**(6): p. 1037-1040.

19. Pascali, C., et al., *High efficiency preparation of L- S-methyl-C-11 methionine by on-column C-11 methylation on C18 Sep-Pak.* Journal of Labelled Compounds & Radiopharmaceuticals, 1999. **42**(8): p. 715-724.

20. Berridge, M.S., E.H. Cassidy, and F. Miraldi, *C-11 ACETATE AND C-11 METHIONINE - IMPROVED SYNTHESES AND QUALITY-CONTROL.* Applied Radiation and Isotopes, 1995. **46**(3): p. 173-175.

21. Berger, G., et al., *Automated synthesis of 11C-labelled radiopharmaceuticals: imipramine, chlorpromazine, nicotine and methionine.* Int J Appl Radiat Isot, 1979. **30**(7): p. 393-9.

22. Langer, O., et al., *Precursor synthesis and radiolabelling of the dopamine D-2 receptor ligand C-11 raclopride from C-11 methyl triflate.* Journal of Labelled Compounds & Radiopharmaceuticals, 1999. **42**(12): p. 1183-1193.

23. Nagren, K. and C. Halldin, *Methylation of amide and thiol functions with C-11 methyl triflate, as exemplified by C-11 NMSP, C-11 flumazenil and C-11 methionine.* Journal of Labelled Compounds & Radiopharmaceuticals, 1998. **41**(9): p. 831-841.

24. Adam, M.J., et al., *C-11-methylations using C-11-methyl iodide and tetrabutylammonium fluoride.* Radiochimica Acta, 2000. **88**(3-4): p. 207-209.

25. Fei, X.S., et al., *An improved synthesis of PET dopamine D-2 receptors radioligand C-11 raclopride.* Synthetic Communications, 2004. **34**(10): p. 1897-1907.

26. Wirth, T., *Microreactors in organic synthesis and catalysis.* 2008, Weinheim: Wiley-VCH. xiv, 283 p. 1,19, 43-53.

27. Watts, P. and S.J. Haswell, *The application of micro reactors for organic synthesis.* Chemical Society Reviews, 2005. **34**(3): p. 235-246.

28. Watts, P. and C. Wiles, *Micro reactors: a new tool for the synthetic chemist.* Organic & Biomolecular Chemistry, 2007. **5**(5): p. 727-732.

29. Hartman, R.L. and K.F. Jensen, *Microchemical systems for continuous-flow synthesis.* Lab on a Chip, 2009. **9**(17): p. 2495-2507.

30. Miller, P.W., *Radiolabelling with short-lived PET (positron emission tomography) isotopes using microfluidic reactors.* Journal of Chemical Technology and Biotechnology, 2009. **84**(3): p. 309-315.

31. Fletcher, P.D.I., et al., *Micro reactors: principles and applications in organic synthesis.* Tetrahedron, 2002. **58**(24): p. 4735-4757.

32. Zimmerman, W.B.J. and International Centre for Mechanical Sciences., *Microfluidics : history, theory and applications*. CISM courses and lectures ;. 2006, Wien ; New York: Springer. 304 p. 1, 5, 106-111.

33. Ratner, D.M., et al., *Microreactor-based reaction optimization in organic chemistry glycosylation as a challenge.* Chemical Communications, 2005(5): p. 578-580.

34. Ueno, M., et al., *Phase-transfer alkylation reactions using microreactors.* Chemical Communications, 2003(8): p. 936-937.

35. Brivio, M., W. Verboom, and D.N. Reinhoudt, *Miniaturized continuous flow reaction vessels: influence on chemical reactions.* Lab Chip, 2006. **6**(3): p. 329-44.

36. Haswell, S.J., B. O'Sullivan, and P. Styring, *Kumada-Corriu reactions in a pressure-driven microflow reactor.* Lab on a Chip, 2001. **1**(2): p. 164-166.

37. Wilson, N.G. and T. McCreedy, *On-chip catalysis using a lithographically fabricated glass microreactor - the dehydration of alcohols using sulfated zirconia.* Chemical Communications, 2000(9): p. 733-734.

38. Lu, H., M.A. Schmidt, and K.F. Jensen, *Photochemical reactions and on-line UV detection in microfabricated reactors.* Lab on a Chip, 2001. **1**(1): p. 22-28.

39. Hisamoto, H., et al., *Fast and high conversion phase-transfer synthesis exploiting the liquid-liquid interface formed in a microchannel chip.* Chemical Communications, 2001(24): p. 2662-2663.

40. Elizarov, A.M., *Microreactors for radiopharmaceutical synthesis.* Lab Chip, 2009. **9**(10): p. 1326-33.

41. Brady, F., et al., *Use of microfabricated devices for radiosynthesis of radiotracers for positron emission tomography*. 2003, Imaging Research Solutions Ltd. p. 25 pp.

42. McDonald, J.C., et al., *Fabrication of microfluidic systems in poly(dimethylsiloxane).* Electrophoresis, 2000. **21**(1): p. 27-40.

43.   Li, P.C.H., *Microfluidic lab-on-a-chip for chemical and biological analysis and discovery*. Chromatographic science series. 2006, Boca Raton: Taylor & Francis/CRC Press. 504 p. 19, 75 - 81.

44.   Zaouk, R., B.Y. Park, and M.J. Madou, *Fabrication of polydimethylsiloxane microfluidics using SU-8 molds.* Methods Mol Biol, 2006. **321**: p. 17-21.

45.   Cubaud, T. and C.M. Ho, *Transport of bubbles in square microchannels.* Physics of Fluids, 2004. **16**(12): p. 4575-4585.

46.   deMello, A.J., *Control and detection of chemical reactions in microfluidic systems.* Nature, 2006. **442**(7101): p. 394-402.

47.   Nguyen, N.T. and Z.G. Wu, *Micromixers - a review.* Journal of Micromechanics and Microengineering, 2005. **15**(2): p. R1-R16.

48.   Hessel, V., H. Lowe, and F. Schonfeld, *Micromixers - a review on passive and active mixing principles.* Chemical Engineering Science, 2005. **60**(8-9): p. 2479-2501.

49.   Meijer, H.E.H., et al., *Passive and Active Mixing in Microfluidic Devices.* Macromolecular Symposia, 2009. **279**: p. 201-209.

50.   Mansur, E.A., et al., *A state-of-the-art review of mixing in microfluidic mixers.* Chinese Journal of Chemical Engineering, 2008. **16**(4): p. 503-516.

51.   Hossain, S., et al., *Analysis and optimization of a micromixer with a modified Tesla structure.* Chemical Engineering Journal, 2010. **158**(2): p. 305-314.

52.   Hossain, S., M.A. Ansari, and K.Y. Kim, *Evaluation of the mixing performance of three passive micromixers.* Chemical Engineering Journal, 2009. **150**(2-3): p. 492-501.

53.   Lin, Y.C., Y.C. Chung, and C.Y. Wu, *Mixing enhancement of the passive microfluidic mixer with J-shaped baffles in the tee channel.* Biomed Microdevices, 2007. **9**(2): p. 215-21.

54.   Garstecki, P., et al., *Mixing with bubbles: a practical technology for use with portable microfluidic devices.* Lab on a Chip, 2006. **6**(2): p. 207-212.

55.   Cherlo, S.K.R., K. Sreenath, and S. Pushpavanam, *Screening, Selecting, and Designing Microreactors.* Industrial & Engineering Chemistry Research, 2009. **48**(18): p. 8678-8684.

56.   Bruus, H., *Theoretical microfluidics.* Oxford master series in physics ;. 2008, Oxford ; New York: Oxford University Press. 346 p. 1, 20, 41.

57.   Buddoo, S., et al., *Study of the pyrolysis of 2-pinanol in tubular and microreactor systems with reaction kinetics and modelling.* Chemical Engineering and Processing, 2009. **48**(9): p. 1419-1426.

58.   Shih, T.R. and C.K. Chung, *A high-efficiency planar micromixer with convection and diffusion mixing over a wide Reynolds number range.* Microfluidics and Nanofluidics, 2008. **5**(2): p. 175-183.

59.   Kim, D.S., et al., *A serpentine laminating micromixer combining splitting/recombination and advection.* Lab Chip, 2005. **5**(7): p. 739-47.

60.   Yang, J.T., et al., *A chaotic micromixer modulated by constructive vortex agitation.* Journal of Micromechanics and Microengineering, 2007. **17**(10): p. 2084-2092.

61.   Jeon, W. and C.B. Shin, *Design and simulation of passive mixing in microfluidic systems with geometric variations.* Chemical Engineering Journal, 2009. **152**(2-3): p. 575-582.

62.   MICROCHEM, *Nano^{TM}SU-8 Negative Tone Photoresist Formulations 50 - 100*: Newton, MA.

63.   Duffy, D.C., et al., *Rapid prototyping of microfluidic systems in poly(dimethylsiloxane).* Analytical Chemistry, 1998. **70**(23): p. 4974-4984.

64.   Haubert, K., T. Drier, and D. Beebe, *PDMS bonding by means of a portable, low-cost corona system.* Lab Chip, 2006. **6**(12): p. 1548-9.

65.   Bioscan, I., *FLOW-COUNT EVERYTHING YOU NEED TO KNOW AND ONE OR TWO THINGS YOU DON'T*. 2006: Washington, DC.

66.   Comar, D., et al., *Labelling and metabolism of methionine-methyl-11 C.* Eur J Nucl Med, 1976. **1**(1): p. 11-4.

67.   COMSOLMultiphysics, *COMSOL Reaction Engineering Lab user's guide.* p. p. 43 - 46.

68.   Levenspiel, O., *Chemical reaction engineering.* 3rd ed. 1999, New York: Wiley. xvi, 668 p. 101-104.

69.   Langstrom, B., et al., *SYNTHESIS OF SOME C-11-LABELED ALKALOIDS.* Chemica Scripta, 1982. **20**(1-2): p. 46-48.

70.   Langstrom, B., et al., *KINETIC ASPECTS OF THE SYNTHESES USING SHORT-LIVED RADIONUCLIDES.* Journal of Radioanalytical Chemistry, 1981. **64**(1-2): p. 273-280.

71.   Gray, B., *"Microfluidic poiseuille flow with applications to cell research platforms" Lecture notes.* 2008.

72.   COMSOLMultiphysics, *COMSOL Multiphysics MEMS Module user's guide.* p. p. 311 - 312, 315, 319, 321, 367 - 369.

73.   Dertinger, S.K.W., et al., *Generation of gradients having complex shapes using microfluidic networks.* Analytical Chemistry, 2001. **73**(6): p. 1240-1246.

74.   Langstrom, B. and G. Bergson, *THE DETERMINATION OF OPTIMAL YIELDS AND REACTION-TIMES IN SYNTHESES WITH SHORT-LIVED*

RADIONUCLIDES OF HIGH SPECIFIC ACTIVITY. Radiochemical and Radioanalytical Letters, 1980. **43**(1): p. 47-54.

75. COMSOLMultiphysics, *COMSOL Multiphysics Chemical Engineering Module user's guide.* p. p. 239 -240.

76. Chemical Rubber Company., *Handbook of chemistry and physics : a ready-reference book of chemical and physical data*, Chemical Rubber Pub. Co. [etc.]: Taylor and Francis Group. Cleveland, Ohio. p. p. 6-216 - 6-217.

77. Mark, J.E. and MyiLibrary., *Physical properties of polymer handbook.* 2007, Springer: New York ; [London]. p. xix, 1076 p. 29 - 30, 227 - 228.

78. Colosseum 15, P.E., The Netherlands. *Micronit Microfluidics BV*. Micronit Microfluidics BV.

79. Pascali, G., et al., *Microfluidic approach for fast labeling optimization and dose-on-demand implementation.* Nucl Med Biol, 2010. **37**(5): p. 547-55.

80. Ishiwata, K., S. Ishii, and M. Senda, *An alternative synthesis of [11C]raclopride for routine use.* Ann Nucl Med, 1999. **13**(3): p. 195-7.

81. Toepke, M.W. and D.J. Beebe, *PDMS absorption of small molecules and consequences in microfluidic applications.* Lab Chip, 2006. **6**(12): p. 1484-6.

82. Seong, G.H. and R.M. Crooks, *Efficient mixing and reactions within microfluidic channels using microbead-supported catalysts.* Journal of the American Chemical Society, 2002. **124**(45): p. 13360-13361.

83. Fukumura, T., et al., *Stability of 11C-labeled PET radiopharmaceuticals.* Appl Radiat Isot, 2004. **61**(6): p. 1279-87.

84. Bogni, A., et al., *Stability of L- S-methyl-C-11 methionine solutions.* Journal of Radioanalytical and Nuclear Chemistry, 2003. **256**(2): p. 199-203.